Fundamental Study of Flotation Behaviors and Oxidation Mechanisms of Polymorphic Pyrrhotite and Pentlandite

by

Chao Qi

A thesis submitted in partial fulfillment of the requirements for the degree of

Doctor of Philosophy

in

Chemical Engineering

Department of Chemical and Materials Engineering

University of Alberta

Abstract

This thesis is mainly concerned with understanding the flotation behaviors of the polymorphic pyrrhotite ($Fe_{1-x}S$, $0 < x \leq 0.125$) and pentlandite ($(Ni,Fe)_9S_8$) to find better measures for their flotation separation. The flotation separation of pentlandite from pyrrhotite is a complicated issue due to the complex chemical environment of the real flotation system. To learn more about the complex chemical environment, we conducted two plant surveys in the Strathcona Mill to learn about the flotation performance of polymorphic pyrrhotite and pentlandite and to find factors that impacted their flotation performance (Chapter 3). Two important phenomena were noticed: 1. the hexagonal pyrrhotite showed higher floatability than the monoclinic pyrrhotite in the Strathcona Mill; 2. the copper adsorption enhanced the flotation recovery of pyrrhotite. For further understanding these phenomena, pyrrhotite oxidation and copper activation were studied in Chapter 4 and Chapter 6, respectively. Importantly, the flotation separation of pentlandite from pyrrhotite was achieved with selective oxidation using hydrogen peroxide, which is shown in Chapter 5.

Pyrrhotite floatability is mainly related to its oxidation level. The oxidation rate of both pyrrhotites was investigated by cyclic voltammetry (CV) test, and oxidation level difference was evaluated with X-ray photoelectron spectroscopy (XPS) and Time-of-Flight secondary ion mass spectroscopy (ToF-SIMS). The CV tests demonstrated a higher

oxidation rate of the monoclinic pyrrhotite than the hexagonal pyrrhotite, further explained by the different variations of the Fe-S bond strength. Investigations of the oxidized polymorphic pyrrhotite surfaces with ToF-SIMS showed that the Fe-S bond strength decreased gradually over a 'defective layer' under the surface. Over this 'defective layer,' the Fe-S bond strength of the monoclinic pyrrhotite declined more steeply than that of the hexagonal pyrrhotite, which is mainly due to the faster incorporation of the oxygen atoms into the monoclinic pyrrhotite than into the hexagonal pyrrhotite.

For the flotation separation of the hexagonal pyrrhotite and pentlandite, hydrogen peroxide was employed to enlarge the oxidation difference between hexagonal pyrrhotite and pentlandite. The surface reactions of the hexagonal pyrrhotite and pentlandite towards the hydrogen peroxide conditioning were examined with electrochemical tests, XPS, ToF-SIMS, and dissolved oxygen (DO) studies. It was found that they responded differently towards the reduction reaction of hydrogen peroxide. On the hexagonal pyrrhotite, the reduction of the hydrogen peroxide was mainly balanced by the surface oxidation of the hexagonal pyrrhotite. While, on the pentlandite, the reduction of the hydrogen peroxide was balanced primarily by the oxidation of hydrogen peroxide. The more severe surface oxidation of the hexagonal pyrrhotite than the pentlandite rendered the hexagonal pyrrhotite lower floatability than the pentlandite.

As a critical factor in the surrounding chemical environment, copper activation effects were firstly confirmed with micro-flotation studies. To fully understand copper activation effects on pyrrhotite flotation, copper's effects on protecting pyrrhotite oxidation were investigated via the CV and XPS depth profile. It was found that copper protected pyrrhotite from severe oxidation by hindering the dissolution of sulfur. Meanwhile, the XPS depth profiles of the pyrrhotite showed that the Cu(I)S is the first and foremost copper activation species formed on pyrrhotite surfaces, which gradually oxidized to Cu(II)S and CuO as oxidation progresses. Cu(I)S is formed through the interaction between Cu^{2+} and surface reactive sulfur anions, which suggested that the copper adsorption can partially occupy the available sulfur anions to reduce the sulfur dissolution rate.

In summary, this study explained the flotation performance of polymorphic pyrrhotite and pentlandite with their different oxidation behaviors under specific chemical environments. Such fundamental understandings revealed the challenges in the floatation separation of pentlandite from hexagonal pyrrhotite and are valuable for exploring for more effective measures.

Preface

This thesis comprises several papers that have been either published, submitted, or ready for submission. Below is the statement of contributions of co-authors to papers presented in Chapters 3, 4, 5, and 6.

1. Chao Qi, Jing Liu, Jonathan Malainey, Lori J. Kormos, Julie Coffin, Curtis Deredin, Qingxia Liu, and Dominic Fragomeni. "The role of Cu ion activation and surface oxidation for polymorphic pyrrhotite flotation performance in Strathcona Mill." *Minerals Engineering* 134 (2019): 87-96. Chao Qi performed the data analysis, CV experiments, XPS studies, and ToF-SIMS tests and wrote the entire paper. Lori J. Kormos performed the QEMSCAN and XRD analysis. Julie Coffin, Curtis Deredin, and Dominic Fragomeni arranged and performed the plant surveys and the ICP analysis. Qingxia Liu supervised the work. All the authors contributed to the discussion and commented on the manuscript.

2. Chao Qi, Mohammad Khalkhali, James S. Grundy, Jing Liu, Jonathan Malainey, and Qingxia Liu. "Unraveling Polymorphic Pyrrhotite Electrochemical Oxidation by Underlying Electronic Structures." *The Journal of Physical Chemistry C* 123, no. 43 (2019): 26442-26449. Chao Qi performed all the experiments, data analysis and wrote the entire paper. Mohammad Khalkhali performed the density functional theory (DFT) modeling. Qingxia Liu supervised the work. All the authors contributed to the discussion and commented on the manuscript.

3. Chao Qi, Mohammad Khalkhali, James S. Grundy, Bo Liu, Aijing Wang, and Qingxia Liu. "Unraveling H_2O_2-stimulated Surface Oxidation of Hexagonal Pyrrhotite and Pentlandite by Underlying Electronic Structures." Accepted by *Minerals Engineering*. Chao Qi performed all the experiments, data analysis and wrote the entire paper.

Mohammad Khalkhali performed the DFT simulation. Qingxia Liu supervised the work. All the authors contributed to the discussion and commented on the manuscript.

4. Chao Qi and Qingxia Liu. “A Fundamental Study of the Cu Activation Effects on the Hexagonal Pyrrhotite. “Manuscript prepared for submission. Chao Qi performed all the experiments and data analysis and wrote the entire paper. Qingxia Liu supervised the work.

Acknowledgments

First of all, I want to express my sincere gratitude to my supervisor, Professor Qingxia Liu, for his continuous support, guidance, and encouragement throughout the whole period of my graduate study.

I want to thank members in Strathcona Mill for the assistance in conducting the two plant surveys and members in Expert Process Solutions (XPS) for helping me conduct sample analysis with QEMSCAN and XRD.

I would like to thank all my defense committee members (Dr. Qi Liu, Dr. Erin Bobicki, Dr. Kristian Edmund Waters, Dr. Douglas G Ivey, Dr. Jing Liu, and Dr. Qingxia Liu) for their time and efforts on reviewing my thesis and attending my defense.

I would like to thank Professor Zhenghe Xu, Professor Jingli Luo, Professor Qi Liu, and Professor Rajender Gupta for allowing me to use their instruments.

I want to thank Dr. Manqiu Xu and Dr. Zongfu Dai in Vale for providing the nickel concentrate samples.

I would like to express my gratitude to Dr. Mohammad Khalkhali for his help in performing the density functional theory (DFT) simulations. I also benefited a lot from the discussion with him about the modeling work.

I would like to express my gratitude to Dr. Jing Liu and Dr. James S. Grundy for their help in editing and reviewing my papers. I am also grateful for their patience, guidance, and encouragement.

I would like to thank Mr. Mingbo Zhang, Ms. Ni Yang, Mr. Mark Labbe, Dr. Mingli Cao, Dr. Shihong Xu, Dr. Anqiang He, Dr. Nancy Zhang, Mr. Darrin Molinaro, Mr. Yushi Wei, and Dr. Deepak Pudasainee for their training and assistances during my graduate study.

I acknowledge the administrative and technical assistance from Mr. Carl Corbett, Ms. Laurie Kachmryk, Mr. James Skawrok, Ms. Patricia Siferd, and Ms. Jie Ru.

I am grateful for all the helpful discussions from nickel research group members, including Mr. Jonathan Malainey, Ms. Caroline da Costa, Ms. Jing Han, Mr. Han Wang, Ms. Hua Run Zhao, and Dr. Jing Liu.

I want to thank my friend Dr. Kaiyang Li, Dr. Bo Liu, Mr. Cody Tischler, Dr. Mingxia Liu, Ms. Mantian Du, and Dr. Bailin Xiang for all the kindness received from them. The life of my graduate study would be different without their accompany.

I also want to acknowledge the Natural Sciences and Engineering Research Council of Canada (NSERC) and Glencore for all the funding, which supported a few other graduate students and me to get their degrees.

I would like to thank my colleagues and group member for all their help and collaborations during my graduate study.

I want to extend my deepest gratitude to my parents and my two sisters for all the support and love.

Table of contents

List of Tables

List of Figures

List of Abbreviations

AES	Auger electron spectroscopy
ARXPS	Angle-resolved X-ray photoelectron spectroscopy
BSE	Backscattered electron imaging
CEMS	Conversion electron Mössbauer spectroscopy
CV	Cyclic voltammetry
CP	Chronopotentiometry
CPs	Chronopotentiograms
DO	Dissolved oxygen
DFT	Density functional theory
EDX	Energy dispersive X-ray spectrometer
ICP	Inductively coupled plasma
ICP-OES	Inductively coupled plasma optical emission spectroscopy
ICP-MS	Inductively coupled plasma mass spectroscopy
JCPDS	Joint committee on powder diffraction standards
LPR	Linear polarization resistance
LSV	Linear sweep voltammetry
PAW	Projector augmented wave
PDF	Powder diffraction file
Po	Pyrrhotite
Pn	Pentlandite
QEMSCAN	Quantitative evaluation of materials by scanning electron microscopy
SEM	Scanning electron microscope
SLS	Sequential layer sputtering model
ToF-SIMS	Time-of-Flight secondary ion mass spectrometry
UV-vis	Ultraviolet-visible

VASP	Vienna Ab initio simulation package
XRF	X-ray fluorescence
XPS	X-ray photoelectron spectroscopy
XRD	X-ray diffraction

Chapter 1. Introduction

1.1. Introduction

Nickel is an important metal needed in many industries, including batteries, electronic devices, coins, alloys, etc. One important nickel sulfide mineral that is of economic interest is pentlandite, which is usually accompanied by a great abundance of pyrrhotite and chalcopyrite. For example, the main nickel source mineral in the nickel deposit of the Sudbury area is pentlandite, which is accompanied by abundant pyrrhotite and chalcopyrite. The pyrrhotite is usually taken as an undesirable gangue mineral since it wastes energy and emits sulfur dioxides (SO_2) during nickel smelting. This issue raises the need to separate pyrrhotite from pentlandite.

Flotation is currently the most used technique for the separation between the sulfides mentioned above. The flotation separation process can be described as following: mineral particles ground into a specific size range (from slightly over ten micrometers to hundreds of micrometers) are introduced into flotation cells at the top and flow downward; at the same time, bubbles are generated at the bottom flow upward. When the dropping particles come into contact with floating bubbles, bubbles will catch the hydrophobic particles and finally collected them into the concentrate, leaving the hydrophilic particles falling downward and finally collected as the tailings.

1.2. Background and Scope of the Thesis

Rejection of pyrrhotite during the flotation of pentlandite has been an issue for decades in the mineral processing industry, which has been complicated by the polymorphic pyrrhotite structures and the complex chemical environments.

Pyrrhotite is commonly divided into monoclinic pyrrhotite and hexagonal pyrrhotite or non-magnetic pyrrhotite. Even though polymorphic pyrrhotite has a similar crystal

structure, their rejection requires different measures. Until now, pyrrhotite rejection was limited to several known techniques with limited effects on hexagonal pyrrhotite flotation. Recently, ores from the Sudbury basin contain large amounts of hexagonal pyrrhotite, calling for more effective strategies for pyrrhotite rejection. The development of more effective measures for their depression is limited by a lack of fundamental understandings of polymorphic pyrrhotite flotation mechanism in the flotation mill.

In addition to the complicated pyrrhotite structures, the complex chemical environment for the flotation of pyrrhotite and pentlandite had made this issue more complicated. Previous research showed that the flotation behaviors of pyrrhotite and pentlandite are affected by numerous factors, including pulp pH, pulp potentials, Ca^{2+}, Cu^{2+}, Ni^{2+}, SO_2, mineral particles, etc. What makes things worse is that the working mechanisms of several factors among them are still not clear, rendering the exploration of pyrrhotite rejection techniques great difficult.

The research objectives of this thesis are to study the influential factors for the flotation behaviors of pyrrhotite and pentlandite in the plant survey and then conduct fundamental studies to understand these factors, including electronic structures, activation effects of metal cations, depressing effects of the hydrogen peroxide (H_2O_2).

1.3. Structure of the Thesis

This thesis contains 7 Chapters; Chapters 3-6 are papers that have been either published or ready to submit. The main content in each chapter is described as follows:

Chapter 1 provides a brief introduction to this thesis's background, motivations, objectives, and structure.

Chapter 2 is a literature review of studies about the flotation and oxidation of polymorphic pyrrhotite and pentlandite.

Chapter 3 presents a study about two plant surveys of the Strathcona Mill. The flotation behaviors of polymorphic pyrrhotite and pentlandite were recorded and analyzed for learning the main challenges in the flotation separation of pentlandite and pyrrhotite. This chapter has been published:

Chao Qi, Jing Liu, Jonathan Malainey, Lori J. Kormos, Julie Coffin, Curtis Deredin, Qingxia Liu, and Dominic Fragomeni. "The role of Cu ion activation and surface oxidation for polymorphic pyrrhotite flotation performance in Strathcona Mill." *Minerals Engineering* 134 (2019): 87-96.

Chapter 4 presents a fundamental study about the different electrochemical oxidation behaviors of the polymorphic pyrrhotite. The oxidation of pyrrhotite depends on the Fe-S bond strength, which changed gradually over a 'defective layer' under pyrrhotite surfaces. Over this 'defective layer,' the Fe-S bond strength in the monoclinic pyrrhotite drops more severely than those in the hexagonal pyrrhotite, leading to a higher oxidation rate of monoclinic pyrrhotite than hexagonal pyrrhotite. This chapter has been published:

Chao Qi, Mohammad Khalkhali, James S. Grundy, Jing Liu, Jonathan Malainey, and Qingxia Liu. "Unraveling Polymorphic Pyrrhotite Electrochemical Oxidation by Underlying Electronic Structures." *The Journal of Physical Chemistry C.* 123, no. 43 (2019): 26442-26449.

Chapter 5 illustrates the different oxidation behaviors of hexagonal pyrrhotite and pentlandite during hydrogen peroxide conditioning. This chapter has been submitted and accepted:

Chao Qi, Mohammad Khalkhali, James S. Grundy, Bo Liu, Aijing Wang, and Qingxia Liu. "Unraveling H_2O_2-stimulated Surface Oxidation of Hexagonal Pyrrhotite and Pentlandite by Underlying Electronic Structures." Accepted by the *Minerals Engineering*.

Chapter 6 explains the copper activation effects on the hexagonal pyrrhotite. This study has prepared for submission:

Chao Qi and Qingxia Liu. "A Fundamental Study of the Cu Activation Effects on the Hexagonal Pyrrhotite. "Prepared to submit.

Chapter 7 contains the conclusions of this research and future possible work based on this research.

The appendix includes the supporting information for chapters 4 and chapters 5.

Chapter 2. Literature Review

2.1. Introduction

The flotation separation of pyrrhotite from pentlandite is a long-standing issue in the mineral processing industry. It has become increasingly important with the increasingly complex ore conditions and increasingly stringent environmental requirements. So, it is important to know the challenging part of this long-standing issue. The flotation of pyrrhotite and pentlandite depends on numerous factors, including copper activation, mineral crystal structures, mineral zeta potentials, electrochemical oxidation reactivity, galvanic interactions, collector adsorptions, and so on. Here, the oxidation mechanisms of pyrrhotite and pentlandite are significant factors affecting their oxidation and flotation, discussed in the following sections.

2.2. Pyrrhotite

2.2.1. Polymorphic Pyrrhotite Structure

Pyrrhotite is non-stoichiometric (chemical formula $Fe_{1-x}S$, $0< x \leq 0.125$) and commonly found as monoclinic and hexagonal or orthorhombic crystal symmetries [1, 2]. Naturally occurring pyrrhotite is classified as monoclinic pyrrhotite (4C-Fe_7S_8) and hexagonal pyrrhotite (5C-Fe_9S_{10}, 6C-$Fe_{11}S_{12}$, and 11C-$Fe_{10}S_{11}$) due to iron vacancies. Here, the number before C shows the amount of unit cell (similar to nickel arsenide unit cell, Figure 2-1) along C axis direction required for specifying a superlattice with iron vacancies [3-5]. Among all these different types of pyrrhotite, the 4C- and 5C-pyrrhotite are the most commonly existed forms. The distributions of vacancies in the 4C-pyrrhotite and 5C-pyrrhotite are usually shown as Figure 2-2 [6], in which the total site occupancy layers alternate with the vacancy containing layers. Due to vacancies, the iron speciation in the polymorphic pyrrhotite is composed of different ferrous iron and ferric iron percentages to maintain charge neutrality [7]. For example, the 4C-pyrrhotite is usually described as $Fe_2^{3+}Fe_5^{2+}S_8$, and 5C-pyrrhotite is generally described as $Fe_2^{3+}Fe_7^{2+}S_{10}$.

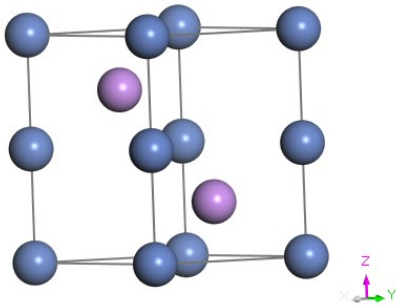

Figure 2-1. Nickel Arsenide (NiAs) unit cell [8].

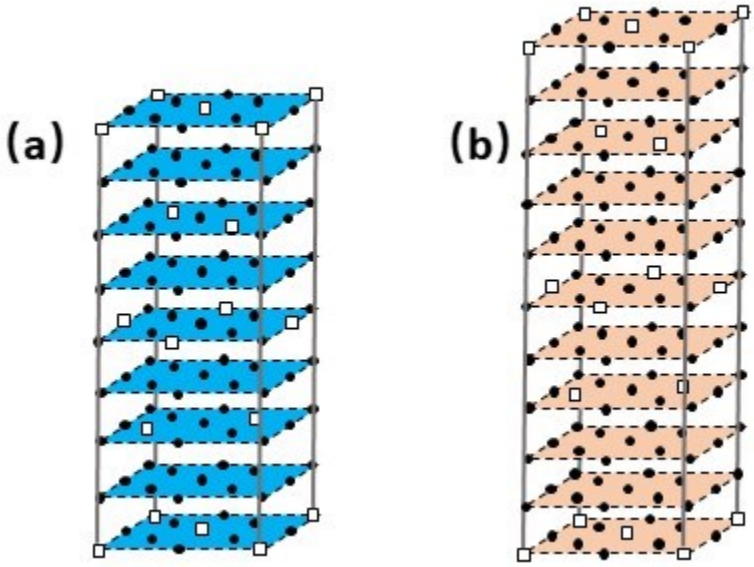

Figure 2-2. Distribution of the iron atoms and vacancies in the (a) 4C-pyrrhotite and (b) 5C-pyrrhotite (adapted from Multani and Waters (2018), with permission. John Wiley and Sons) [3]. The squares here represent iron vacancies, and sulfur atoms are omitted for clarity.

The hexagonal pyrrhotite is the common crystal form for the iron monosulfide because the pyrrhotite got the NiAs sub-cell, which has a hexagonal close-packed structure. The pyrrhotite can easily take the hexagonal form, but vacancies can lower the symmetry of the

crystal and 1/8 iron vacancies can lower the symmetry of pyrrhotite from hexagonal to monoclinic [9, 10].

Even though the hexagonal pyrrhotite ($a=b\neq c$, $\alpha=\beta=90°$, $\gamma=120°$, here, α is the angle between *b*-axis and *c*-axis, β is the angle between *a*-axis and *c*-axis, γ is the angle between *a*-axis and *b*-axis) and monoclinic pyrrhotite ($a\neq b\neq c$, $\alpha=\gamma=90°$, $\beta\neq 90°$) seems to be two totally different crystal structure, the monoclinic pyrrhotite structure here is just a slight distortion of the hexagonal pyrrhotite structure. The *ab*-plane of 4C-pyrrhotite (a=2A, $b=2\sqrt{3}$A) and 5C-pyrrhotite ($a=b$=2A) are shown in Figure 2-3 [4]. Here, 'A' and 'C' refers to the NiAs unit cell dimension along the *a*-axis and *c*-axis, respectively. Even though they got different shape on the *ab*-plane, the *ab*-plane of both pyrrhotites is composed of parts from the NiAs subcell. The main difference between the unit cell of these two pyrrhotites is the different value of β (the angle between the *a*-axis and *c*-axis). The β of 5C-pyrrhotite equals to 90 degree (and $\alpha=90°$), which means the *c*-axis is perpendicular to the *ab*-plane, and the β of 5C-pyrrhotite does not equals to 90 degree (while $\alpha=90°$), which means the *c*-axis of the 4C-pyrhotite tilts with respect to *ab*-plane [11]. Therefore, the monoclinic pyrrhotite could be taken as that the abundant iron vacancies in the 4C pyrrhotite tilted the unit cells of the crystal structure and made it monoclinic.

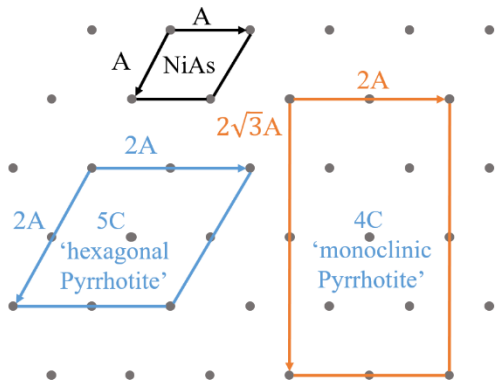

Figure 2-3. Unit cells of 4C-pyrrhotite, 5C-pyrrhotite, and NiAs projected on the ab-plane (001) (adapted from Multani and Waters (2018), with permission. John Wiley and Sons) [3].

One important thing needs to point out here is that the pyrrhotite crystal structure is not only a result of the number of vacancies but also a result of cooling rate [5]. At high temperature (above 300 °C), the vacancies distribution is random and the unit cell of pyrrhotite is NiAs subcell, the 1C structure, which is hexagonal [5]. As the temperature decreases, the vacancies start to order and the superstructures of NiAs subcell start to form [12]. Until below 300 °C, vacancies cannot move freely anymore, which may have the high-temperature structures locked in metastable status [5, 13-16]. That is why the quenching technique would only produce hexagonal pyrrhotite even thought the bulk composition is Fe_7S_8 [17]. For producing the monoclinic pyrrhotite, a prolonged annealing (slow cooling rate process) at around 250 °C is required to convert the hexagonal pyrrhotite to the monoclinic pyrrhotite [17].

The magnetic field of pyrrhotite contains alternating layers (*ab*-plane) of ferro-magnetically oriented magnetic moments and layers (*ab*-plane) of the anti-ferromagnetically coupled moments (Figure 2-4). Since layers of full iron sites and layers

with iron vacancies alternate with each other in the 4C-pyrrhotite (FAFBFCFD… as shown in Figure 2-2), the moment in vacancy layers orientate in the same direction and the moment in vacancy-free layers orientate in the same direction but anti-parallel to the direction of moments in vacancy layers. In pyrrhotite, iron is the carrier of spin moment and, therefore, the layer with cation vacancies got weaker magnetism than layers without vacancy. For 4C-pyrrhotite, the strong magnetism of the vacancy-free layers can not be counterbalanced by the weak magnetism of vacancy layers, making the monoclinic 4C-pyrrhotite ferrimagnetic. For other pyrrhotites, the magnetic moment orientations of vacancy layers and vacancy-free layers are complicated due to the relative position for the vacancy layer and vacancy free layer (like for 5C pyrrhotite, the relative position of vacancy layers and vacancy-free layers could be described as AFBFFCFDFF…, Figure 2-2). Therefore, the moment of the vacancy layers and the moment of vacancy free layers can orientate either direction (up or down as in Figure 2-4), which means the magnetic moment from different layers got the possibility of being counterbalanced. For example, the 5C-pyrrhotie (Fe_9S_{10}) is anti-ferrimagnetic because of the counterbalanced magnetic moments [5].

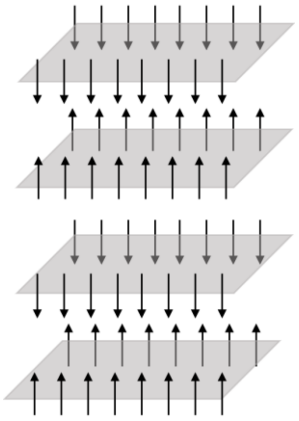

Figure 2-4. Magnetic moments configuration in pyrrhotite (adapted from Wang and Salveson (2005), with permission. Taylor and Francis) [5]

Except for their differences in magnetic property, hexagonal and monoclinic pyrrhotite minerals also demonstrate differences in other characteristics, particularly in their floatation behavior. As investigated in former research and numerous plant practices [18-20], hexagonal pyrrhotite got better floatability than monoclinic pyrrhotite, which has been attributed to the relatively low oxidation rate of the hexagonal pyrrhotite. The higher oxidation rate of the monoclinic pyrrhotite than hexagonal pyrrhotite was attributed to the more abundant Fe^{3+} and iron deficiencies in monoclinic pyrrhotite [21, 22]. Note that the Fe^{3+} work as internal oxidant and iron deficiencies may facilitate electron transfer.

2.2.2. Eh-pH Diagram

Pourbaix diagram (or Eh-pH diagram) is usually employed to understand the mineral's aqueous stability in solution under a specific Eh and pH condition. Figure 2-5 [23] shows that pyrrhotite is expected to be stable in potential ranges from -600 to -400 mV and pH from 7 to 9. Deviation from this area would generally result in pyrrhotite oxidation, either promoting iron dissolution or the formation of $Fe(OH)_3$. It is worth mentioning that the pyrrhotite stable area on the Eh-pH diagram may different in references due to different Gibbs Free Energy of pyrrhotite taken for calculation [24, 25].

When the Pourbaix diagram is used, extreme caution needs to be taken since the Poubaix diagram is usually calculated with thermodynamic data of stable chemical species, which means that metastable species are commonly not shown. Therefore, metastable kinetic species formed are typically considered and carefully analyzed by surface analysis tools. During consideration of metastable kinetic species, it was found that a slightly higher potential would be required for kinetic species formation than the potential calculated. It can be well shown in the Eh-pH diagram of S-H_2O system and pyrrhotite floatable potential in the presence of Na_2S. As shown in Figure 2-8, there are disagreements for the floatable

potential range at pH 8 and the potential range for elemental sulfur formation, which could be attributed to the overpotential required to form metastable species - sulfur [26]. Pourbaix diagram reflected the possible products of the thoroughly oxidized or reduced minerals, which is not likely to happen in real conditions. Understanding the surface properties of the pyrrhotite necessitates the characterization of the surface products formed under specific surrounding chemical environments (particularly the oxidizing environment) with surface analysis techniques.

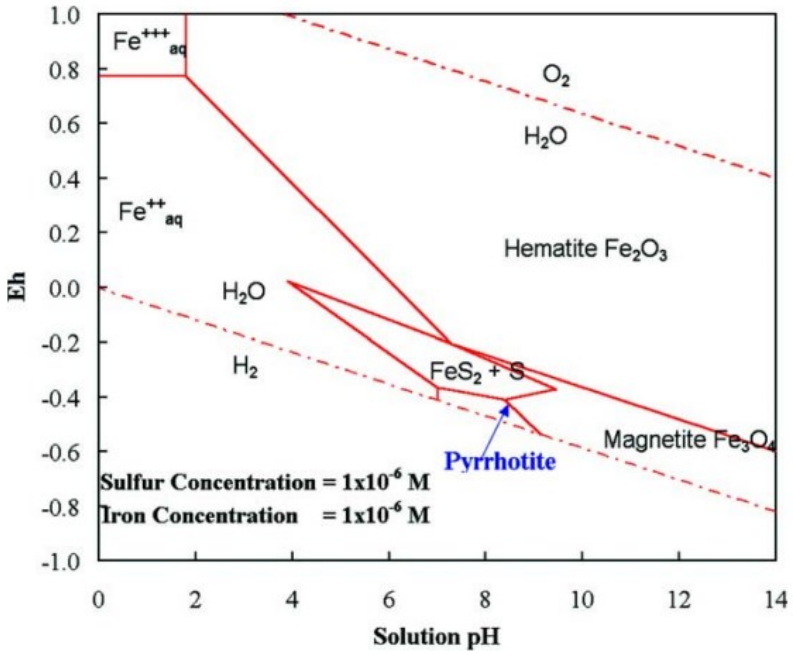

Figure 2-5. Stability regions of iron oxides and sulfides in water at 25 ℃, 1 atm. with Sum S = 1×10^{-6} mol/l and Sum Fe = 1×10^{-6} mol/l (adapted from Multani and Waters (2018), with permission. John Wiley and Sons) [3].

2.2.3. Oxidation Mechanisms of Pyrrhotite

The oxidation mechanism of the pyrrhotite has been widely studied with surface analysis techniques, including X-ray photoelectron spectroscopy (XPS), Auger electron spectroscopy (AES), Mössbauer spectroscopy as well as Time-of-Flight secondary ion

mass spectrometry (ToF-SIMS). The oxidation mechanism of pyrrhotite is a complicated topic and still could not be clearly defined, but numerous studies confirmed the gradual enrichment of sulfur in the pyrrhotite surface layers during pyrrhotite oxidation [27-30], particularly pyrrhotite oxidation in the air [31].

Steger studied the pyrrhotite oxidation by analyzing the water-soluble Fe(II), sulfate and thiosulfate with chemical extraction method [32]. By changing the temperature and relative humidity, Steger showed that pyrrhotite gradually oxidized to $FeSO_4$, $Fe(OH)(SO)_4 \bullet xH_2O$ and finally to Ferric oxide and elemental sulfur [32].

Using XPS, Buckley and Woods investigated the pyrrhotite oxidation in air and found that pyrrhotite oxidation occurs when exposed to the air for a few seconds. During this period, the iron diffused outwardly from the pyrrhotite surface layers and gradually changed to ferrous oxide and ferric hydroxy-oxide or hydrated oxide at the air/pyrrhotite interface [28]. The chemical formula for pyrrhotite oxidation in the air can be written as formula (2-1) [28]. According to the S *2p* spectrum changes, Buckley and Woods stated that the oxidation of the sulfur happens in the first few minutes and the total thickness of iron oxide and altered sulfide is less than 5 nm. When the pyrrhotite was exposed to the hydrogen peroxide solution, Buckley and Woods observed the formation of elemental sulfur and sulfate on pyrrhotite surfaces with XPS [33]. The elemental sulfur was further claimed as metal-deficient sulfides in a later study by Buckley et al. [27]. Using XPS and X-ray diffraction (XRD), Jones et al. observed that sulfate, iron-deficient sulfur-rich species, and ferric oxide/hydroxides formed on the pyrrhotite surfaces when oxidized in the air or water [30]. They also observed that the acid reaction restructured part of the surface to defective tetragonal Fe_2S_3 during the initial stage, further oxidized to the iron hydroxides as the oxidation progresses [30].

$$4Fe_{1-x}S + 3yO_2 + 2yH_2O = 2yFe_2O_3 \cdot H_2O(or 4yFeOOH) + 4Fe_{1-x-y}S \quad (2\text{-}1)$$

To refine the air oxidation mechanism of pyrrhotite, Pratt et al. [34] compared pyrrhotite fractured in a high vacuum chamber (10^{-7}) with pyrrhotite oxidized in the air by using a combination of XPS and AES. It is worth to note that they provided the first spectroscopic evidence for the existence of ferric iron in the pyrrhotite. After oxidizing the pyrrhotite in the air for 6.5 hours, the Fe(II)-S in the pyrrhotite decreased from 68% to 42%, while the Fe(III) increased from 32% to 58%, the majority of which iron changed from bonding with sulfur (Fe(III)-S) to bonding with oxygen atoms (Fe(III)-O). To describe the oxidation process, Pratt et al. [34] quantified the surface composition of the pyrrhotite oxidized for 6.5 hours and 50 hours in the air with AES and proposed the sequential layer sputtering model (SLS). The model described the oxidized pyrrhotite surface as the transition from the unaltered inner layers of pyrrhotite to the oxygen-rich sulfur-depleted top layers by going through the layer with a continuous and gradual decrease of S/Fe ratio. For example, the pyrrhotite oxidized for 50 hours in the air from the top surface to the deep inside consists of layers with $FeO_{1.5}$, FeS_2, Fe_2S_3, and Fe_7S_8. The chemical compositions of the oxidized pyrrhotite surfaces suggested that pyrrhotite oxidized through the combination of the outward diffusion of electrons and iron atoms, and the incorporation of oxygen atoms. The incorporation of oxygen atoms occurred through reducing the adsorbed oxygen molecules to O^{2-} by the electrons diffused from the pyrrhotite interior. They also stated that the rapid electron exchange between Fe(III) and Fe(II) is helpful for the outward diffusion of electrons and the vacancies are helpful for the outward diffusion of iron atoms. Further studies of pyrrhotite oxidation in pH 3.0 H_2SO_4 solutions for 8 hours showed that pyrrhotite oxidized through a similar process with a much higher average rate of the iron outward diffusion, forming a layer with a high S/Fe ratio [35]. Mycroft et al. [36] investigated the incipient oxidation of pyrrhotite with angle-resolved X-ray photoelectron spectroscopy (ARXPS) and concluded with a similar oxidation process. They stated that preferential

outward-diffusion of Fe over S results in a sulfur-rich zone, which includes both the disulfide species and marcasite (FeS_2) structure. The increase of disulfide in the oxidized pyrrhotite is also seen by Smart et al. [37] when pyrrhotite is investigated with ToF-SIMS.

During the investigation of pyrrhotite's flotation, dissolution, and depression, numerous research found that the polymorphic pyrrhotite exhibited different reactivity in the same chemical environment. Even though some disagreements exist as to which superstructure is more susceptible to oxidation, most references showed that the 4C-pyrrhotite got oxidized more easily than the 5C-pyrrhotite [18, 21, 38-40]. As shown in the pyrrhotite oxidation products, the vacancies and Fe^{3+} were believed to be helpful for pyrrhotite oxidation since vacancies can facilitate the outward diffusion of iron cations and the Fe^{3+} is more acceptable to the oxygen atoms. Therefore, the easier oxidation of 4C-pyrrhotite than 5C-pyrrhotite was usually attributed to the more abundant vacancies and Fe^{3+}.

Besides vacancies and Fe^{3+}, Janzen proposed that the substitution of iron by nickel and cobalt cations in the pyrrhotite structure can hinder the pyrrhotite oxidation since the positive charge near nickel and cobalt can limit the movement of electrons in pyrrhotite structures [21]. Kwong suggested a similar conclusion during the study of monoclinic pyrrhotite, in which the monoclinic pyrrhotite with high trace metal content (nickel and cobalt) got a relatively low oxidation rate [41].

During the evaluation of the different reactivity of polymorphic pyrrhotite, it is also essential to consider the galvanic interaction between pyrrhotite and the surrounding environment, including the grinding media and the naturally accompanied minerals [42-47]. Becker et al. [48] once proposed that the higher reactivity of 4C-pyrrhotite than the 5C-pyrrhotite is also possibly because 4C-pyrrhotite is more commonly found with pyrite.

2.2.4. Collectorless Flotation

Pyrrhotite has been reported to exhibit natural floatability under mild oxidizing environments [26]. The formed hydrophobic species have mainly been attributed to sulfur species, such as elemental sulfur, metal-deficient polysulfides, etc. [26, 49-51]. A surface sulfur complex $Fe(OH)(S_2)$ is believed to be a possible intermediate oxidant product, as formed by formula (2-2) [3].

$$FeS_{1.13} + H_2O = Fe(OH)S_2 + S_2^{2-} + H^+ + e^- \quad (2\text{-}2)$$

The pulp potential range for self-induced floatability of pyrrhotite as a function of pH is shown in Figure 2-6 [26]. The upper limit potential E_mU and the lower limit potential E_mL of pyrrhotite collectorless flotation decrease with pH. When the pH increased from pH 2 to pH 12, E_mU declined from 750 to 300 mV vs. SHE, and E_mL decreased from 450 to 50 mV vs. SHE. As the OH^- concentration increased in the solution, the equilibrium potential calculated in formula (2-3) will drop.

$$E_h = E_h^0 - 0.0591 \times \log [OH^-] \quad (2\text{-}3)$$

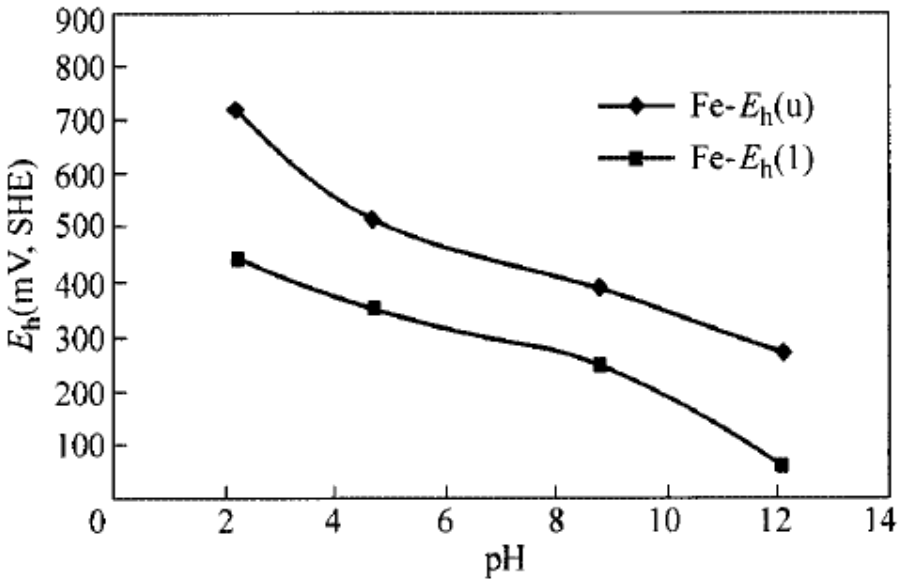

Figure 2-6. Collectorless flotation recovery of pyrrhotite as a function of Na_2S concentration at different pH condition (adapted from Hu et al. (2009), with permission. Springer) [26].

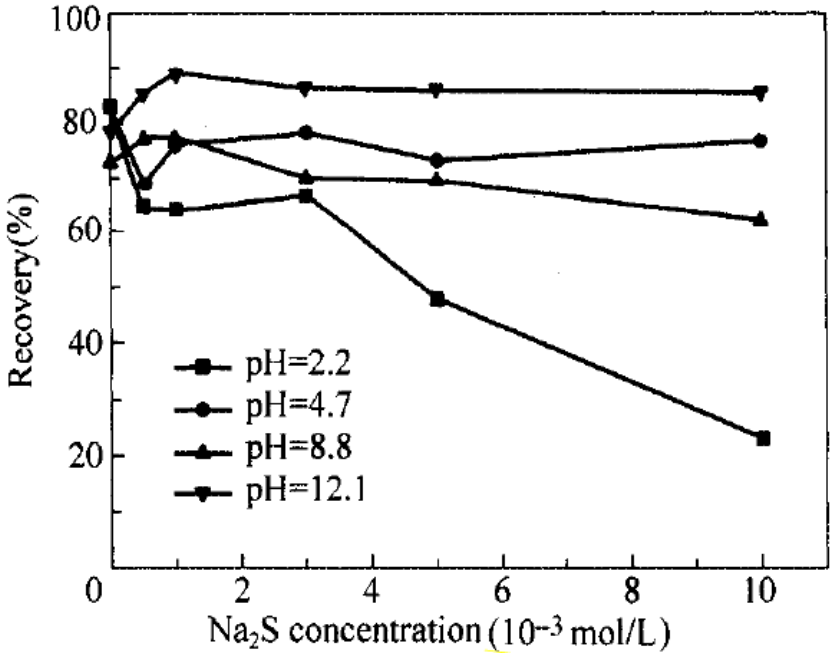

Figure 2-7. Collectorless flotation recovery of pyrrhotite as a function of Na_2S concentration at different pH conditions (adapted from Hu et al. (2009), with permission. Springer) [26].

For sulfide minerals, collectorless floatability can be divided into self-induced floatability (without any sodium sulfide) and sulfur-induced floatability (with the presence of sodium sulfide). Some iron sulfide minerals (such as pyrite, arsenopyrite) demonstrate low self-induced floatability but strong sulfur-induced floatability. As for pyrrhotite, Hu et al. demonstrated that the effect of sodium sulfide on the pyrrhotite collectorless floatability depends on the solution pH [26]. Figure 2-7 shows that as the pH increases from 2.2 to 12.1, sodium sulfide showed increasingly positive effects onto pyrrhotite flotation, with slight depression effects at pH 2.2 and activation effects at pH 12.1. It has been proposed that elemental sulfur is the hydrophobic entity for pyrrhotite sulfur-induced floatability (Figure 2-8). The improved sulfur-induced collectorless floatability of pyrrhotite at high pH is probably related to the increased difference between the open circuit potential of pyrrhotite and the potential for sulfur formation (Figure 2-8 and Figure 2-9). That is to say, the difference between the open circuit potential of pyrrhotite and the potential required for sulfur formation at pH 12 was much larger than that at pH 2. Hayes et al. also demonstrated that sulfide minerals with higher open circuit potential got higher sulfur-induced floatability [52]. One possible explanation is that the high rest potential could promote the oxidation of sodium sulfide to hydrophobic sulfur.

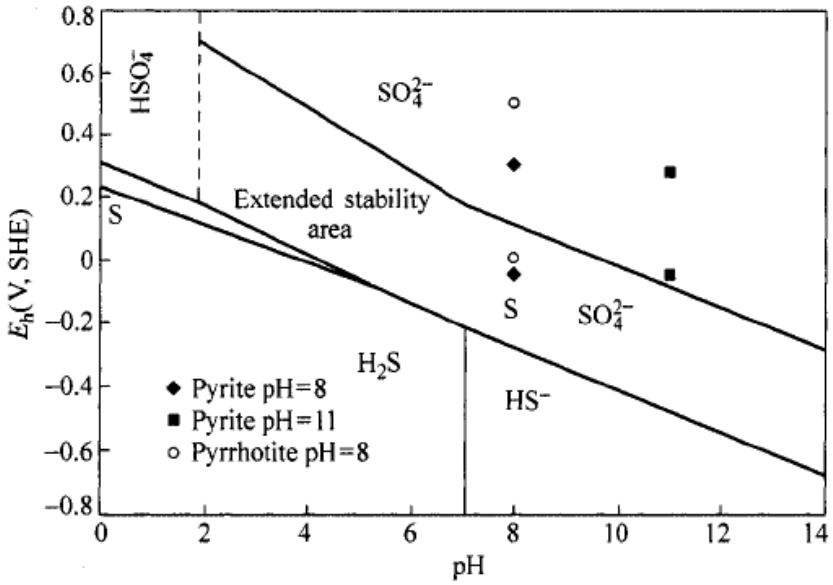

Figure 2-8. Eh-pH diagram of sodium sulfide (elemental sulfur as metastable phase) (adapted from Hu et al. (2009), with permission. Springer) [26].[1]

[1] Equilibrium lines drawn based on 10^{-3} mol/L dissolved species, plotted points show potential range of sulfur-induced flotation of pyrrhotite from literature.

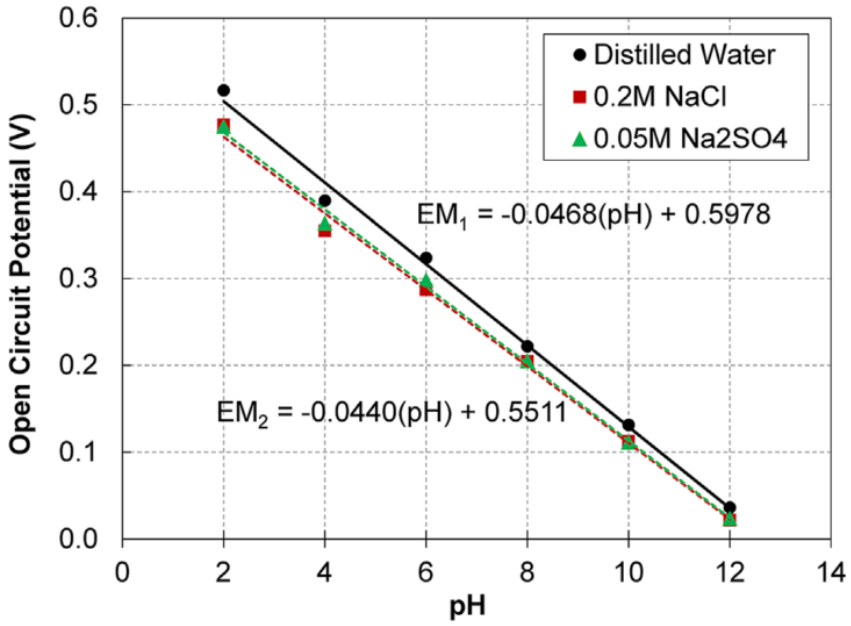

Figure 2-9. Open circuit potential of pyrrhotite as a function of pH in several electrolyte solutions (adapted from Multani and Waters (2018), with permission. John Wiley and Sons) [3].

Interestingly, the ore locality has shown an impact on the collectorless floatability of pyrrhotite. Among those five pyrrhotite ore deposits that Becker compared, non-magnetic pyrrhotite from Sudbury shows the highest collectorless floatability at pH 7 and 10 [18]. As discussed in detail by Multani and Waters's review, the high floatability of the non-magnetic pyrrhotite could be attributed to pyrrhotite type and lots of other factors, including crystallography, Fe^{3+} and Ni^{2+} content, and mineral associations [3].

2.2.5. Interactions with Xanthate

For the pyrrhotite and xanthate interaction, a two-step process consisted of the first physisorption and then oxidation was proposed [53]. Based on the phenomenon that anodic peaks on the cyclic voltammetry (CV) of pyrrhotite shifted to more anodic values when xanthate was added into the buffer solution (pH 9), Hodgson and Agar postulated that

xanthate is initially adsorbed onto pyrrhotite surface by forming $Fe(OH)_2X$ product via coulombic attraction (formula (2-4) & formula (2-5)). Physically adsorbed xanthate was then oxidized to dixanthogen by the reduction of oxygen (formula (2-8)). Since xanthate oxidation (formula (2-6)) is not pH-dependent, dixanthogen formation depends much more on the alkyl chain length of xanthate and its concentration, as can be seen from the dixanthogen formation potential shown as formula (2-7) (Nernst Equation).

$$FeS + 2H_2O = Fe(OH)[S]^+ + 2H^+ + 2e^- \quad (2\text{-}4)$$

$$Fe(OH)[S]^+ + X^- = Fe(OH)[S]X \quad (2\text{-}5)$$

$$2X^- = X_2 + 2e^- \quad (2\text{-}6)$$

$$E_h = E_h^0 + 0.0591 \times \log [X^-] \quad (2\text{-}7)$$

$$O_2 + 2H_2O + 4e^- = 4OH^- \quad (2\text{-}8)$$

For xanthate adsorption onto pyrrhotite, it was pointed out that pyrrhotite was required to be oxidized (formation of $Fe(OH)[S]^+$) to provide a suitable site for dixanthogen adsorption [53]. Even though mild oxidation is required for xanthate adsorption onto pyrrhotite, severe oxidation of pyrrhotite can decrease their hydrophobicity, so does the excessive cathodic polarization. Figure 2-10 demonstrated that both the lower and upper floatable potential of pyrrhotite in the presence of ethyl xanthate. Floatable potentials decrease with the increase of pH [26]. Even though Fornasiero et al. [54] showed that only dixanthogen is observed on pyrrhotite surface at pH 5.5, pH 7, and pH 9, the particularly low potential required for pyrrhotite flotation at pH 12 suggested that hydrophobic entity required for pyrrhotite flotation at pH 12 at the existence of xanthate could be metal xanthate. The potential required for the oxidation of ethyl xanthate to dixanthogen is 0.179V, and the lower floatable limit at pH 12 is around 0.05 V (Figure 2-10).

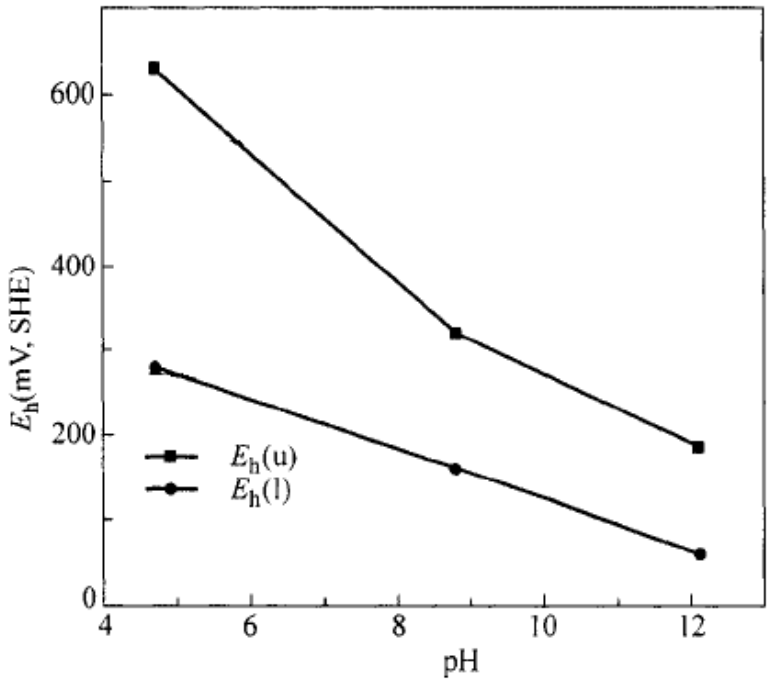

Figure 2-10. The Lower (E_hL) and upper (E_hU) limiting collector flotation potential of pyrrhotite at different pH (Ethyl Xanthate 10^{-4} M) (adapted from Hu et al. (2009), with permission. Springer) [26].

Other than E_h, pH and xanthate type also affect pyrrhotite xanthate interactions. According to Barsky relationship ($[X^-]/[OH^-]=K$) [55], xanthate and hydroxide ions are competing to adsorb onto the sulfide mineral surface. The Barsky relationship explained that the pyrrhotite floatability in the presence of xanthate is progressively inhibited by increased pH [56, 57]. Becker compared the influence of sodium isobutyl xanthate (SIBX) and sodium normal propyl xanthate (SNPX) on pyrrhotite from several different localities showed that SIBX is a stronger collector than SNPX for most of the pyrrhotite ores they studied [18], which is probably due to the longer chain length of SIBX.

2.2.6. Ions Effects

Interactions between pyrrhotite and xanthate are also affected by ions in process water. Even though some of the findings are not consistent, they agree that the Ca^{2+} will depress pyrrhotite flotation, but Cu^{2+} and Ni^{2+} can activate pyrrhotite flotation.

Hodgson and Agar showed that Ca^{2+} ions (350 ppm Ca, at pH 9.5) increased the xanthate dosage needed for pyrrhotite flotation due to possible competitive adsorption [53]. However, Rao and Finch showed that at one specific condition (pH 8.4, N_2, 300 ppm Ca^{2+}) Ca^{2+} ions were beneficial for pyrrhotite flotation in the presence of xanthate, which is probably due to the bridging effect of $Ca(OH)^+$ formed under this condition [56]. Different effects of Ca^{2+} on pyrrhotite flotation in these two references may relate to the relative amount of $Ca(OH)_2$ formed since 350 ppm at pH 9.5 would produce lots of $Ca(OH)_2$ precipitation than 300 ppm at pH 8.4. However, as to the critical Ca^{2+} concentration for pyrrhotite flotation, lower than which Ca^{2+} show activating effects and higher than which Ca^{2+} show depressing effects, it is still not clear.

Meanwhile, Hodgson and Agar also showed that the presence of $S_2O_3^{2-}$ can increase the xanthate dosage needed for achieving a required hydrophobicity for pyrrhotite (contact angle > 80° for a 5 µl bubble). Moreover, the combination of lime and thiosulphate can increase the required xanthate dosage significantly. The possible mechanism for the adsorption of $S_2O_3^{2-}$ ions onto the pyrrhotite surface was explained as Figure 2-11 [53].

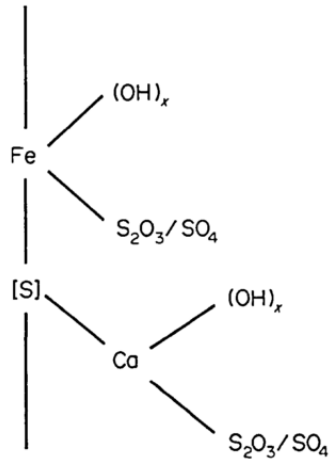

Figure 2-11. Possible adsorption mechanism of $S_2O_3^{2-}$ ions onto pyrrhotite surfaces (adapted from Hodgson and Agar (1989), with permission. Taylor and Francis) [53]. Note that [S] represents a polysulfide sulfur site.

Cu and Ni activation effects onto polymorphic pyrrhotite flotation have been identified and widely accepted. Becker's research on the polymorphic pyrrhotite demonstrated the activation effect of Cu^{2+} ions [18]. Similarly, in a plant practice study, it was observed that seasonal nickel content in the slurry has a close correlation with the Pn/Po (pentlandite/pyrrhotite) flotation selectivity, suggesting activating effects of Ni^{2+} on pyrrhotite flotation [58]. Yoon et al. showed that Cu, Ni, and Ag activation effects on pyrrhotite flotation in Clarabelle Mill via the metal ion concentration in the pulp and on mineral surfaces [59].

Even though both Cu and Ni have shown activation effects on polymorphic pyrrhotite flotation, studies about Cu activation effects are more abundant than Ni activation. For studies of Cu activation, they are summarized according to their adsorption mechanism, effects on pyrrhotite-xanthate interaction, and parameters that matter for Cu adsorption.

For copper adsorption onto pyrrhotite in alkaline conditions, there are two assumptions worth mentioning. One states that Cu is mainly adsorbed as $Cu(OH)_2$ [60]. Another is that

copper adsorbed onto pyrrhotite surface at pH 9 reduced to Cu(I), which is probably related to the oxidation of surrounding sulfur sites [61].

As to their effects on pyrrhotite-xanthate interaction, Cu^{2+} had been shown to change pyrrhotite zeta potential and oxidize xanthate to dixanthogen. Acar and Somasundaran [62] showed that 10^{-2} M $CuCl_2$ could reverse pyrrhotite potential from negative to positive even at pH 10. Multani et al. [63] showed that the zeta potential of both monoclinic and hexagonal pyrrhotite improved significantly with the addition of 10^{-4} M $CuSO_4$, suggesting a higher coulombic attraction force between pyrrhotite and xanthate. During xanthate interaction with Cu-activated pyrrhotite surfaces, CuX_2 was considered formed initially and then oxidized to X_2 via the reduction of cupric copper to Cu_2X_2 [60].

Several parameters that have been shown crucial for copper activation onto pyrrhotite are Cu^{2+} concentration, reagents adding orders, and pyrrhotite pre-oxidation. As stated earlier, part of the adsorbed copper formed the $Cu(OH)_2$ species, and too high $Cu(OH)_2$ would possibly result in pyrrhotite depression. As to the reagents adding order, Allison and O'Connor showed that copper's activation effects were passivated when added after xanthate because copper activating effects lie in aiding xanthate adsorption and oxidation [60]. Furthermore, Gerson claimed that copper activation is less effective on pre-oxidized pyrrhotite surfaces [61].

The higher Cu activating effects onto hexagonal pyrrhotite than monoclinic pyrrhotite have been demonstrated via micro-flotation by Becker, followed by further evidence in zeta potential [63] and Cu/Fe ratio [61]. As to the fundamental reason for differential Cu activation effects, Multani and Waters attributed it to the Fe^{2+}/Fe^{3+} ratio [3], and Gerson attributed it to the differential oxidation rate [61]. Gerson showed that the lower Cu/Fe ratio on oxidized monoclinic pyrrhotite surface than that of hexagonal pyrrhotite was well

related to the higher oxidation tendency of monoclinic pyrrhotite than hexagonal pyrrhotite [61].

As to the studies of Ni activating effects on polymorphic pyrrhotite, it is mainly shown in plant practices, and nickel's effects in slightly improving both types of pyrrhotite zeta potential in alkaline conditions (around pH 9) [63]. With limited studies in Ni activation on polymorphic pyrrhotite, studies relate to nickel activation would hike and possibly follow a similar manner to that of Cu activation studies. For further studies of Ni activation on polymorphic pyrrhotite, the differential oxidizing properties between Ni^{2+} and Cu^{2+} should be considered since Cu^{2+} oxidizing properties are claimed to be helpful for its adsorption and xanthate oxidation. To show Cu^{2+} and Ni^{2+} oxidizing property difference, on the one hand, Gerson demonstrated that Cu^{2+} could oxidize xanthate to dixanthogen in the N_2-purged solution even though no effects on promoting dixanthogen formation on pyrrhotite surface; on the other hand, Gerson showed that Ni^{2+} could not oxidize xanthate to dixanthogen in a similar oxygen-deficient environment [61].

2.3. Pentlandite

2.3.1. Pentlandite Structure

Pentlandite ($(Fe,Ni)_9S_8$) is the principal source sulfide mineral commonly found with pyrrhotite and pyrite [53, 64-68]. The pentlandite structure is a cubic cell with F*m3m* symmetry, and the chemical formula of pentlandite is M_9S_8 [69]. Here, M refers to the metal cations, most commonly found as Fe, Ni, and Co. There are 36 metal cations and 32 sulfur anions in the pentlandite cubic cell. Of the 36 metal cations, 32 are tetrahedrally coordinated, and 4 are octahedrally coordinated—every tetrahedrally-coordinated cation bond with four sulfur anions, and every octahedrally-coordinated cation bonds with six sulfur anions. Of the 32 sulfur anions, 24 are fivefold-coordinated (bonds with five metal cations), and 8 are fourfold-coordinated (bonds with four metal cations) [69]. The metal

cations in natural pentlandite samples are most commonly found as Fe and Ni with the Ni:Fe ratio of approximately 1:1, and sometimes it can be found as mono-metallic cobalt pentlandite (Co_9S_8) [70]. The Ni and Fe atoms were generally considered distributed randomly across all the tetrahedral and octahedral sites in the pentlandite [71, 72]. Still, some evidence suggested that iron atoms can preferentially occupy the octahedral sites [73].

2.3.2. Oxidation Mechanism of Pentlandite

In 1989, Richardson and Vaughan [66] studied the oxidation of the synthetic pentlandite with several surface spectroscopic techniques, including XPS, AES, and conversion electron Mössbauer spectroscopy (CEMS). The pentlandite oxidation was conducted in several different environments to exemplify pentlandite oxidation in natural environments and during extraction. The surface analysis results showed that pentlandite oxidation resulted in a nickel-rich sub-surface and an oxidized surface with numerous oxide species, including iron oxides, iron hydroxides, iron sulfates, and nickel oxides. Comparing the oxidized surfaces of pentlandite from different conditioning environments, they proposed the oxidation sequence of pentlandite. The initial oxidation of pentlandite formed the oxide layer with abundant iron oxides, keeping the pentlandite from fast oxidation. Further oxidation of pentlandite was realized in the preferential dissolution of iron, leaving an iron-deficient subsurface to transform to violarite.

In 1991, Buckley and Woods [64] studied the pentlandite oxidation in an aqueous solution using XPS and electrochemical techniques. They found that the initial pentlandite oxidation in the air formed a hydrated iron oxide overlayer and a metal-deficient sub-layer. In contrast, the further oxidation involved the outward diffusion of nickel to the oxide overlayer. They also observed that pentlandite oxidation in alkaline solution happened

similarly to its oxidation in the air but at a higher rate. Electrochemical studies of pentlandite oxidation suggested that preferential iron removal during anodic oxidation.

Legrand et al. [65, 74] studied the pentlandite oxidation in pH 9.3 aqueous solutions with XPS and AES. Surface analysis showed that one thin overlayer (several nanometers thick) formed on the pentlandite contains Fe(III) oxyhydroxide, Fe(III)-S, violarite ($FeNi_2S_4$), $NiSO_4$, $Ni(OH)_2$, and polysulfides.

Marape and Vermaak [67] investigated the effects of the composition of pentlandite on its electrochemical behaviors. They found the oxide film formed on the pentlandite decreased pentlandite's reactivity towards the oxygen reduction. The reduced reactivity was attributed to the oxidized film, which changed the oxygen reduction from the four-electron reaction to the two-electron reaction.

2.4. Flotation Separation of Pentlandite from Pyrrhotite

2.4.1. Galvanic Interaction between Pyrrhotite and Pentlandite

Due to the importance of the collector adsorption on the sulfide mineral flotation, the collector adsorption mechanisms and affecting parameters were widely studied. Investigations of the collector adsorption on sulfides in the single mineral system showed that the interaction between xanthate and sulfide surfaces was affected by a combination of several essential variables, including pulp potential, metal cations, pH, etc. However, understanding the collector adsorption on sulfides in the single mineral flotation system did not make sure their application in the paired mineral system since the galvanic interaction between different minerals also affected the collector adsorption [75-79].

Bozkurt et al. [75] studied the galvanic interaction between the pyrrhotite and pentlandite by comparing the xanthate adsorption on these two sulfides in the single mineral system and mixed mineral system. They tested the amount of xanthate adsorbed onto pyrrhotite and pentlandite under three conditions: a) single mineral system, b) mixed mineral system share the same solution but no direct contact, and c) the mixed mineral system share the same solution with direct contact. The FTIR-ATR spectra results showed that the amount of xanthate adsorbed on pentlandite was a) < b) < c), and that on pyrrhotite was c) < b) < a). They explained the different adsorption behaviors of xanthate in these three different systems with the mixed potential model. The mixed potential model described that when the pentlandite has physical contact with pyrrhotite, the anodic oxidation of xanthate to dixanthogen happened on the pentlandite and the cathodic reaction of oxygen to hydroxyl ions occurred on pyrrhotite.

As shown in the mixed potential model proposed by Bozkurt et al. [75], the galvanic interaction between pyrrhotite and pentlandite is beneficial for the flotation separation of pentlandite and pyrrhotite. Since the galvanic interaction between pyrrhotite and pentlandite depends on their rest potential, which is significantly affected by the system potential and dissolved oxygen (DO), Khan and Kelebek [80] achieved a better Pn/Po flotation selectivity by lowering the amount of dissolved oxygen and controlling a low pulp potential.

2.4.2. Pyrrhotite Depression with Amine Chelates

Yoon et al. [59] claim that diethylenetriamine (DETA) is an effective reagent in improving the flotation recovery of pentlandite and meanwhile keep the para-magnetic pyrrhotite depressed under oxidizing conditions. They attributed the depression effect of DETA to its effects on increasing the adsorption potential of xanthate on pyrrhotite and its effects on

decreasing the contact angle at the same adsorption amount of xanthate [59]. They also pointed out several other possible reasons: pyrrhotite can be activated by the Cu^{2+}, Ni^{2+} and Ag^{+} ions in processing water, and DETA is an effective chelator in removing these cations in the processing water [59]; the activation products formed on para-magnetic pyrrhotite surfaces are usually insoluble under reducing conditions but possibly soluble when they are converted to oxides in the presence of DETA.

In 1999, Kelebek and Tukel [81] separated pentlandite from hexagonal pyrrhotite effectively via the combination of sodium metabisulfite (SMBS) and triethylenetetramine (TETA). However, they did not explore the mechanism of this synergistic effect, only suggested that this could be similar to the synergistic effect of the Sulphur dioxide-DETA system, which is related to the potential control and chelation [81]. This phenomenon shows the high deficiencies in the fundamental understanding of the effect of the combination of these two reagents.

Manouchehri [82] used sulfite and DETA to separate pentlandite from pyrrhotite only get a good result when magnetic pyrrhotite is the dominant form of pyrrhotite.

Tukel and Kelebek [83] claim that one possible mechanism of SMBS in depressing pyrrhotite is its effect in decomposing xanthate to carbon disulfide and therefore decreasing the adsorption of xanthate onto pyrrhotite surfaces. TETA, on the other hand, serves as a reactive reagent in releasing surface species into the aqueous phase. Therefore, the effectiveness of the combination of SMBS and TETA in separating pentlandite from hexagonal pyrrhotite could be of a similar mechanism.

Bozkurt et al. [42] used the specific dixanthogen IR spectra peak height as an index for the amount of dixanthogen adsorbed on mineral (pentlandite and pyrrhotite) surfaces. They discovered that when pentlandite and pyrrhotite are mixed the adsorbed amount of dixanthogen on pentlandite increased and that on pyrrhotite decreased significantly [42]. More importantly, the combination of DETA and SMBS is most effective in increasing the ratio of dixanthogen adsorbed onto pentlandite surfaces to the amount of dixanthogen adsorbed onto pyrrhotite surfaces.

Kelebek et al. [84] find that both SO_2 and DETA can depress the flotation of both pentlandite and pyrrhotite at collectorless flotation conditions. The collectorless flotation of sulfides depends mainly on the oxidation level of sulfides, which can be significantly lowered by heavy metal cations, like Cu^{2+}, Ni^{2+} etc. Therefore, they attributed the depressing effects of DETA partially to DETA's deactivation effects [84]. Furthermore, they claim that a sufficient amount of SO_2 can produce more thiosulfate by further oxidizing the hydrophobic layer [84]. They also found that the depressing effects of DETA and SO_2 on pentlandite is reversible when a sufficient amount of xanthate added and pyrrhotite will keep being depressed even if enough xanthate added, which may result from the formation of complex $[Ni(DETA)_2]S_2O_6$ on sulfide mineral surfaces under collectorless flotation conditions. In this way, the flotation separation of pentlandite from pyrrhotite can be achieved in the presence of DETA, SO_2 and a sufficient amount of xanthate.

Recent work by Multani and Waters [85] compared the effects of DETA alone, DETA/SMBS, sulfuric acid/DETA/SMBS with aeration, sulfuric acid/DETA/SMBS without aeration, and DETA/SMBS with concentrate regrind on ores with high Po/Pn ratio (7.5). Of all the pyrrhotite contained in the ore, 42% is hexagonal pyrrhotite. The

comparison showed that the DETA/SMBS with concentrate regrind gives the best result, in which ~85% pentlandite recovery and ~11% pyrrhotite recovery were achieved.

2.4.3. Pyrrhotite Depression with Polymers

Due to environmental concerns, some polymeric reagents have also been tried as pyrrhotite depressants, like in South African plants [86]. They tried to use guar gum carboxymethylcellulose (CMC), most of which are effective and environmental-friendly. Some other organic-based reagents are also proved to be good pyrrhotite depressants, such as the 'SD' series, a mixture of lignosulfonates and starches [87].

2.4.4. Other Pyrrhotite Depression Strategies

(1) Pyrrhotite flotation depression with cyanide

Kalahdoozan showed in the lab-scale test work that cyanide can effectively depress pyrrhotite flotation at alkaline pH [57]. The exact depression mechanism is still not clear, but it was suggested that the depression effects of cyanide come from the formation of metal cyanide complexes and cyanide's ability in decomposing the adsorbed dixanthogen [88].

(2) Pyrrhotite rejection with magnetic separation

The magnetic separation was implemented quite early for pyrrhotite rejection since it can effectively separate the magnetic monoclinic pyrrhotite. In Clarabelle Mill (Sudbury, Canada), the magnetic separation was employed via the drum magnetic separator to separate the magnetic fraction (including the monoclinic pyrrhotite) from the bulk ore and processed separately. Such process separated the high sulfur tail (monoclinic pyrrhotite) from the low sulfur tail (silicate mineral), which is a great advantage for tail disposal [89].

(3) Collector starvation

It is expected that the xanthate would preferentially adsorb on copper sulfides and nickel sulfides than the pyrrhotite (iron sulfide), which means that keeping the xanthate concentration low would help improve the flotation selectivity of valuable minerals (nickel sulfides and copper sulfides) against pyrrhotite [3].

(4) High pH with sulfite

Hodgson and Agar showed that $S_2O_3^{2-}$ increased the xanthate dosage required for pyrrhotite flotation, and the combination of lime and thiosulphate can increase the necessary xanthate dosage particularly significant [53]. The addition of sulfite limited the formation of hydrophobic surface species on pyrrhotite by maintaining a low pulp potential [82].

2.4.5. Pyrrhotite Depression Practices in Mineral Processing Plant

For pyrrhotite rejection, it is important to know typical pyrrhotite rejection practice in mineral processing plant. In Canada, the Strathcona Mill and the Clarabelle Mill are two important milling plants aims to reject pyrrhotite to get a high-grade copper concentrate and a high-grade nickel concentrate. Here, only the Clarabelle mill was covered in the literature review since the flowsheet of the Strathcona Mill is covered in Section 3.2 Strathcona Mill Flowsheets.

(1) Vale – Clarabelle Mill [90]

In Clarabelle Mill, both the siliceous gangue and the nickeliferous pyrrhotite are intended to be rejected in the flotation process to reach the goal of a high-grade nickel concentrate (16% Cu+Ni) and a high-grade copper concentrate (31% Cu+Ni) [90].

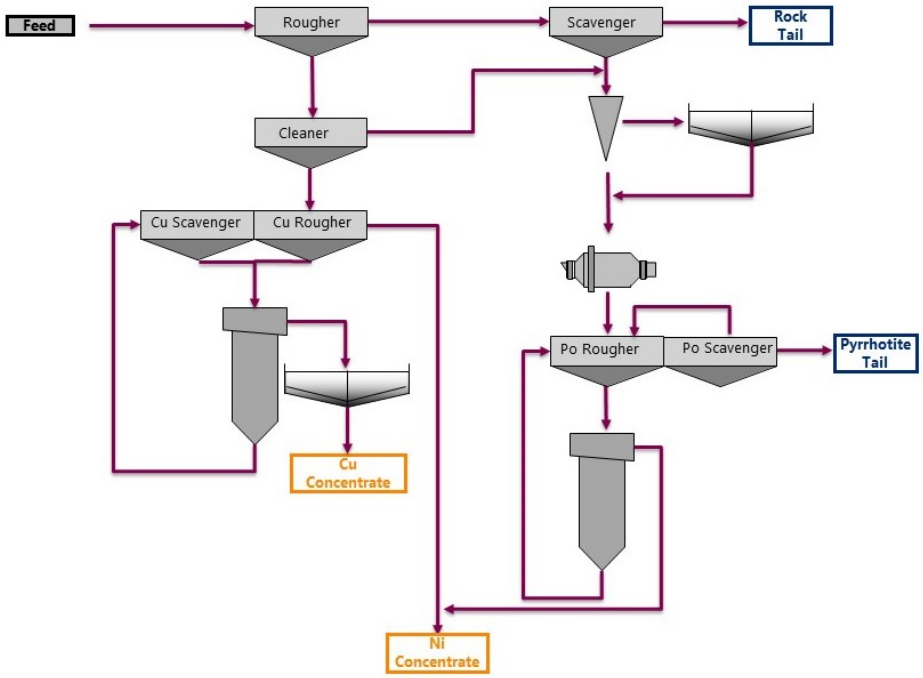

Figure 2-12. Clarabelle Mill flowsheet [90].

The Clarabelle Mill flowsheet is shown in Figure 2-12. In Clarabelle Mill flotation process, the primary goal of the rougher and cleaner is to maximize copper and nickel recovery while maintaining a high-grade rougher concentrate (15% Cu+Ni) and a high-grade cleaner concentrate (23% Cu+Ni). The cleaner concentrate is further separated to the copper concentrate and nickel concentrate via the copper/nickel separation circuit. Meanwhile, the cleaner tail and the scavenger concentrate are combined to the regrind circuit, in which circuit the mineral particles are reground to further liberate valuable sulfide minerals from the waste minerals. For the well liberation of valuable sulfide minerals, the product grind target of the regrind circuit is a P_{80} (product size, 80% passing) of 60 microns. The reground stream is then feed into the pyrrhotite rejection circuit to recover the liberated valuable minerals while rejecting as much pyrrhotite as possible. The pyrrhotite cleaner concentrate from the pyrrhotite rejection circuit, together with the copper rougher tail, become the final

nickel concentrate. For more details about the milling practice and the flotation circuit of the Clarabelle Mill, please refer to the Canadian Milling Practice 2020 [90].

2.4.6. The Rationale of this Work

All these above strategies mentioned can improve the flotation selectivity of hexagonal pyrrhotite from pentlandite to some extent. But some chelates, which are powerful in heightening the flotation selectivity of hexagonal pyrrhotite from pentlandite, can cause environmental concerns and require significant effort to deal with. For example, the use of DETA can lead to high concentrations of Ni^{2+} and Cu^{2+} in the final effluent over the regulated amount since DETA can form stable chelates with Ni^{2+} and Cu^{2+}, which kept them from being precipitated with lime treatment. Also, the need for pyrrhotite rejection would become increasingly intense due to the depleting head grade of valuable minerals in the feeding ores, which is calling for more effective pyrrhotite rejection measures. Exploring more effective measures for pyrrhotite depression requires a fundamental understanding of their flotation behaviors since their complex flotation system presented numerous directions to move ahead. For example, there is still a debate about the desirable chemical environment for separating pentlandite from pyrrhotite using flotation. Some researchers have claimed that a reducing environment helps to suppress xanthate oxidation on the pyrrhotite surface, rendering pyrrhotite more hydrophilic and less floatable [80, 91]. Other researchers have reported that an oxidizing environment plays a crucial role in the flotation separation of pyrrhotite and pentlandite [59, 92]. A fundamental understanding of their oxidation behaviors and controlling parameters is of crucial importance for directing the exploration. Therefore, fundamental studies, like this study, would be beneficial for future explorations.

Chapter 3. The Role of Cu Ion Activation and Surface Oxidation for Polymorphic Pyrrhotite Flotation Performance in Strathcona Mill

Abstract:

In the Strathcona Mill, the rejection of pyrrhotite ($Fe_{(1-x)}S$, $0< x \leq 0.125$) is in high demand to meet the stringent environmental standards for SO_2 emission in downstream smelting operations. For this purpose, two plant surveys were conducted to study polymorphic pyrrhotite flotation and depression mechanisms in the Strathcona Mill via investigating polymorphic pyrrhotite distributions, pulp chemistry, and industrial settings (with combined Cu-Ni feed and split Cu-Ni feed). The plant survey data revealed that hexagonal pyrrhotite in the Ni concentrate demonstrated higher floatability than the monoclinic pyrrhotite. The different oxidation rates of monoclinic and hexagonal pyrrhotite were investigated. CV studies corroborated the higher floatability of hexagonal pyrrhotite with its lower oxidation rate than monoclinic pyrrhotite. XPS studies demonstrated the progressive oxidation of pyrrhotite from concentrate to tail, substantiating that pyrrhotite oxidation is essential for pyrrhotite depression. ToF-SIMS tests showed the copper activation effects on pyrrhotite. This study suggested that careful control of Cu ions in the Ni stream and proper ways to relatively increase pyrrhotite oxidation rate (particularly for hexagonal pyrrhotite) would help depress pyrrhotite.

Keywords: Polymorphic Pyrrhotite, Plant Surveys, Flotation, Surface Characterization, Copper Activation

3.1. Introduction

Nickel is an important metal, an essential component in various industries, including alloys, batteries, catalysts, coins, and electronic devices. In the Sudbury Basin, pentlandite, a major economic nickel-rich sulfide ($(Ni,Fe)_9S_8$), is usually associated with abundant pyrrhotite, an iron sulfide ($Fe_{(1-x)}S$, $0< x \leq 0.125$). Due to increasingly stringent regulations

on the SO_2 emission from nickel concentrate downstream smelter operations, sulfur and iron content in the Ni concentrate needs to be limited during the mineral processing. As pyrrhotite is a gangue sulfide with no current economic value, it must be rejected wherever possible. Ironically, it was once recovered due to the small amount of nickel content naturally found within its crystal structure (pyrrhotite in Sudbury Contact ore contains 1.07% Ni) [93, 94].

With a NiAs unit cell (see Figure 2-1), Pyrrhotite is non-stoichiometric and often exists as several polytypes of hexagonal and monoclinic crystal symmetries [95]. Among these, four naturally occurring pyrrhotites are separated into two categories based on their crystal symmetries: 1. 4C (Fe_7S_8) monoclinic pyrrhotite; 2. 5C (Fe_9S_{10}), 6C ($Fe_{11}S_{12}$), and 11C ($Fe_{10}S_{11}$) hexagonal pyrrhotite. Here, the number before C indicates the number of unit cells in the "C" direction needed for defining a superlattice with iron vacancies [3-5]. Iron deficiencies can result in distinctions in their magnetic properties since iron vacancies lower the balance between ferromagnetically oriented moments and coupled moments from alternate layers [5]. Therefore, defect-rich monoclinic pyrrhotite shows strong ferromagnetic behavior, while hexagonal pyrrhotite, with lower iron vacancies, shows weak or non-magnetic behavior [96, 97].

Among all factors that may affect pyrrhotite flotation, the following are three factors of great significance: crystal structure, Cu activation, and galvanic interactions [42, 95, 98]. In pyrrhotite crystal, iron deficiencies are surrounded by Fe^{3+} to maintain charge neutrality, theorized as an internal oxidant in the pyrrhotite crystal structure. Moreover, iron deficiencies are also believed to be helpful for electron transferring, facilitating pyrrhotite oxidation reactions [21, 22, 40]. It is consistent with the phenomenon shown by numerous research investigations and plant practices that hexagonal pyrrhotite has a lower oxidation

rate and higher floatability than monoclinic pyrrhotite [38, 82, 98]. Differences in crystal structures also brought differences in their response to copper activation. Both Becker [98] and Kalahdoozan [19] showed that pyrrhotite of different superstructures exhibits a different response to copper activation. These differential Cu activation effects have been extensively discussed in the fundamental research of this paper, and it would be beneficial to investigate further and understand the underlying mechanisms. Furthermore, studies have shown the drastic effect of galvanic interactions on pentlandite and pyrrhotite during their flotation separation. During galvanic interaction, pentlandite will serve as the host for anodic reactions of xanthate and pyrrhotite as the host for cathodic reactions of oxygen, leading to better flotation selectivity in a low redox potential solution [42].

Due to the difference in their crystal properties, hexagonal and monoclinic pyrrhotite may require distinct methods for their individual rejections [82, 95]. The ferromagnetic property and relatively high surface oxidation rates of monoclinic pyrrhotite render effective flotation separation of monoclinic pyrrhotite from pentlandite via magnetic separation [89] and the low redox flotation practice [91]. However, an efficient depression strategy for hexagonal pyrrhotite is still not in place for industrial applications. Some of the promising depression methods include 1) the manipulation of pulp potential by N_2 purging [80], which promotes the anodic oxidation of xanthate on pentlandite surface as stated before, 2) surface deactivation with the combination of DETA or TETA and SMBS [81, 92] or the combination of DETA and highly oxidizing conditions [99], 3) starving xanthate conditioning to improve the selective adsorption of xanthate [20]. Among these depression strategies, magnetic separations and starving xanthate conditioning have been widely used. Although DETA/TETA + SMBS demonstrated optimum depression effects for pyrrhotite, its applications were limited by environmental concerns. The environmental concern is that DETA/TETA has powerful chelating effects with metal ions, preventing metal ions in the

wastewater from being precipitated out in the traditionally used alkaline conditions [81, 92, 100]. Therefore, for further developing preliminary depression strategies for pyrrhotite, hexagonal pyrrhotite especially, flotation performance and mechanisms of polymorphic pyrrhotite in Strathcona Mill were investigated.

Sudbury Basin is a major source in the production of nickel and copper. In 2017, Glencore produced about 109,100 tonnes of nickel [101], which is about 5.2% of the total nickel production in the world. The Strathcona Mill, located in Sudbury Basin, processes a blend of ores from Nickel Rim South and Fraser [94]. Among all feed ores, pyrrhotite grade varies from 3 to 6% in Cu-rich ores and ranges from 20 to 25% in low Cu grade ore [94]. Recently, feed ores have seen higher pyrrhotite content, especially hexagonal pyrrhotite, in their feed ores. The high pyrrhotite content in the feed ore is a significant issue that needs to be addressed immediately.

The lack of an effective depression strategy for hexagonal pyrrhotite leads to the necessity to develop a better fundamental understanding of pyrrhotite flotation. Meanwhile, the development of new fundamental theories is restricted by existing contradictions that arise from investigations using samples with different mineralogies (including mineral localities, nickel contents, and ore types etc.) [40, 98]. Therefore, new findings must be organized appropriately to their applicable orebody. Thorough understanding of the overall flotation behaviors of pyrrhotite and valuable sulfide mineral flotation performances and flotation conditions in Strathcona Mill are foundations and starting points for fundamental studies of pyrrhotite flotation, helping for developing more effective pyrrhotite rejection methods in Strathcona Mill. In this study, two plant surveys were conducted in 2016 and 2017. During these two plant surveys, size-by-size mineralogy, liberation, recovery analysis, and total mass balance were obtained via Quantitative Evaluation of Materials by Scanning

Electron Microscopy (QEMSCAN) analysis and sampled pyrrhotite surface was characterized by XPS and ToF-SIMS. The information listed above aimed to identify and understand the polymorphic pyrrhotite flotation differences in Strathcona Mill.

3.2. Strathcona Mill Flowsheets

The ore feeding strategies were different for the 2016 and 2017 plant surveys. For the 2016 plant survey, all feed ores were combined and fed into the primary nickel rougher circuit as the nickel feed. For the 2017 plant survey, feed ores with high Cu grade were fed into the copper pre-float circuit, tails from which were dealt in a primary copper rougher circuit (Figure 3-1), and feed ores with low Cu grade were fed into the primary nickel rougher circuit as nickel feed.

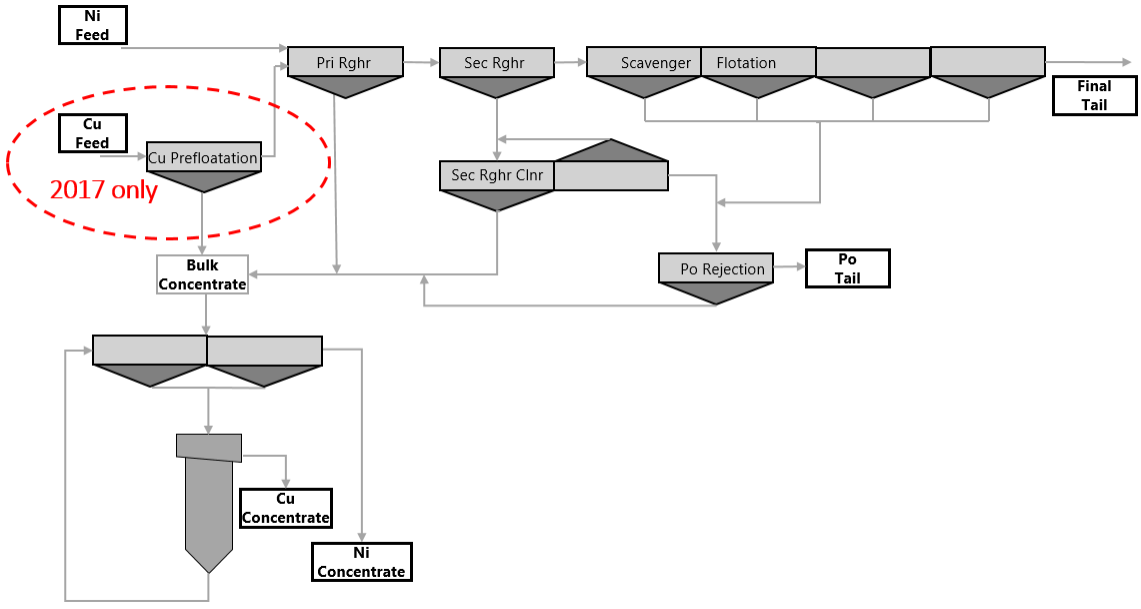

Figure 3-1. Flowsheet for 2016 and 2017 plant survey (Pri Rghr- primary Cu/Ni rougher, Sec Rghr- secondary rougher) [102].

For both 2016 and 2017 plant surveys, Cu and Ni sulfide minerals in the nickel feed were first recovered in a primary nickel rougher circuit, and remnant valuable sulfide minerals were then retrieved via a combination of a secondary rougher and a secondary rougher cleaner, leaving the rest valuable sulfide minerals fed in the scavenger circuits. Meanwhile, the primary copper rougher tail in the 2017 plant survey was combined with the primary nickel rougher tail and fed into the secondary rougher together. Scavenger concentrate was reground to further liberate valuable sulfide minerals and then fed into pyrrhotite rejection flotation circuits to recover pentlandite. Tails from the pyrrhotite rejection circuits were usually called pyrrhotite tails, and tails from the scavenger circuit were named final tails. All recovered concentrate (including the primary nickel rougher concentrate, the secondary rougher cleaner concentrate, the pyrrhotite rejection concentrate, and together with two other concentrates for the 2017 plant survey – the copper pre-float concentrate and the primary copper rougher concentrate) were fed into copper cleaner flotation columns, producing copper concentrate and nickel concentrate.

3.3. Experimental Procedures and Methods

3.3.1. Sampling Procedures

For representative sampling, the two-hour survey unit was performed, within which 16 cuts were taken of every surveyed stream. Slurries collected were used for mass balancing, as well as for QEMSCAN.

For SIMS and XPS tests, the slurry was collected with a different campaign as samples used for those tests are easily affected by oxidation. Slurry collected from sampling locations were filled in specimen tubes (50 ml conical polypropylene centrifuge tubes) and then deoxygenated by bubbling nitrogen for 5 minutes. Immediately after, the samples were frozen with liquid nitrogen and delivered for further analysis. All sampling was

conducted when the plant was in a stable operating state, which helps to make the collected samples representative enough.

Frozen samples prepared for analysis got defrosted at room temperature, and N_2 was kept bubbling in to avoid further oxidation. Defrosted samples were washed five times with nitrogen purged Milli-Q water and then frozen in oxygen-free Milli-Q water and dried in a freeze-dryer.

3.3.2. Sample Characterization

For preparing pyrrhotite samples used for surface analysis, well-dried samples were undergone a magnetic separation process, during which only a hand-magnet was used. Pyrrhotite samples' purity was further confirmed with XRD (Rigaku XRD Ultima IV) and X-ray fluorescence (XRF, Orbis PC Micro-XRF Elemental Analyzer) tests. The XRD test results were analyzed with the MDI Jade software.

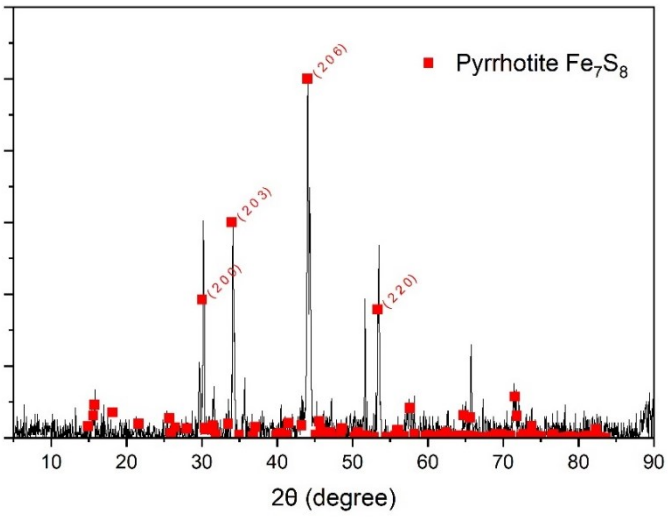

Figure 3-2. Powder XRD results of the pyrrhotite in the primary nickel rougher concentrate of the 2016 plant survey (ToF-SIMS sample) using CuKα radiation and the reference from the Joint Committee on Powder Diffraction Standards (JCPDS) Powder Diffraction File (PDF) database (PDF-71-0647).

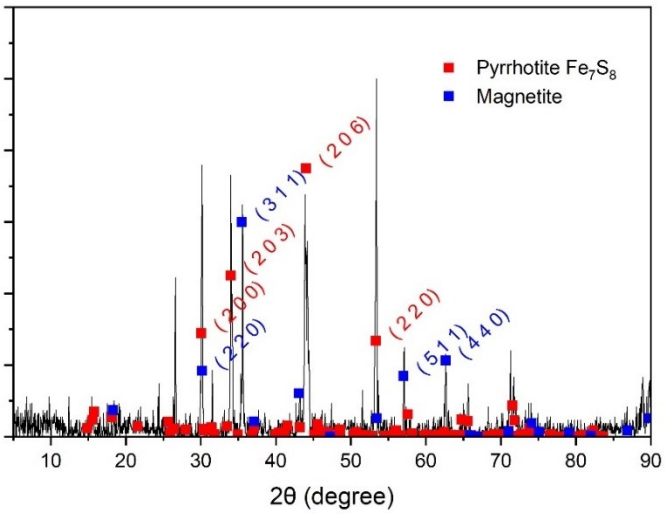

Figure 3-3. Powder XRD results of the pyrrhotite in the Primary nickel rougher tail of 2016 plant survey (ToF-SIMS sample) using CuKα radiation and the reference from the JCPDS database (PDF-71-0647 for pyrrhotite and PDF-88-0866 for magnetite)

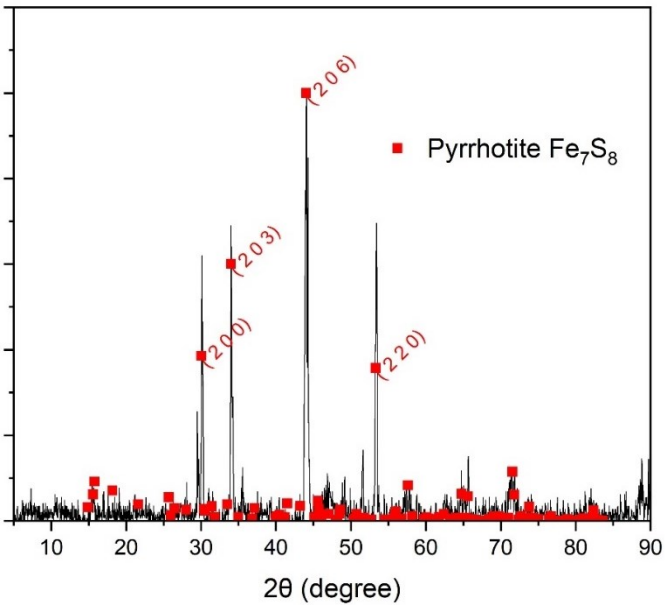

Figure 3-4. Powder XRD results of the pyrrhotite in the Primary nickel rougher concentrate of 2017 plant survey (XPS sample) using CuKα radiation and the reference from the JCPDS database (PDF-71-0647)

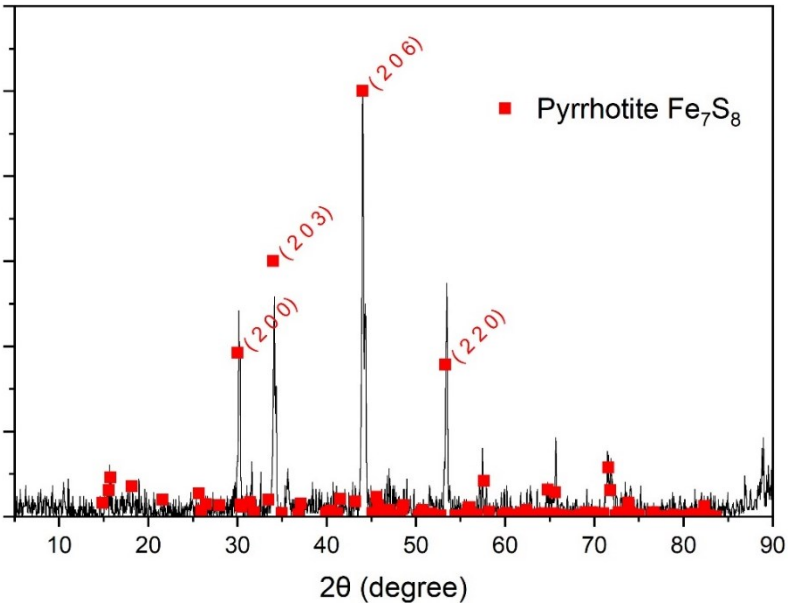

Figure 3-5. Powder XRD results of the pyrrhotite in the Primary nickel rougher tail of 2017 plant survey (XPS sample) using CuKα radiation and the reference from the JCPDS database (PDF-71-0647)

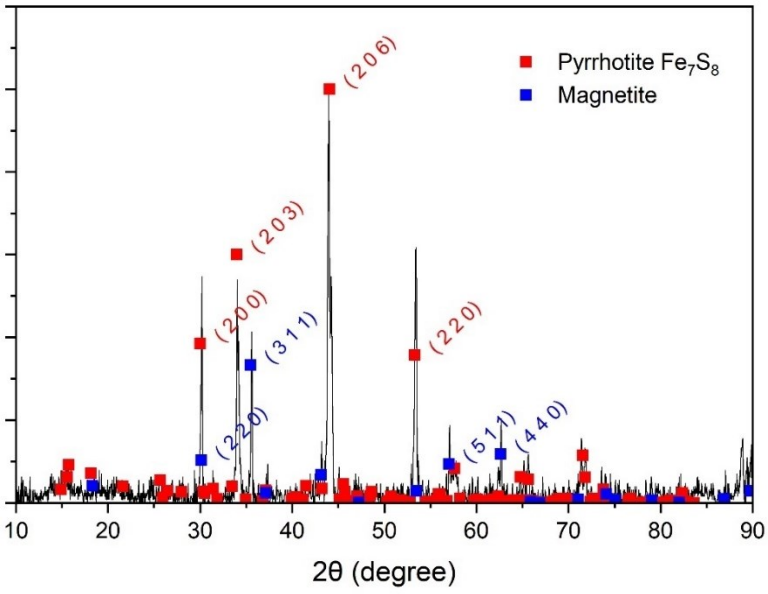

Figure 3-6. Powder XRD results of the pyrrhotite in the pyrrhotite tail of 2017 plant survey (XPS sample) using CuKα radiation and the reference from the JCPDS database (PDF-71-0647 for pyrrhotite and PDF-88-0866 for magnetite)

Table 3-1. The XRF results of the pyrrhotite in the primary nickel rougher concentrate and primary nickel rougher tail

Element	2016 Plant survey (ToF-SMS Samples)		2017 Plant Survey (XPS Samples)		
	PRC	PRT	PRC	PRT	PT
S	38.40	30.74	38.96	36.35	33.03
Fe	57.28	65.89	57.29	61.37	64.13
Ni	2.45	0.87	2.18	1.29	0.65
Cu	0.80	0.12	0.70	0.32	0.10
Ca	0.18	0.38	0.13	0.14	0.44
Al	0.24	0.40	0.25	0.22	0.41
Si	0.49	1.29	0.48	0.30	1.23
Mn	0.08	0.17	0.00	0.00	0.00
K	0.08	0.14	0.00	0.00	0.15
Total	100.00	100.00	100.00	100.00	100.00

According to Figure 3-2, Figure 3-3 and Table 3-1, the purity of pyrrhotite is reasonably high for the ToF-SIMS tests, but the pyrrhotite in the primary nickel rougher concentrate got slight amount of magnetite, which means extreme care need to be taken when picking the particle for the ToF-SIMS tests. While, Figure 3-4, Figure 3-5, Figure 3-6, and Table 3-1 showed that the purity of pyrrhotite should be good enough for the XPS tests. Extreme care needs to be taken when checking the spectra of Fe and O for the pyrrhotite sample in the pyrrhotite tail since the slight amount of magnetite inside the sample also contributed to their peak intensity.

3.3.3. Mineralogy Analysis by QEMSCAN

Sampled mineral particles were separated into several size ranges- +106μm, -106/+53μm, -53/+25 μm, -25/+8 μm, -8/+3 μm, and -3 μm with sieves and hydrocyclones. Appropriate graphite size was selected for each size fraction and then mixed with its corresponding

sample particles. Sample/graphite mixtures were prepared via thoroughly mixing, and extreme care was taken to avoid de-agglomeration of fines. The sample/graphite mixture and the mixture of epoxy and hardener were stirred until uniform and cured after removing bubbles. After scrupulous grinding and polishing, samples were coated with carbon and sent for analysis.

Samples were analyzed with Cameca SX-100 Microprobe, coupled with five higher resolution wavelength dispersive spectrometers (WDS). Its detection limits can reach as low as 100 ppm. Detailed compositional data was then imported back into the QEMSCAN software to further refine the elemental deportment and size-by-size liberation calculations. The ratio of the hexagonal pyrrhotite over monoclinic pyrrhotite in the sample was determined via the high resolution XRD tests (Bruker D8 Advance XRD). The example tests were described in detail in Section B.1.2 Single Mineral Characterization. Mineralogy analysis, including QEMSCAN and high resolution XRD tests and analysis, was done by Kormos.

3.3.4. Surface Characterization

Time-of-Flight Secondary Ion Mass Spectrometry (ToF-SIMS)

ToF-SIMS allows for the compositional mapping of pyrrhotite, which was conducted on an ION-TOF ToF-SIMS IV (ION-TOF, Munster, Germany) equipped with a bismuth liquid ion source. The primary ion beam (Bi^{3+}) was operated at 25 keV in a static Burst alignment mode with a primary pulsed beam current of 0.5 pA.

X-ray Photoelectron Spectroscopy (XPS)

The X-ray photoelectron spectroscopy (XPS) analysis, used to investigate pyrrhotite surface oxidation, was performed with Kratos Analytical AXIS 165 with a

monochromatized Al Kα source (hν = 1486.6 eV). Spectra were referenced with a binding energy of C *1s* (284.8 eV) to ensure that the binding energy shift due to charging gets calibrated.

Cyclic Voltammetry (CV) Studies

Pyrrhotite electrodes were prepared from natural massive specimens (pyrrhotite solids, not ground particles). Monoclinic pyrrhotite was from Sudbury, Ontario, Canada, and hexagonal pyrrhotite came from Virginia, America. Pyrrhotite electrodes were prepared by gluing the copper wire onto one end of the mineral piece with the Leitsilber 200 silver paint. The piece glued together were then encased in non-conductive epoxy (West System 105 epoxy resin and 205 hardener) using a specifically designed PTFE cylinder mold (5mm diameter × 12 mm deep).

Pyrrhotite electrodes were tested in secondary electron microscopy with Backscattered electron imaging (BSE) and energy dispersive X-ray spectrometer (EDX) after grinding and polishing to ensure their purity is good enough for CV. For the relative purity of the electrodes, please check Appendix A.5 Pyrrhotite Electrode Purity.

CV tests were performed in a pH 9.2 borax buffer solution (0.05 M $Na_2B_4O_7$). Prior to the electrochemical tests, the solution was purged with N_2 for 15 mins to remove oxygen. A new electrode surface was prepared by wet grinding on a 1200 grid silicon carbide. The polished electrode was then immediately transferred into the de-oxygenated borax buffer solution. The potential scanning was commenced from an open circuit potential towards negative potential at a 20 mV/s scan rate for removing possible surface oxidation.

3.3.5. Inductively Coupled Plasma Optical Emission Spectroscopy (ICP-OES) Tests

Ion concentration in sampled streams was directly determined by ICP-OES (Thermo Scientific iCAP 6500 ICP-OES CID Spectrometer) after removing solids in sampled streams.

Different digestion procedures were applied based on their mineral composition. For sulfide dominated samples (i.e., copper concentrates), they were dissolved in 95 ℃ aqua regia (at a 0.1g/20ml concentration for 2 hours); for samples containing many insoluble minerals, they were sintered by sodium peroxide (Na_2O_2) fusion at 650 ℃ in Zirconia crucibles and digested in a 5% nitric acid.

3.4. Results and Discussion

3.4.1. Polymorphic Pyrrhotite Floatability in Plant Surveys

Recovery Difference of Hexagonal and Monoclinic Pyrrhotite

As described in Figure 3-7, the distribution of polymorphic pyrrhotite in the final four products of Strathcona Mill demonstrates that a higher recovery of hexagonal pyrrhotite reported in the Cu concentrate and Ni concentrate than monoclinic pyrrhotite. The relative proportion of the hexagonal pyrrhotite and monoclinic pyrrhotite was determined via the ratio of the peak intensity at 51.40 (2θ) to the peak intensity at 51.75 (2θ) in the XRD tests using CoKα radiation (for details, please referred to Appendix B.1.2 Single Mineral Characterization.

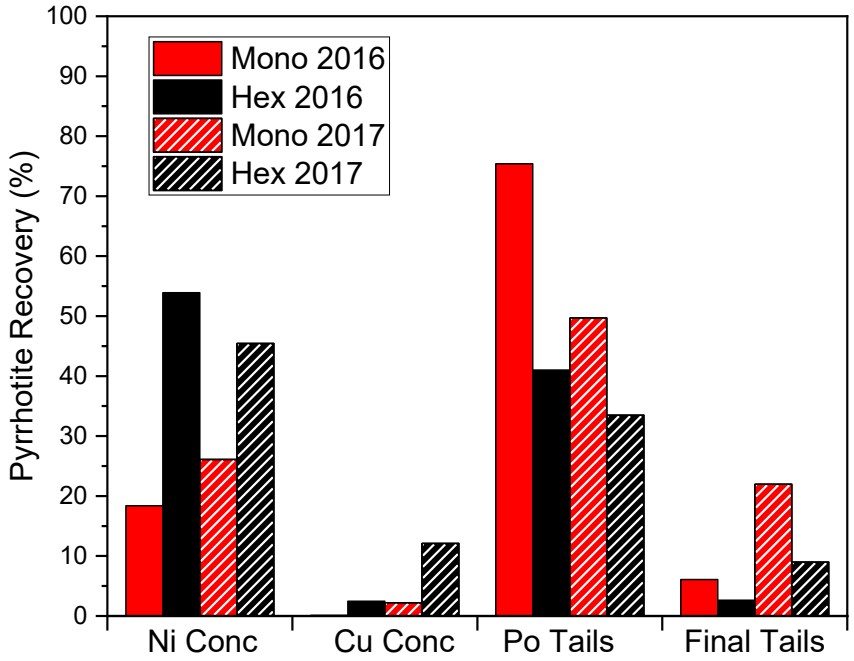

Figure 3-7. Comparison of monoclinic and hexagonal pyrrhotite recovery in final four products of 2016 and 2017 plant surveys: Ni concentrates, Cu concentrates, Po Tails and Final tails

Polymorphic Pyrrhotite Liberation in Ni Concentrate

As the liberation information of iron sulfide from Ni concentrate shown in Figure 3-8, pyrrhotite reported into nickel concentrate was well-liberated and mainly distributed in the 8 to 53 μm size ranges. Since the liberation of pyrrhotite reported into nickel concentrate did not seem to be a problem (Figure 3-8), higher recovery of hexagonal pyrrhotite than monoclinic pyrrhotite could be attributed to their floatability differences, which were further explained in following XPS analysis and CV studies.

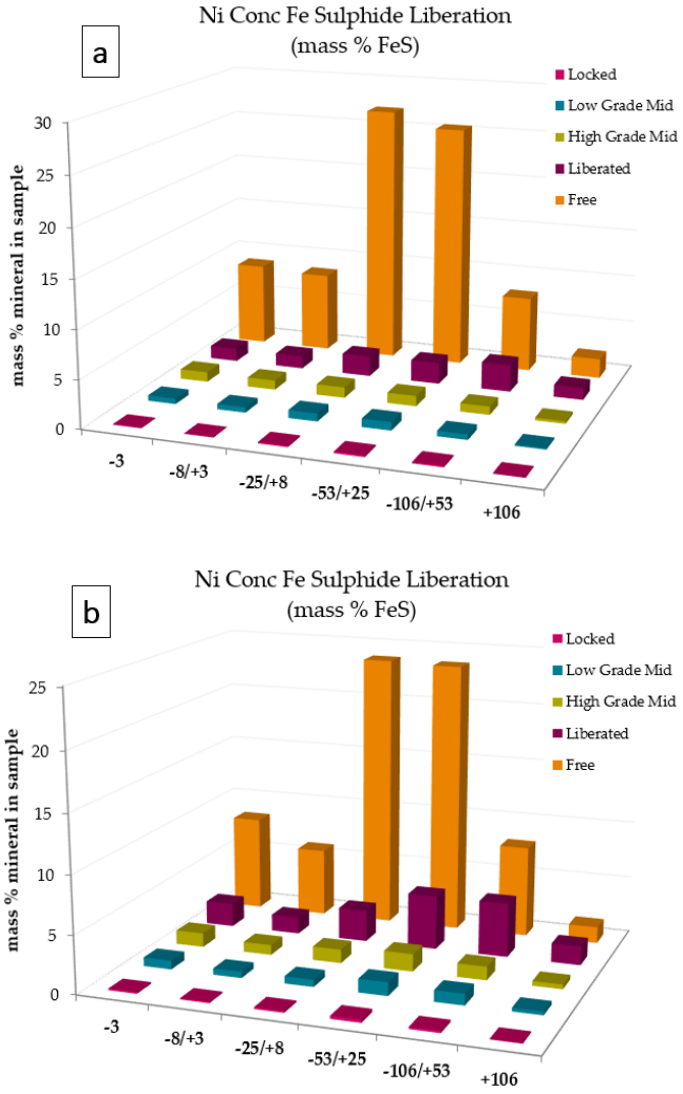

Figure 3-8. Liberation of iron sulfide in nickel concentrate for 2016 (a) and 2017 (b) plant surveys.

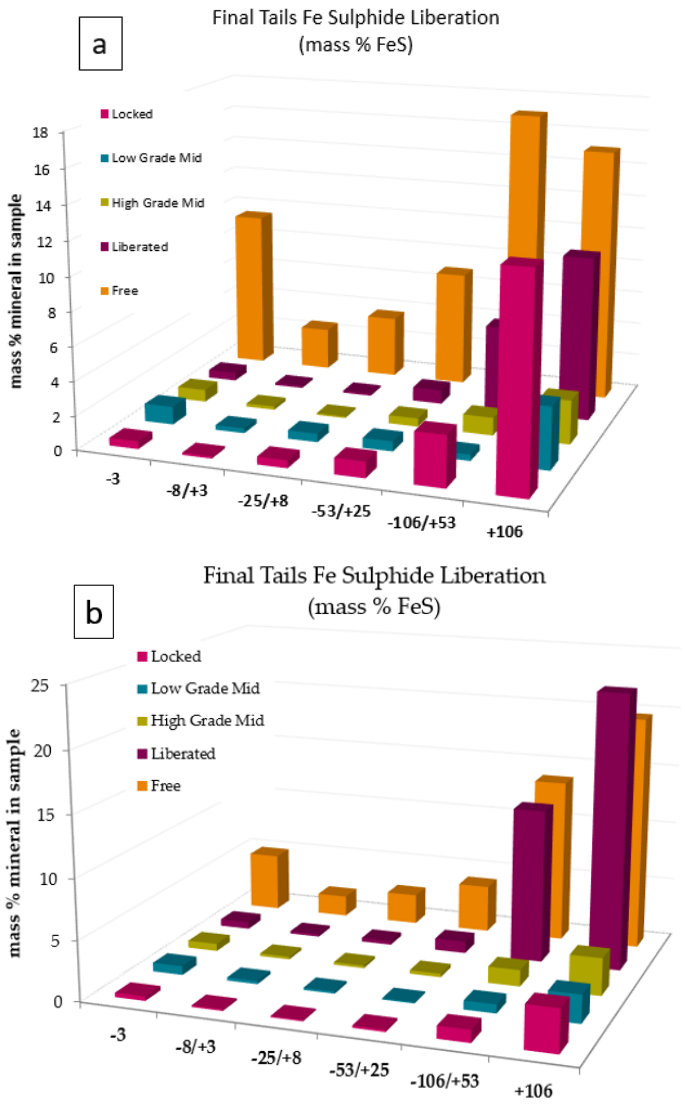

Figure 3-9. Liberation of iron sulfide in final tails for 2016 (a) and 2017 (b) plant surveys.

The higher floatability of hexagonal pyrrhotite than monoclinic pyrrhotite was also reflected by the higher distribution of monoclinic pyrrhotite in final tails than that of hexagonal pyrrhotite (Figure 3-7). In both plant surveys, most iron sulfide minerals in the final tails were well-liberated and mainly distributed in the -106/+53 and +106 µm size ranges (Figure 3-9). As the purpose of the scavenger is to recover all major sulfide minerals to the pyrrhotite rejection circuit, any losses to the final tails should be due to a lack of liberation from the silicates or extreme low floatability. In both plant surveys, the liberation

of iron sulfides is reasonably high. Given the degree liberation (Figure 3-9) and the high distribution of monoclinic pyrrhotite in the final tails (see Figure 3-7), it is also reasonable to say that monoclinic pyrrhotite was more difficult to float than the hexagonal pyrrhotite.

Decreased Recovery of Hexagonal Pyrrhotite in Primary Nickel Rougher in the 2017 Plant Survey

Separating the Cu-rich feed in the 2017 plant survey had a surprising impact on hexagonal pyrrhotite flotation recovery in the primary nickel rougher circuit. Both chalcopyrite and pentlandite entering the primary nickel rougher feed were of similar grade (both of which were around 4%). However, the pyrrhotite grade of nickel feed is around 19% in 2016 and 30% in 2017. Accompanied with variations in nickel feed ore were variations of major sulfide mineral recoveries in the primary nickel rougher concentrate. All major sulfide mineral recoveries in the primary nickel rougher feed of the 2017 plant survey dropped compared to those of 2016.

Among them, hexagonal pyrrhotite flotation recovery in the primary nickel rougher concentrate dropped much more severely than that of monoclinic pyrrhotite (17.58% monoclinic and 53.53% hexagonal pyrrhotite recovered in primary nickel rougher for 2016 plant survey, 11.01% monoclinic and 22.03% hexagonal pyrrhotite in 2017 plant survey). Note that pyrrhotite recovery inside primary nickel rougher concentrate refers to the percentage of pyrrhotite reported from nickel feed to the primary nickel rougher concentrate. The reason for the large difference in hexagonal pyrrhotite flotation recovery is, in part, related to the surface interaction of both pyrrhotites with the ions found in the pulp. The influences of ions will be further discussed in the following pyrrhotite surface characterization (ToF-SIMS and XPS studies) and pulp chemistry analysis (ICP) sections.

3.4.2. Surface and Chemistry Analysis

ToF-SIMS Studies

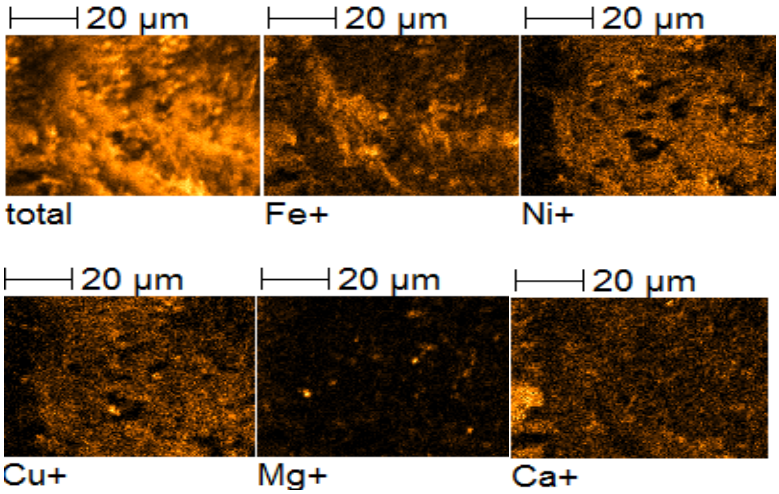

Figure 3-10. Positive ion ToF-SIMS images of pyrrhotite in the primary nickel rougher concentrate for the 2016 plant survey

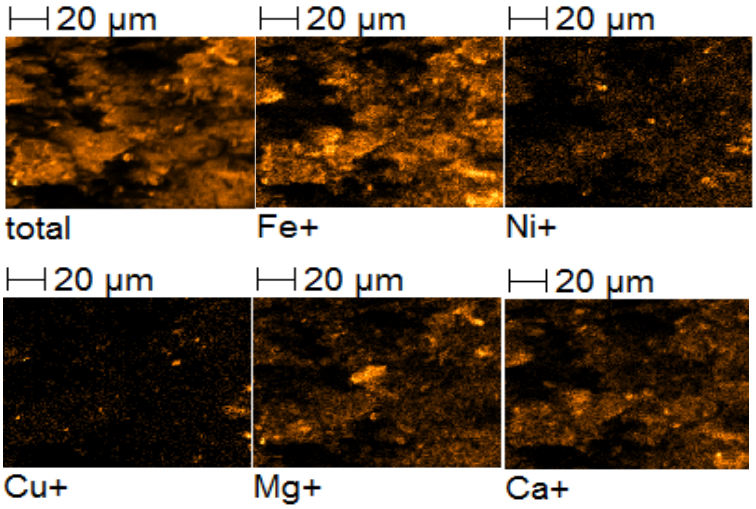

Figure 3-11. Positive ion ToF-SIMS images of pyrrhotite in the primary nickel rougher tail for the 2016 plant survey

The metal ions found on the pyrrhotite grains in the primary nickel rougher concentrate and primary nickel rougher tails were investigated using ToF-SIMS. A rough comparison

between the major ions (Cu, Ni, Mg, Ca) images (Figure 3-10 and Figure 3-11) on surfaces of pyrrhotite in the primary nickel rougher concentrate and the primary nickel rougher tail showed that the amount of copper and nickel found on surfaces of pyrrhotite in primary nickel rougher concentrate was much greater than those found in the primary nickel rougher tail. However, it is hard to tell the variation of Ca and Mg simply based on these four figures. One important thing that needs to be noted is that extreme care needs to be taken when picking the pyrrhotite particles for the ToF-SIMS tests because the purity of the sample, particularly the pyrrhotite in the primary nickel rougher tail, could hardly be ensured solely by the magnetic separation. The purity of the pyrrhotite in the primary nickel rougher concentrate is quite well for the ToF-SIMS tests, which can be seen from Figure 3-2 and Table 3-1. In contrast, the pyrrhotite in the primary rougher tail contains a slight amount of magnetite (Figure 3-3 and Table 3-1), which means that the spot with low intensity of O^- relative to S^- needs to be selected for the ToF-SIMS tests before conducting the positive ToF-SIMS tests.

Table 3-2. The intensity ratio of Mg, Ca, Ni, and Cu to Fe when sputtering the surfaces of pyrrhotite from different streams.[2]

Assignment	Pyrrhotite			
	Mg/Fe	Ca/Fe	Ni/Fe	Cu/Fe
PNRC	0.16	0.30	0.57	0.32
PNRT	0.44	0.60	0.12	0.03

[2] PNRC – Pyrrhotite in the primary nickel rougher concentrate;

PNRT – Pyrrhotite in the primary nickel rougher tail.

For comparing the relative concentration of these four major elements, the intensity of their major mass fragments was used to calculate the ratio of Mg, Ca, Ni, and Cu to Fe on pyrrhotite surfaces in different streams (Table 3-2).

Table 3-2 shows the relative ratio of Mg, Ca, Ni, and Cu to Fe based on the intensity ratio of their major mass fragments. The comparison of pyrrhotite surfaces in the primary nickel rougher concentrate and the primary nickel rougher tail showed that Mg and Ca concentrations were lower on pyrrhotite surfaces in the primary nickel rougher concentrate than that in the primary nickel rougher tail. Meanwhile, the amount of Cu and Ni was more on pyrrhotite surfaces in primary nickel rougher concentrate than those found in the tail. The results suggest that Mg and Ca are helpful for pyrrhotite depression, while Cu and Ni are helpful for pyrrhotite flotation.

Plant Water Solution Species Analysis

Metal ions concentration in sampled slurries were investigated to further establish the connection between pyrrhotite floatation performances and metal ions concentration, as shown in Figure 3-12. ToF-SIMS studies showed that Cu, Ni, Ca and Mg were four major influential metal cations for pyrrhotite flotation/depression. There were nearly no apparent differences in the concentration of Ca and Mg in the nickel feed of these two plant surveys, but significant differences for Cu, Ni, and Fe (Figure 3-12). ToF-SIMS analysis showed that pyrrhotite with a high Cu and Ni concentration on its surface reported to the primary nickel rougher concentrate while pyrrhotite with low Cu and Ni concentrations reported into the primary nickel rougher tails. Therefore, the lower copper and nickel ion concentration in the nickel feed of the 2017 plant survey than in the nickel feed of 2016 plant survey could be one important reason for the lower pyrrhotite flotation recovery in the primary nickel rougher concentrate of the 2017 plant survey.

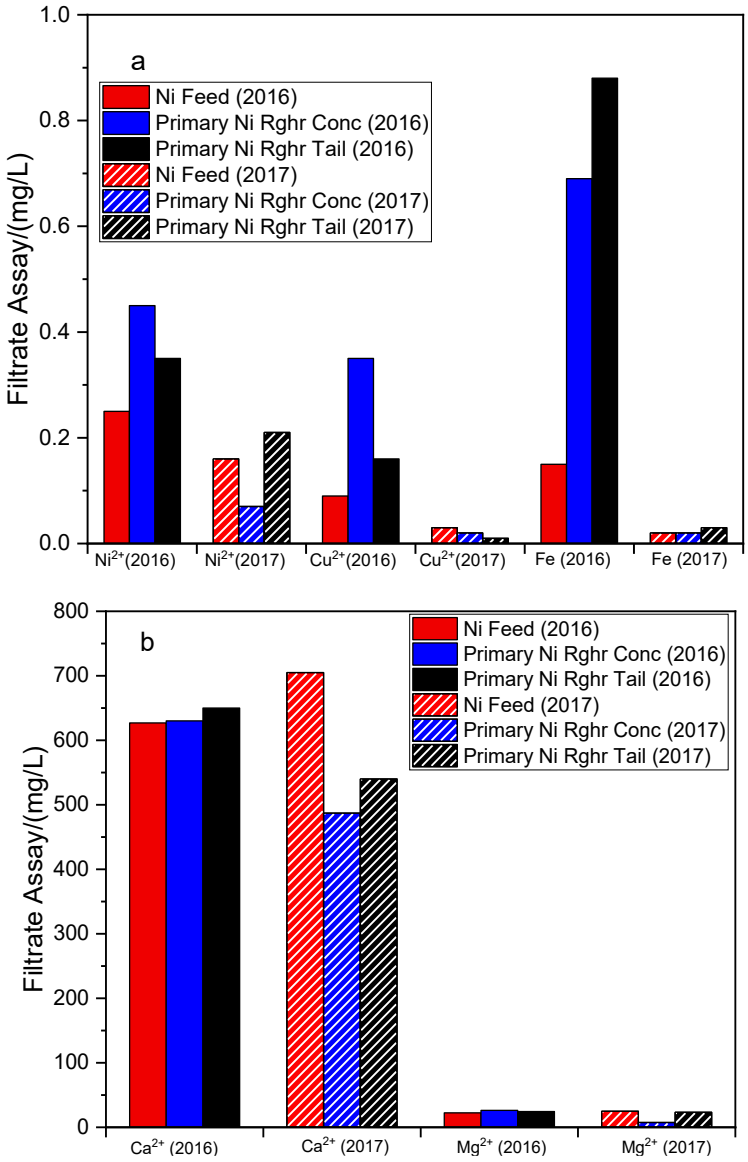

Figure 3-12. Inductively coupled plasma (ICP) analysis of the filtrate in the nickel feed, the primary nickel rougher concentrate and the primary nickel rougher tail for two plant surveys. (a) Ni^{2+}, Cu^{2+}, and Fe; (b) Ca^{2+} and Mg^{2+}.

As to the significant drop of hexagonal pyrrhotite flotation recovery in the primary nickel rougher concentrate (from 53.53% in 2016 to 22.03% in 2017) than that of monoclinic pyrrhotite (from 17.58% in 2016 to 11.01% in 2017), it could be due to the higher Cu

activating effects on hexagonal pyrrhotite than that of monoclinic pyrrhotite. According to Becker's research, Cu activation effects on Sudbury non-magnetic pyrrhotite are much more apparent than that of Sudbury magnetic pyrrhotite [98].

XPS Studies

For understanding the flotation performance of pyrrhotite in the primary nickel rougher circuit, the pyrrhotite in the sampled streams were characterized by XPS analysis.

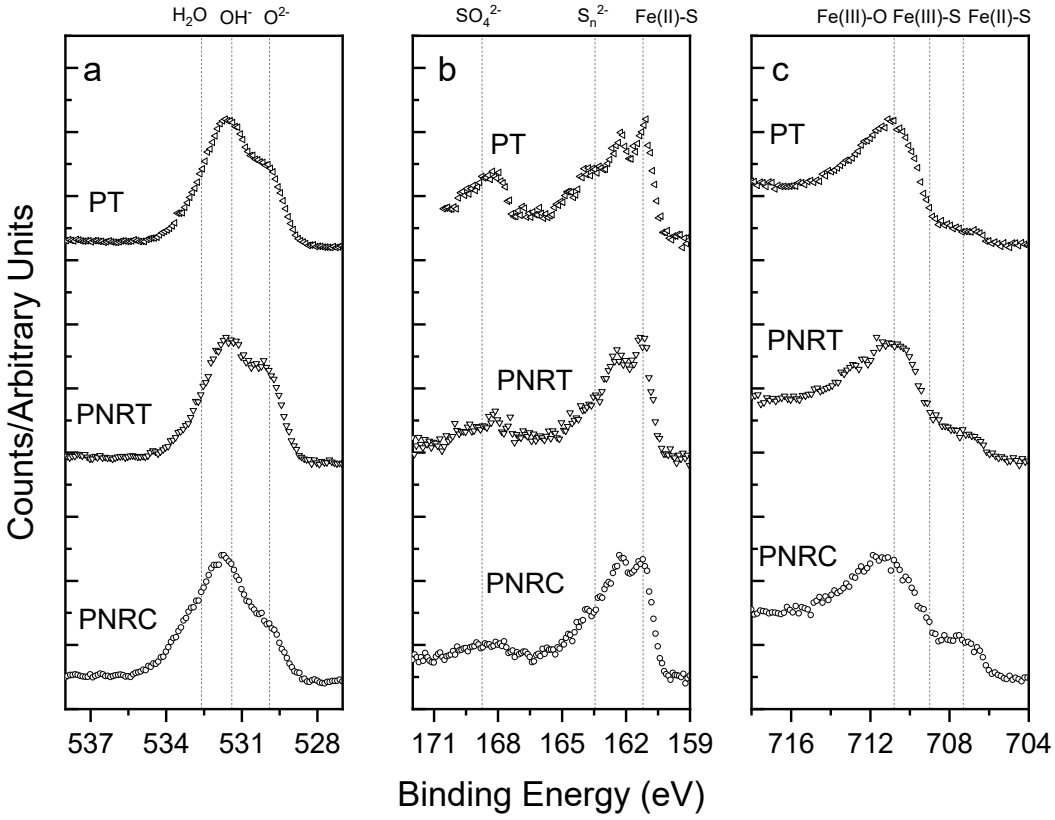

Figure 3-13. Overlays of the O *1s* (a), S *2p* (b), and Fe *2p3/2* (c) XPS narrow region scans of Strathcona Mill survey samples for the 2017 plant survey.[3]

[3] PNRC - Pyrrhotite in the primary nickel rougher concentrate;

PNRT - Pyrrhotite in the primary nickel rougher tail;

PT - Pyrrhotite in the pyrrhotite tail.

According to Legrand et al.'s [74, 103] research about the spectroscopy studies of pyrrhotite oxidation, the pyrrhotite spectrum (Fe *2p*, S *2p*, and O *1s*) display systematic changes resulting from surface oxidation, which can be used to analyze pyrrhotite oxidation states.

As shown in Figure 3-13, a strong, broad peak in the range of 710-714 eV, which is indicative of Ferric oxyhydroxide contribution, became increasingly dominated for pyrrhotite in the pyrrhotite tail (PT in Figure 3-13) and primary nickel rougher tail (PNRT in Figure 3-13) than that in the primary nickel rougher concentrate (PNRC in Figure 3-13). The dominant contribution of the Ferric oxyhydroxide in the pyrrhotite tail and primary nickel rougher tail than in the primary nickel rougher concentrate can also be seen in the gradual diminishing peak around 707 eV, which is indicative of Ferrous sulfide contribution. For the S *2p* signal, a peak near 168.7 eV, which indicates sulfate component, became increasingly apparent for pyrrhotite in the primary nickel rougher concentrate to pyrrhotite in primary nickel rougher tail, and to pyrrhotite in pyrrhotite tail. According to Legrand et al. [74, 103], changes in the Fe $2p_{3/2}$ and S *2p* signal are indicative of a more heavily oxidized overlayer on pyrrhotite surface in the tail (pyrrhotite tail and primary nickel rougher tail) than that in concentrate (primary nickel rougher concentrate).

Table 3-3. XPS Fe *2p*$_{3/2}$, S *2p*, and O *1s* peak parameters, proportions, and chemical states information for pyrrhotite in the 2017 plant survey.[4]

Peak	Binding Energy	FWHM	PNRC	PNRT	PT	Chemical State
	eV	eV	At%	At%	At%	
S *2p*	161.2	0.8	39	30	47	S^{2-}
S *2p*	161.7	0.8	14	9	13	S_2^{2-}
S *2p*	162.6	2.9	37	45	21	S_n^{2-}
S *2p*	166.7	1.3	0	4	1	$S_2O_3^{2-}$
S *2p*	168.3	1.2	11	12	19	SO_4^{2-}
O *1s*	531.3	1.7	41	50	49	OH^-
O *1s*	529.8	1.275	17	30	25	O^{2-}
O *1s*	532.0	1.7	15	7	10	SO_4^{2-}
O *1s*	532.5	1.7	16	12	14	$H_2O_{adsorbed}$
O *1s*	533.5	1.7	11	2	2	H_2O_{other}
Fe *2p*	706.3	1.1	23	14	7	Fe(II)-S
Fe *2p*	709.0	1.3	21	24	22	Fe(III)-S
Fe *2p*	710.4	1.6	56	62	71	Fe(III)-O

The proportions of surface species were determined via detailed quantitative analysis of XPS narrow region spectra and listed in Table 3-3. The XPS narrow region spectra were referenced with Gaussian-Lorentzian function combined with a Shirley background [74, 103].

[4] PNRC - Pyrrhotite in the primary nickel rougher concentrate;

PNRT - Pyrrhotite in the primary nickel rougher tail;

PT - Pyrrhotite in the pyrrhotite tail.

Table 3-4. Binding energies, FWHM, and area ratio for individual components of Fe(II)-S, Fe(III)-S, and Fe(III)-O multiplet structures.

Species	Peak	Binding Energy (eV)	FWHM (eV)	Area
Fe(II)-S	Multi. 1	706.2	1.0	1.00
	Multi. 2	707.2	1.2	3.80
	Multi. 3	708.1	1.0	1.32
	Multi. 4	713.0	2.6	1.61
Fe(III)-S	Multi. 1	709.0	1.3	1.00
	Multi. 2	710.1	1.3	0.66
	Multi. 3	711.1	1.3	0.35
	Multi. 4	712.0	1.3	0.15
Fe(III)-O	Multi. 1	710.4	1.6	1.00
	Multi. 2	711.4	1.6	0.95
	Multi. 3	712.6	1.6	0.59
	Multi. 4	713.9	1.6	0.28

According to Table 3-3, the oxidation degree of pyrrhotite in the primary nickel rougher concentrate, the primary nickel rougher tail, and the pyrrhotite tail can be reflected by the relative percentage of oxide species. The lower oxidation degree of pyrrhotite in the primary nickel rougher concentrate than that in the primary nickel rougher tail was shown by the difference in the proportion of Fe(III)-O and SO_4^{2-} (56% Fe(III)-O and 11% SO_4^{2-} for pyrrhotite in primary nickel rougher concentrate; 62% Fe(III)-O and 12% SO_4^{2-} of that in the primary nickel rougher tail). The high oxidation degree of pyrrhotite in the pyrrhotite tail was shown by the 71% of Fe(III)-O and 19% of SO_4^{2-}.

Due to the complexity of deconvolution of Fe $2p_{3/2}$ narrow spectra, detailed parameters used in this study for their deconvolution are listed in Table 3-4.

3.4.3. CV Studies

The oxidation of monoclinic and hexagonal pyrrhotite in the absence of collectors was investigated to relate the differential flotation performance of polymorphic pyrrhotite in sampled streams to the nature of pyrrhotite surface anterior to reactions with flotation reagents.

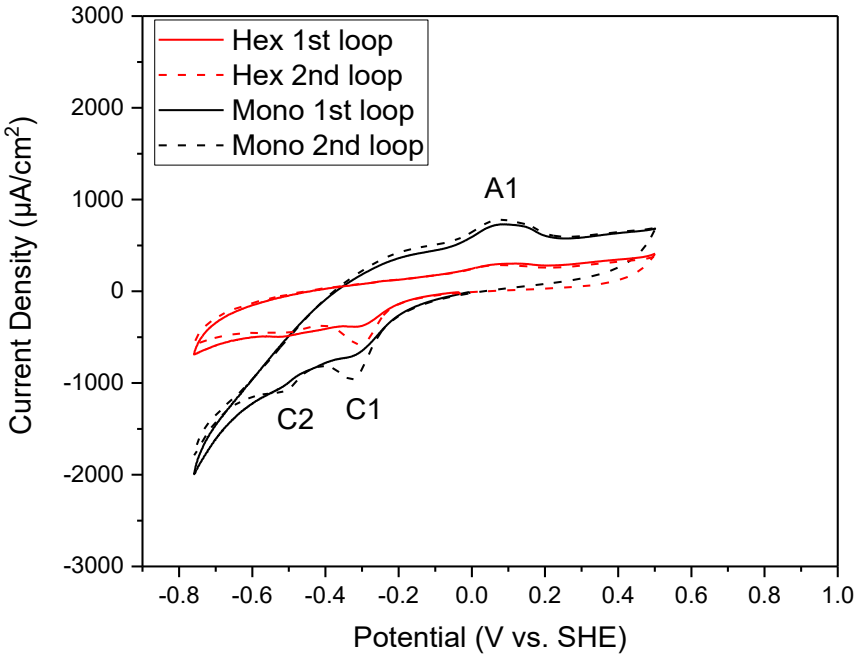

Figure 3-14. First two CV loops of rotating (2000 rpm) hexagonal and monoclinic pyrrhotite electrodes at pH 9.2 (0.05 M Borax, sweep rate 20 mV/s).

The CV of monoclinic and hexagonal pyrrhotite electrodes in an oxygen-deficient borate solution is shown in Figure 3-14. As elaborated before, the scan started from a negative-going direction to remove possible oxidation during polishing on a sand-paper. There was a small anodic current peak around 0.1 V (A1) on the return positive-going sweep, which was much more apparent for monoclinic pyrrhotite than for hexagonal pyrrhotite. Corresponding oxidation and reduction reactions that happened at peak A1, C1, and C2 are listed in Table 3-5.

Table 3-5. Summary of electrochemical anodic and cathodic reactions of pyrrhotite.

Peak (V vs. SHE)	Chemical Reactions	Reference
A1 (~0.1 V)	$Fe_{(1-x)}S+3yOH^-=Fe_{(1-(x+y))}S+yFe(OH)_3+3ye^-$	[38]
C1 (~-0.4 V)	$Fe(OH)_3+e^-+H^+=Fe(OH)_2+H_2O$	[38, 104]
	$S+2e^-+H^+=HS^-$	
C2 (~-0.55 V)	$S+Fe(OH)_2+2e^-=FeS+2OH^-$	[38, 104]

XPS data analysis showed that the development of the oxide layer is quite essential for pyrrhotite depression. Since pulp potentials of sampled slurries were ranges from 0.2 to 0.3 V vs. SHE, the formation rate of $Fe(OH)_3$, as shown by the peak height of A1 (Table 3-5), is one key part of pyrrhotite depression, i.e., the higher peak A1 height means faster formation rate of $Fe(OH)_3$, resulting in ready flotation depression of monoclinic pyrrhotite.

Ekmekçi et al.'s and Becker's [38, 98] studies also substantiated that the oxidation rate or the iron oxy-hydroxide layer formation rate, shown as the peak A1 height, is the reverse of pyrrhotite flotation recovery. Therefore, the higher A1 peak of monoclinic pyrrhotite than that of hexagonal pyrrhotite, which is indicative of the faster formation of an iron oxy-hydroxide layer on monoclinic pyrrhotite, showed that lower oxidation rate could be one important reason for better floatability of hexagonal pyrrhotite.

3.4.4. Discussions

Based on surface differences of pyrrhotite from the primary nickel rougher concentrate and the primary nickel rougher tail, surface oxidation differences and ions concentration differences (including Cu, Ni, Ca, and Mg) were critical parameters for pyrrhotite flotation and depression.

Among these parameters, polymorphic pyrrhotite difference in oxidation rate is one major reason for their flotation difference. During pyrrhotite oxidation, both ferric hydroxide and iron-deficient polysulfide species formed on their surfaces. The formation of initial oxidized product $Fe(OH)[S]^+$ is favorable for xanthate uptake. However, oxygen will speed up oxidation and promote $Fe(OH)_3$ precipitation [95]. As shown in CV studies, the higher oxidation rate of monoclinic pyrrhotite suggested that the formation of $Fe(OH)_3$ species on monoclinic pyrrhotite surfaces would be quicker than on hexagonal pyrrhotite. The formed hydrophilic $Fe(OH)_3$ layers render monoclinic pyrrhotite with a lower hydrophobicity. With a lower oxidation rate, hexagonal pyrrhotite gets a kinetic window (prior to the formation of a thick $Fe(OH)_3$ layer) for collector attachment. Meanwhile, the XPS analysis demonstrated that pyrrhotite oxidized more severely (with a higher percentage of Fe(III)-O and SO_4^{2-} species) reported into primary nickel rougher tail during flotation. Therefore, the high oxidation rate of monoclinic pyrrhotite is one important reason for the higher flotation recovery of hexagonal pyrrhotite in the nickel and copper concentrate than that of hexagonal pyrrhotite. To understand the differential oxidation rate of the hexagonal pyrrhotite and monoclinic pyrrhotite, their oxidation rate and electronic structures were further studied in Chapter 4.

Comparison of ions concentration on surfaces of the pyrrhotite in primary nickel rougher concentrate and the primary nickel rougher tail showed that Ni^{2+} and Cu^{2+} have activating effects on pyrrhotite flotation, Ca^{2+} and Mg^{2+} have depressing effects on pyrrhotite flotation. Ni^{2+} and Cu^{2+} have been claimed to be helpful for xanthate attachment onto pyrrhotite surfaces. During xanthate uptake onto pyrrhotite surfaces, xanthate electrostatic adsorption and then oxidation to form dixanthogen are two necessary steps. According to Multani and Waters [95], fresh pyrrhotite surfaces are negatively charged when pH is larger

than 3.5, preventing xanthate ions from adsorbing. Cu^{2+} and Ni^{2+} can change pyrrhotite zeta potential from negative to positive at acidic or slightly alkaline solutions (even at pH 10), facilitating xanthate physical adsorption onto pyrrhotite surfaces [62]. Acar and Somasundaran also showed that Cu^{2+} is more effective in reversing pyrrhotite surface charge than Ni^{2+} [62]. This was consistent with the phenomenon that the Cu/Fe ratio difference on pyrrhotite surfaces in the primary nickel rougher concentrate and the primary nickel rougher tails was much higher than that of Ni/Fe. As to the significant drop of hexagonal pyrrhotite flotation recovery in primary nickel rougher concentrate than that of monoclinic pyrrhotite in the 2017 plant survey, the lower Cu concentration is likely one important possibility. According to the summarization of previous research about activation studies on hexagonal pyrrhotite and monoclinic pyrrhotite by Multani and Waters, hexagonal pyrrhotite is better activated by Cu^{2+} than monoclinic pyrrhotite, which probably comes from different Fe^{2+}/Fe^{3+} ratio [95]. Lowered Cu^{2+} concentration in the nickel feed of the 2017 plant survey, as shown in the ICP studies (Figure 3-12), is likely to affect hexagonal pyrrhotite flotation recovery much stronger than monoclinic pyrrhotite. The significant Cu activation effects on the hexagonal pyrrhotite were further investigated and results were shown in Chapter 6. Even though Fe concentration differences are also observed in the nickel feed of these two plant surveys (Figure 3-12), its significance for pyrrhotite flotation is hardly corroborated by evidence from XPS or SIMS.

The higher ratio of Ca/Fe and Mg/Fe on pyrrhotite surfaces in the primary nickel rougher tail than that in the primary nickel rougher concentrate showed their depressing effects on pyrrhotite flotation. Ca^{2+}'s depressing effects on pyrrhotite have been widely studied due to lime's depressing effects on pyrrhotite. It is generally considered that calcium sulfate, calcium hydroxide, and calcium carbonate species are formed on iron sulfides [105]. Since

magnesium hydroxide is much less water-soluble than calcium hydroxide, Mg^{2+} ions were claimed as one important source for slime coating, especially for sea water flotation [106].

The enrichment of pyrrhotite in nickel feed could also be one important reason for the dropping of all major sulfide mineral flotation recovery in the 2017 primary nickel rougher circuit. As oxygen can be speedily consumed by pyrrhotite [98], high pyrrhotite grade in Ni feed for the 2017 plant survey could lead to low oxygen contents and low pulp potentials. Relative lower pulp potentials would result in overall lower recoveries of all principal sulfide minerals since moderate oxidation is necessary for the hydrophobic polysulfide layer formation and interactions with xanthate [92].

As discussed above, Cu ion concentration and oxidation conditions are two important factors for pyrrhotite flotation. The latter has two-fold effects: a low pulp potential would be beneficial for Pn/Po flotation separation at the cost of valuable mineral flotation recovery, while a high pulp potential would lower Pn/Po flotation selectivity. Meanwhile, controlling Cu ion concentration still offered us more opportunities for practical application due to the variation in the feeding ore. Generally, feeding ores for Strathcona Mill are composed of high Cu grade ore (Po grade is lower than 10%) and low Cu grade ore (Po grade around 20-30 %) [94]. Suppose the high Cu grade ore could be treated separately from that of low Cu grade ore. In that case, a low Po recovery could be expected since a high Pn/Po flotation selectivity can be achieved for the low Cu grade feeding ore (main distribution of Pyrrhotite) as a result of low copper activation effects.

3.5. Summary and Conclusions

XPS studies revealed that extensive oxidation is of key importance for pyrrhotite depression via demonstrating higher proportions of Fe(III)-O and SO_4^{2-} on pyrrhotite in the

tail than in the concentrate. In addition, the fact that the higher floatability of hexagonal pyrrhotite than that of monoclinic pyrrhotite was related to the naturally higher oxidation rate of monoclinic pyrrhotite in CV studies, which is indicative of the faster formation of the iron oxy-hydroxide layer.

By comparing the ratio of metal ions to iron on pyrrhotite surfaces, ToF-SIMS studies showed depressing effects of Ca and Mg on pyrrhotite flotation and activating effects of Cu and Ni on pyrrhotite flotation. Furthermore, pyrrhotite flotation recovery in the primary nickel rougher concentrate appeared to trend together with Cu concentration in Ni feed, which was more remarkable for hexagonal pyrrhotite.

Chapter 4. Unraveling Polymorphic Pyrrhotite Electrochemical Oxidation by Underlying Electronic Structures

Abstract:

Metal sulfides oxidation is a common yet poorly understood phenomenon that significantly affects surface properties. In this chapter, we studied the electrochemical oxidation of polymorphic pyrrhotites ($Fe_{1-x}S$) to gain insights into the relationship between their electrochemical oxidation rate and electronic structures. The surface composition of oxidized pyrrhotites, as shown by Time-of-Flight Secondary Ion Mass Spectrometry (ToF-SIMS) and X-ray Photoelectron Spectroscopy (XPS), suggested that one critical step for pyrrhotite oxidation is the outward diffusion of metal cations to form polysulfide and oxides. This diffusion process involves the rupture of Fe-S bonds, hence depends on the Fe-S bond strength. According to the ToF-SIMS, the Fe-S bond strength in the defective layer (> 100 nm), the layer right underneath the polysulfide layer (~10 to 20 nm), got modified by the incorporation of oxygen atoms, which mainly existed in the form of OH^- and H_2O. It was found that oxygen anions are much more abundant in the defective layer of monoclinic pyrrhotite (Fe_7S_8) than that of hexagonal pyrrhotite (Fe_9S_{10}), resulting in a much weaker Fe-S bond with the former than the latter. The oxygen abundance difference can be explained by their electronic structures. Density functional theory (DFT) calculation showed that monoclinic pyrrhotite (Fe_7S_8) gets a higher Fe *3d* and S *3p* band center than hexagonal pyrrhotite (Fe_9S_{10}). Therefore, monoclinic pyrrhotite could incorporate oxygen atoms easier than hexagonal pyrrhotite. This presented a clear relation between polymorphic pyrrhotite electronic structures and their electrochemical oxidation rate. It also fundamentally explained why the sulfides with slight bulk metal-sulfur bond strength difference could demonstrate a significant oxidation rate difference.

4.1. Introduction

As major sources of nonferrous base metals, sulfide minerals are usually recovered and separated from other gangue minerals via flotation based on surface hydrophobicity [107], which is significantly affected by the oxidation level of the sulfide minerals. The control of the redox environment to separate sulfide minerals requires a fundamental understanding of the critical parameters controlling sulfide oxidation. One crucial parameter is sulfide electronic structure, but a clear relationship between sulfide electronic structure and sulfide oxidation is still developing [108]. Meanwhile, a clear relationship has been established between sulfide electronic structures and oxygen reduction reactions (ORR) on sulfide mineral surfaces. This correlation between sulfide electronic structures and surface ORR was shown by linear fits of the S 3p band centers (relative to Fermi level) and the rest potentials of metal sulfides in xanthate solutions [109-111]. This linear fitting offered deep insights into oxygen reduction reactions (ORR) on the vast majority of sulfide mineral surfaces. Sulfide oxidations, which are usually caused by oxygen reductions on their surfaces, are most likely affected by their electronic structures. However, the relation between sulfide oxidation and their electronic structures is still in development due to an insufficient understanding of the steps involved in the sulfide oxidation process. In this study, pyrrhotite, $Fe_{(1-x)}S$ ($0<x\leq0.2$), a major non-stoichiometric iron sulfide gangue mineral in Ni-Cu ores [3] and a major contributor to acid mine drainage [112], was studied to reveal the relationship between its electronic structures and oxidation. For a detailed introduction about pyrrhotite, please check Paragraph 2 in Chapter 3 Section 3.1. Note that vacancies inside 4C-monoclinic pyrrhotite are generally agreed to be full vacancies; however, recent studies have argued that those inside 5C-hexagonal pyrrhotite are partial vacancies [2, 113, 114].

Even though polymorphic pyrrhotites are only slightly different in their crystal structures and the number of vacancies, their floatabilities are distinctly different from each other due to their different oxidation rates. Generally, hexagonal pyrrhotite floats much better than monoclinic pyrrhotite since hexagonal pyrrhotite can oxidize at a much lower rate [3, 18, 38, 115]. This oxidation rate difference has been attributed to the different amounts of vacancies. However, their difference in vacancies is quite slight and unlikely to be the main reason for their vast oxidation rate difference. Another possible important parameter for the differential oxidation of pyrrhotite polymorphs is their different electronic structures, but further research is needed to understand the oxidation process better.

Conventionally, sulfide oxidation is mainly concerned with polysulfide and oxide species formed in the superficial oxidation layer, usually tens of nanometers thick [116]. Underneath this oxidation layer, there is a layer called the defective layer [117, 118]. The defective layer was so named because of its near-stoichiometric and highly stable nature [118], which means that metal cations can diffuse out from this layer without forming disulfide or polysulfide [118]. Recent research has shown that this defective layer, which can be a hundred nanometers thick, significantly affects metal sulfide chemical reactivity and physical properties [117, 118]. However, the relation between the oxidation rate-determining step (i.e., the metal-releasing rate proposed by Milkhlin et al. [118]) and the properties of the defective layer is still unclear due to the limited understanding of this layer.

This chapter aims to gain insights into the relationship between polymorphic pyrrhotites' oxidation rates and their electronic structures via investigating their oxidized surfaces, particularly the defective layer. The results of X-ray photoelectron spectroscopy (XPS) and time-of-flight secondary ion mass spectrometry (ToF-SIMS) investigations demonstrated

the gradual oxidation of pyrrhotite polymorphs and the relation between their oxidation rate and the properties of the defective layer. Using spectroscopic and DFT simulation results, we present the relation between polymorphic pyrrhotites electronic structures and their oxidation rate. We believe the same systematic approach can be applied to other sulfide minerals to develop a more applicable model for the oxidation of all sulfide minerals.

4.2. Methods

4.2.1. Cyclic Voltammetry (CV) Studies

Electrode Preparation

Magnetic monoclinic pyrrhotite and non-magnetic hexagonal pyrrhotite electrodes were prepared according to the procedure in Section 3.3.4. Surface Characterization. The well-prepared electrodes were then polished, and their purity was confirmed by scanning electron microscopy (SEM) with backscattered electron imaging (BSE) and energy dispersive X-ray spectrometry (EDX) (See Appendix A.5 Pyrrhotite Electrode Purity for details). Note that electrodes used for ToF-SIMS and XPS tests were cured into one bigger epoxy piece to have the same planar surface for a better comparison.

Cyclic Voltammetry (CV) Test Procedures

Before every CV test, electrode surfaces were cleaned by gentle wet-polishing on 600 grit followed by 1200 grit sandpaper for 2 minutes on each sandpaper and subsequent rinsing with Milli-Q water. Electrolyte solutions were purged with high purity nitrogen for 15 minutes before each test. Potential sweeps started from the open circuit potential towards the negative potential at a scan rate of 20 mV/s. Current variations were reported as current density. Note that the electrochemically active surface area was calculated by taking a picture of the electrode surface and count the active area with ImageJ. Potentials were

recorded relative to the standard calomel electrode (SCE) and reported against the standard hydrogen electrode (SHE) in this chapter. The platinum mesh was used as the counter electrode, and all CV tests were conducted with the potentiostat PGSTAT302N (Metrohm Autolab, Utrecht, Netherlands). Buffer solutions were composed of the following: pH 7.6 (0.17 M $H_2B_4O_7$ + 0.0075 M $Na_2B_4O_7$ + 0.047 M H_2SO_4), pH 9.2 (0.05 M $Na_2B_4O_7$), and pH 11.0 (0.0237 M Na_2CO_3 + 0.0025 M $NaHCO_3$).

4.2.2. ToF-SIMS Depth Profiles

Wet-polished (two minutes on a 1200 grit sandpaper) pyrrhotite electrodes were oxidized under an applied potential of 0.4 V for 1 min in N_2-purged (15 min) pH 9.2 borate buffer solution. After conditioning, the specimens were transferred into a de-oxygenated pH 9.2 Milli-Q water solution (adjusted by NaOH) to wash off borate, followed by a swift transfer into a vacuum chamber to dry. After drying for 24 hours, the sample was transported into the high vacuum ToF-SIMS testing chamber (5×10^{-9} mbar).

To determine the species distribution on different oxidized layers, we conducted a ToF-SIMS depth profile with a ToF-SIMS IV (IONTOF GmbH, Münster, Germany) at the Nanofabrication and Characterization Facility (nanoFAB). Sputtering was done with Cs^+ ions at 1 kV and around 10 nA over an area of 200 × 200 μm^2, under pressure lower than 5×10^{-9} mbar. Bi^+ ions, operated at 25 kV, were used as the analytical source. By alternating Bi^+ and Cs^+ ions, depth profiles of 40 × 40 μm^2 in the centers of craters were acquired. Note that the sputtering rate is about 1.3 Å/s when applied onto a Si surface (See Appendix A.4.2. Sputtering Rate Estimation for details).

4.2.3. XPS Tests

The same electrode preparation procedures for the ToF-SIMS depth profile tests in this Chapter were used here. The XPS analysis was performed with an AXIS 165 (Kratos

Analytical Ltd, Manchester, UK) with a monochromatized Al Kα source (hν = 1486.6 eV) in the nanoFAB. Sputtering was done with Ar^+ at 4 kV and around 10 mA, under the pressure of 2×10^{-8} Torr for 1 min. Spectra were referenced to the binding energy of C 1*s* (284.8 eV) to ensure that the binding energy shift due to charging was calibrated.

4.2.4. Density Functional Theory (DFT) Simulation

Crystal Structure and Symmetry

In this study, the low-temperature crystal structure derived by Powell et al. at 11 K [119] was used as the reference structure 4C-pyrrhotite. As described before, the crystal structure of 5C-pyrrhotite is associated with some uncertainty [2, 4, 113, 114, 120, 121]. Here, we used the structure proposed by Vaughan et al. [6]. Mohammad Khalkhali did DFT simulation work.

Simulation Details

In this study, periodic DFT calculations were carried out using the plane-wave pseudopotential method as implemented in the CASTEP module [122, 123] within the Materials Studio software package (Version 8, Accelrys, San Diego, CA, USA). The generalized gradient approximation of the Perdew–Burke–Ernzerhof (PBE) functional form [124] augmented with a rotationally-invariant Hubbard-like U term was used to account for the strong electron correlation on the Fe *3d* orbitals. This "DFT + U" method [125, 126] has successfully reproduced experimental lattice constants of other iron sulfides (troilite and pyrite) [127-130]. Ultrasoft pseudopotentials were used to model the core-electron interaction, treating explicitly the *4s*, *3d,* and *3p* electrons of Fe, and the *3s* and *3p* of S. A plane wave energy cut-off of 350 eV and Monkhorst-Pack grid with k point separation of 0.04 $Å^{-1}$ were chosen for both structures after checking the energy convergence carefully in a series of single point energy calculations. The presence of iron

in the component necessitated spin-polarization calculations. Spin configurations that are ferrimagnetic and antiferromagnetic along the C axis revealed the lowest energy configurations in 4C- and 5C-pyrrhotite, respectively. These spin configurations are similar to atomic magnetic moments proposed in previous experimental studies [5, 119]. The find the optimal U value in the Hubbard-corrected DFT scheme, the unit cell volume of both pyrrhotite polymorphs obtained from a series of geometry optimizations was compared with the experimentally reported ones. The value of U = 1.8 eV was taken as it gave the best agreement for both polymorphs (Please refer to Figure A-1 for more details).

4.3. Results and Discussion

4.3.1. CV Studies

Results from CV experiments with monoclinic and hexagonal pyrrhotite at pH 7.6, pH 9.2, and pH 11.0 are shown in Figure 4-1. During the experiments, a strong anodic peak was observed if the upper switching potential was too high (>0.5 V at pH 7.6 and pH 9.2 or >0.4 V at pH 11.0). A similar phenomenon was observed by Buswell and Nicol [104]. As the pulp potential in traditional Ni-Cu flotation is lower than 0.4 V [23, 80], pyrrhotite oxidation under 0.4 V was studied.

Since pyrrhotite oxidizes very quickly (within several seconds when exposed to air), there is a weak anodic peak (which varied from -0.25 V at pH 7.6 to -0.45 V at pH 11.0) shown on the first sweep in a negative direction from the open circuit potential even though the surface was freshly polished before each test. On the following positive sweep, one anodic peak A_1 appeared around 0.1 V with a slight position difference for various pH. There remain some controversies about the oxidation reactions that occur at peak A_1. Details of their assumptions are listed in Table A-3. Under all test pH conditions, the peak A_1 of

monoclinic pyrrhotite was higher than that of hexagonal pyrrhotite, suggesting a higher oxidation rate of monoclinic pyrrhotite.

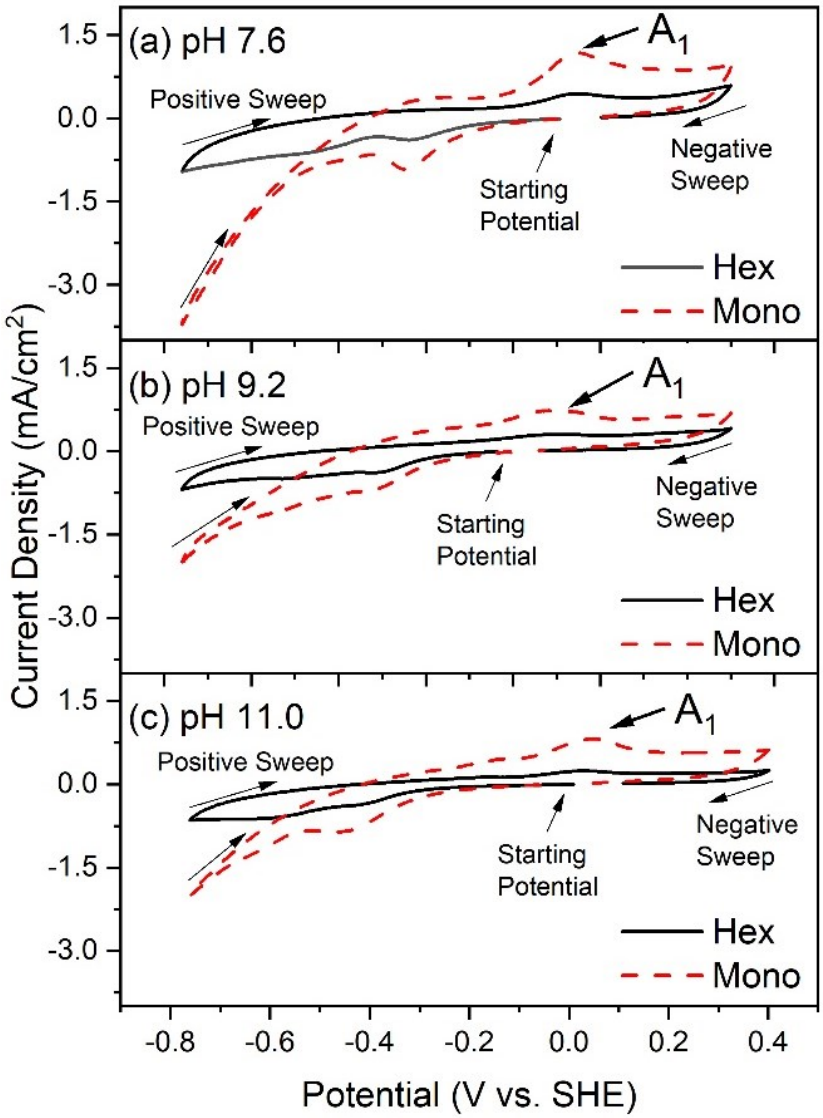

Figure 4-1. Comparison of the cyclic voltammograms of rotating hexagonal and monoclinic pyrrhotite electrodes at pH 7.6 (a), pH 9.2 (b) (same as Figure 3-14), and pH 11.0 (c) buffer solutions.

4.3.2. XPS Results

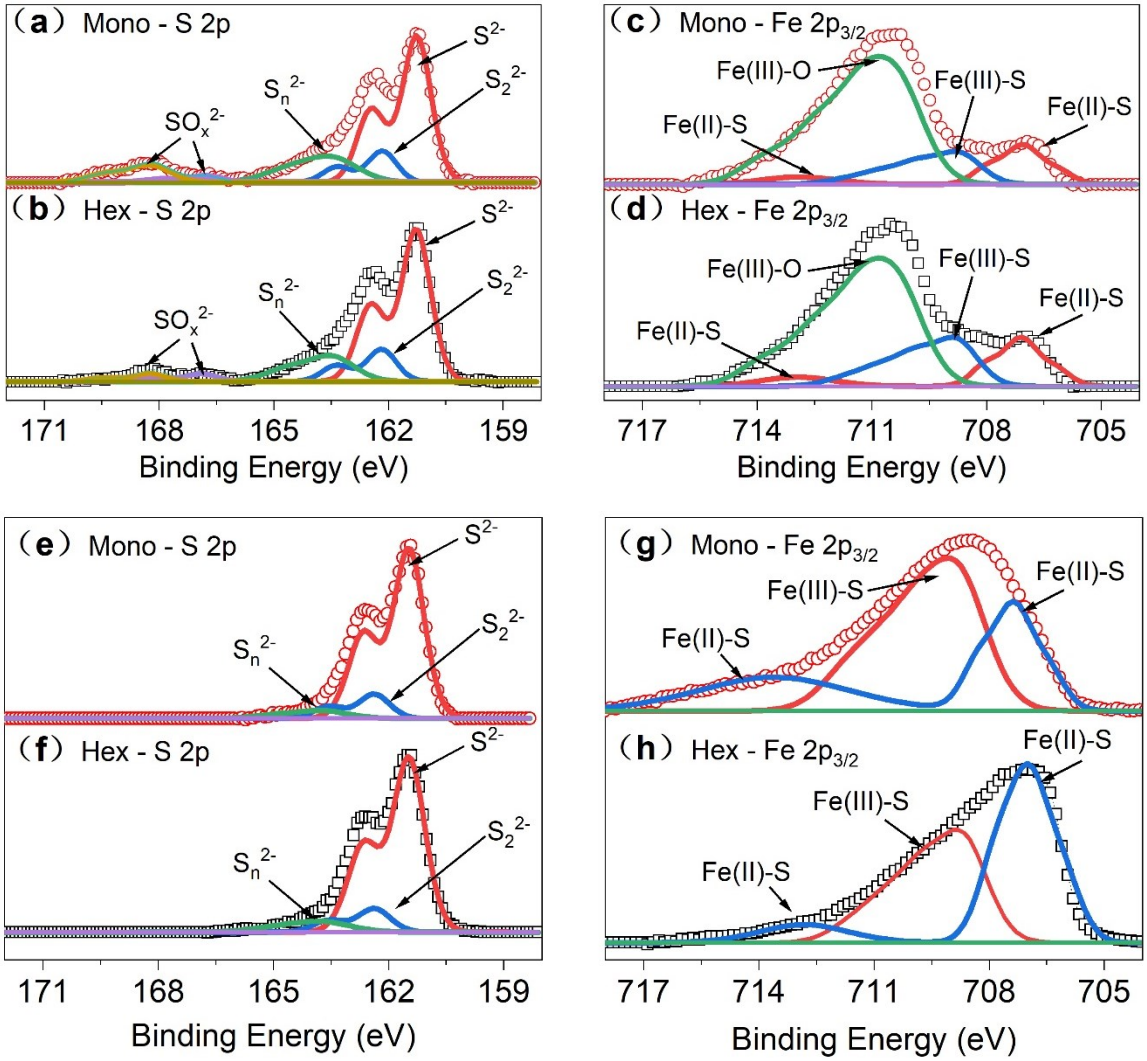

Figure 4-2. Overlays of S *2p* (a, b) and Fe *2p*$_{3/2}$ (c, d) of pyrrhotite oxidized at 0.4 V for 1 min; Overlays of S *2p* (e, f) and Fe *2p*$_{3/2}$ (g, h) of pyrrhotite oxidized at 0.4 V for 1 min and cleaned with Ar^+ sputtering for 1 min.

Oxidized pyrrhotite surfaces, as well as the layers beneath, were studied via XPS (Figure 4-2). For interpreting XPS results, the peaks from narrow region scans were analyzed using the Shirley background and Gaussian-Lorentzian (60% Gaussian – 40% Lorentzian) peak model. Binding energies and other parameters were mainly referenced from Pratt and Nesbitt [35], Legrand [116, 131], Knipe et al. [133], Richardson and Vaughan [66],

Scofield [135], Mikhlin and Tomashevich [136], Biesinger et al. [132], and Moulder et al. [134] (See Appendix A.2 XPS Analysis Details for details). Note that the multiplet splitting happens on iron in pyrrhotite and only the envelopes are listed in Figure 4-2, the individual peaks are listed in Figure A-4. The narrow spectra fitting peak parameters, proportions, and corresponding chemical states for pyrrhotite oxidized surfaces and sublayers are listed in Table 4-1.

Table 4-1. Peak parameters, proportions, and corresponding chemical state information of XPS Fe $2p_{3/2}$ and S $2p$.[5]

Peak	Binding Energy (eV)	FWHM (eV)	M 0.4 V	M(C) 0.4 V	H 0.4 V	H(C) 0.4 V	Chemistry
Fe $2p_{3/2}$	706.1	0.9	15.32	43.43	16.63	56.01	Fe(II)-S
Fe $2p_{3/2}$	708.9	1.3	15.22	56.55	20.43	43.99	Fe(III)-S
Fe $2p_{3/2}$	710.4	1.6	69.46	0	62.93	0	Fe(III)-O
S $2p$	161.3	0.9	58.00	82.45	63.52	81.32	S^{2-}
S $2p$	162.2	0.9	12.54	11.85	13.51	11.01	S_2^{2-}
S $2p$	163.5	1.6	17.02	5.7	15.79	7.66	S_n^{2-}
S $2p$	166.8	1.0	2.88	0	3.52	0	$S_2O_3^{2-}$
S $2p$	168.2	1.3	9.57	0	3.65	0	SO_4^{2-}

[5] M 0.4 V- monoclinic pyrrhotite which was oxidized at 0.4 V for 1 min;

M(C) 0.4 V- monoclinic pyrrhotite which was oxidized at 0.4 V for 1 min and then cleaned with Ar^+ sputtering in the XPS test chamber;

H 0.4 V- hexagonal pyrrhotite which was oxidized at 0.4 V for 1 min;

H(C) 0.4 V- hexagonal pyrrhotite which was oxidized at 0.4 V for 1 min and then cleaned with Ar^+ sputtering in the XPS test chamber.

As shown in Table 4-1, more abundant ferric oxide species (monoclinic, 69.46%; hexagonal, 62.93%) and sulfoxide species, including both $S_2O_3^{2-}$ and SO_4^{2-} (monoclinic, 12.45%; hexagonal, 7.17%), formed on monoclinic pyrrhotite surfaces, indicating more oxidation than that of hexagonal pyrrhotite. Meanwhile, a similar amount of polysulfide species (S_n^{2-}, n≥2) (monoclinic, 29.56 %; hexagonal, 29.30%) was observed.

To better understand pyrrhotite oxidation, the oxidized pyrrhotite surfaces were sputtered with Ar^+ for one minute. After Ar^+ sputtering, the signal of Fe(III)-O, SO_4^{2-}, and $S_2O_3^{2-}$ disappeared, indicating that these oxidized species mainly existed in the very superficial layer (Figure 4-2 and Table 4-1). Also, the significant decrease of the polysulfide species (S_n^{2-}) (from 17.02% to 5.7% on monoclinic pyrrhotite and from 15.79% to 7.66% on hexagonal pyrrhotite) after Ar^+ sputtering showed that polysulfide species are important components of the removed superficial layers.

4.3.3. ToF-SIMS Depth Profile

To better understand the pyrrhotite oxidation process, oxidized pyrrhotite surfaces were analyzed with ToF-SIMS. During ToF-SIMS analysis, oxidized pyrrhotite surfaces were sputtered off layer by layer and the ejected species were determined by their mass over charge ratio. According to species variation (Figure 4-3) with sputtering time, the oxidized pyrrhotite surface can be roughly divided into three layers (Figure 4-5): I Oxide layer, II Polysulfide layer, and III Defective layer (the layer with abundant sulfide, slight amount of oxide, and no disulfide or polysulfide). Note that since no suitable materials were found for calibration the sputtering rate, we could only estimate the depth of these layers based on the sputtering rate when applied onto the Si surface, which is about 1.3 Å/s. Based on that, the sputtering rate on Pyrrhotite was estimated to be about 1.6 Å/s. Therefore, the layer I, the layer II, and layer III thickness are around 10 nm, 20 nm, and 200 nm, respectively (See Appendix A.4.2 Sputtering Rate Estimation).

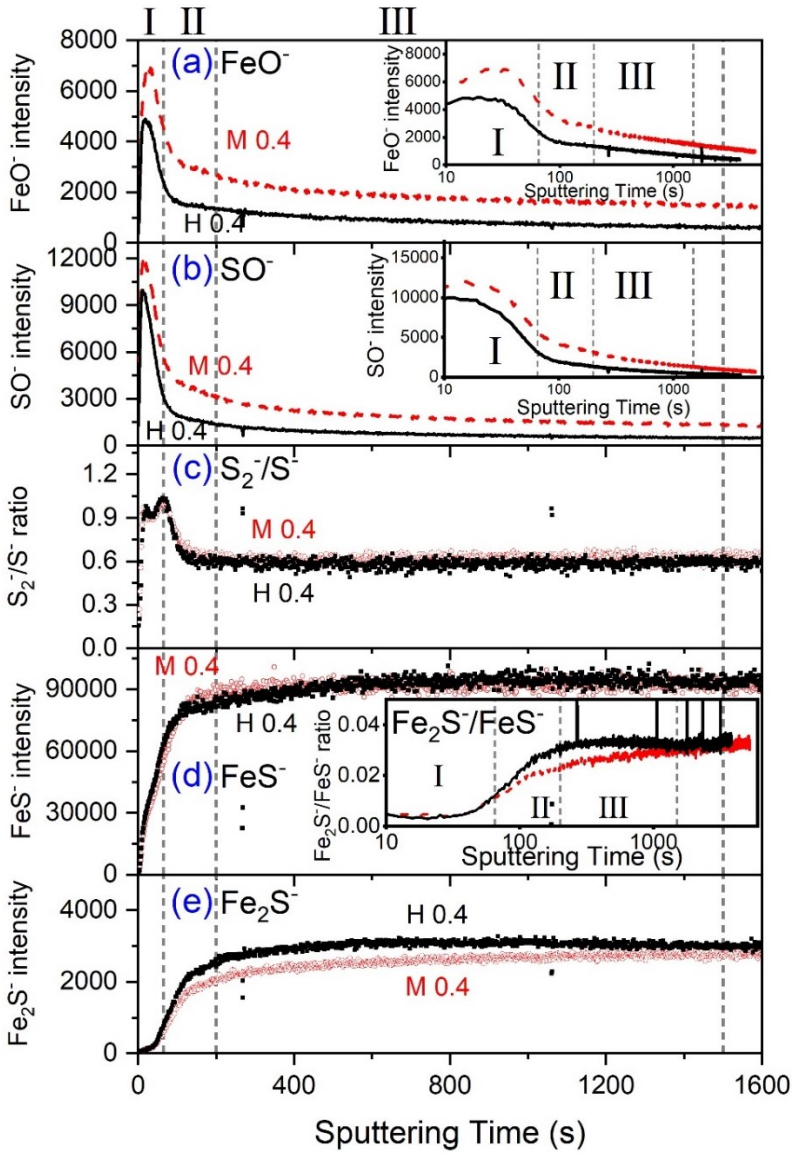

Figure 4-3. Variation of FeO^- intensity (a), SO^- intensity (b), S_2^-/S^- (c), FeS^- intensity (d), and Fe_2S^- intensity € as a function of linearly displayed sputtering time for hexagonal pyrrhotite (black squares) and monoclinic pyrrhotite (red circles) oxidized at 0.4 V vs. SHE for 1 min in pH 9.2 borate buffer solutions. Variation of FeO^- intensity (inset figure, a), SO^- intensity (inset figure, b), and Fe_2S^-/FeS^- ratio (inset figure, d) as a function of logarithmically displayed sputtering time for hexagonal pyrrhotite (black squares) and monoclinic pyrrhotite (red circles) oxidized at 0.4 V for 1 min in pH 9.2 borate buffer solutions. (Note that the intensity refers to the Poisson corrected counts)

The name of layer I—the oxide layer—comes from that the SO^- and FeO^- species were abundant during the initial sputtering time and decreased significantly with further sputtering (Figure 4-3a and Figure 4-3b). Their variation indicated that iron oxide and sulfoxide species mainly existed on the very superficial layer, which is consistent with XPS results (Figure 4-2 and Table 4-1).

The name of layer II—the polysulfide layer—comes from the variation of S_2^-/S^-. Smart et al. showed that S_n/S ($n \geq 2$) is a good indicator for disulfide and polysulfide species based on comparing ToF-SIMS spectra and XPS spectra [137]. The high ratio of S_n/S is therefore used to represent the polysulfide species. Figure 4-3c demonstrates that S_2^-/S^- started to increase from the II/III layer interface until the I/II layer interface, followed by a sudden slight decrease of S_2^-/S^- and simultaneous increase of FeO^- and SO^- (Figure 4-3a and Figure 4-3b). The simultaneous decrease of S_2^-/S^- (Figure 4-3c) and the increase of FeO^- and SO^- (Figure 4-3a and Figure 4-3b) suggests the surficial oxides are formed from the oxidation iron polysulfide. Also, the high ratio of S_2^-/S^- in layer I suggested that polysulfide species also existed in layer I.

The name of layer III—the defective layer—is referenced from Milkhlin et al.'s research [118]. Milkhlin et al. claimed that metal cations could diffuse out from the defective layer without forming disulfide species [118]. In our study, the stability of this defective layer was also supported by the constant FeS^- (Figure 4-3d) and S_2^-/S^- value (Figure 4-3c) in layer III.

Species variation in layer III also demonstrated the variation of the Fe-S bond strength. The binding energy is an important parameter that can affect the number of ejected species

during sputtering. For example, the emission of Fe_2S^- could be interpreted as an iron atom combining with the main species (FeS^-), which depends on the Fe-S bond strength (for more details, please refer to Appendix A.4.1 Data Interpretation). As shown in Figure 4-3e, the Fe_2S^- intensity of monoclinic pyrrhotite was lower than that of hexagonal pyrrhotite at depths below layer II. The higher Fe_2S^- intensity inside hexagonal pyrrhotite reflected its stronger Fe-S bond [137-139]. This Fe-S bond strength variation is clearer with the variation of Fe_2S^-/FeS^- ratio (see inset, Figure 4-3d). The Fe_2S^-/FeS^- ratio (see inset, Figure 4-3d) inside monoclinic pyrrhotite dropped almost linearly with logarithmic time in layer III while that of hexagonal pyrrhotite is stable in layer III. With a much lower Fe_2S^-/FeS^- ratio or weaker Fe-S bonds near the layer II/III interface, monoclinic pyrrhotite could form polysulfide species at a relatively higher rate during oxidation than hexagonal pyrrhotite since Fe-S bond breaking is an important step during disulfide and polysulfide formation.

Oxide species (Figure 4-3a), including iron oxide and sulfoxide, are much more abundant inside layer III of monoclinic pyrrhotite than those in the hexagonal pyrrhotite. Also, the FeO^- and SO^- dropped almost linearly with the logarithm of sputtering time (see inset, Figure 4-3a and Figure 4-3b), suggesting that oxides in layer III did not originally exist in pyrrhotite but come from inward diffusion of oxygen anions. Importantly, the FeO^- and SO^- in layer III are more abundant inside monoclinic pyrrhotite than in hexagonal pyrrhotite, which could be one important reason for the much weaker Fe-S bond in layer III of monoclinic pyrrhotite.

4.3.4. Simulation Results

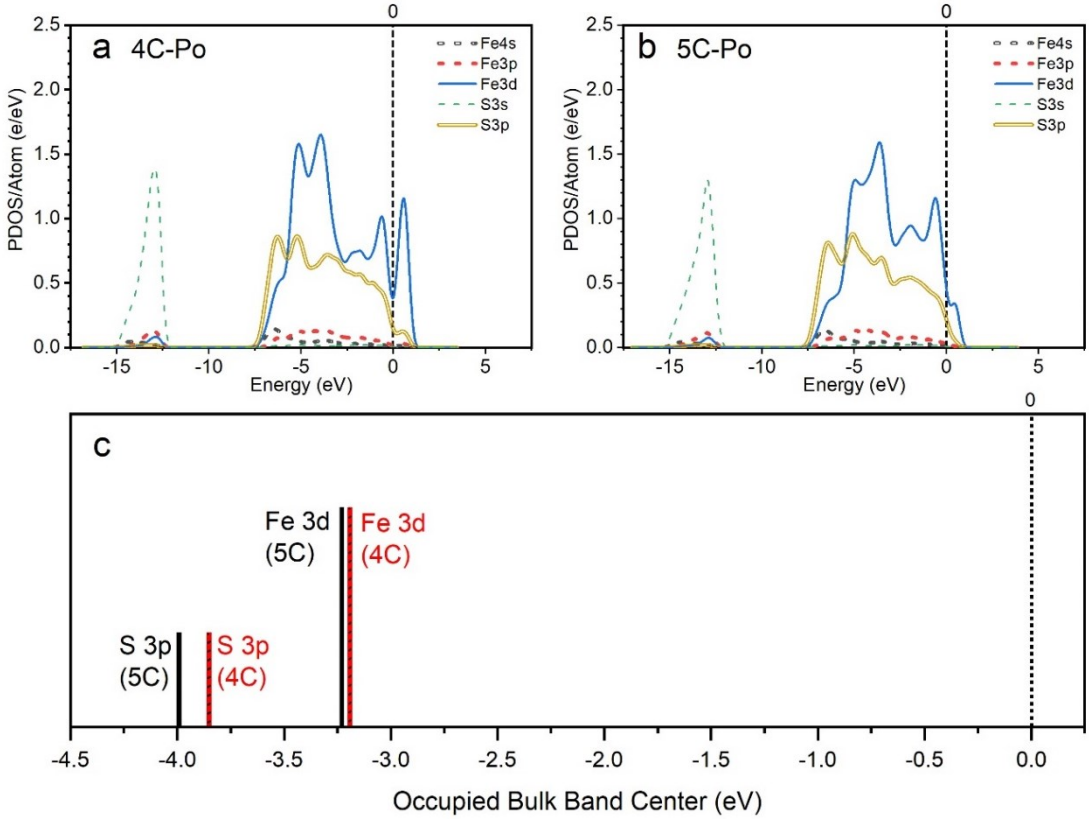

Figure 4-4. Partial density of states of 4C-monoclinic pyrrhotite (a) and 5C-hexagonal pyrrhotite (b); (c) bulk S *3p* and Fe *3d* band centers of 4C-monoclinic pyrrhotite and 5C-hexagonal pyrrhotite (note that their height is only for identifying Fe *3d* band center from S *3p* band center and contains no physical meaning here).[6]

Figure 4-4a and Figure 4-4b show the partial density of states (PDOS) calculated for optimized 4C- and 5C-pyrrhotite unit cells, respectively. PDOS diagrams are normalized according to the number of the corresponding atoms (Fe or S) in the unit cell and the energy set to 0 eV at the Femi level (E_F). PDOS diagrams (Figure 4-4a and Figure 4-4b) and the band structures (Figure A-2a and Figure A-2b) show that both pyrrhotite structures are

[6] This simulation work was carried out by Mohammad Khalkhali.

conductors, which means that electron transfer can readily happen when needed for oxidation.

For metallic components, the energy of the metal d band center can reflect its reactivity: the higher the metal d band center, the lower-filling of the antibonding states and hence the stronger metal-oxide bond [140, 141]. For sulfide minerals, Tao et al. found a general bulk descriptor, S *3p*, and claimed that metal sulfides with a higher bulk S *3p* band center could compete more strongly for the oxygen reduction reaction intermediates with the metallic cations [109].

As shown in Figure 4-4c, both Fe *3d* and S *3p* band centers of the 4C-monoclinic pyrrhotite are higher than those for 5C-hexagonal pyrrhotite. This suggests that both Fe and S inside monoclinic pyrrhotite can bond with oxygen anions more easily than those in hexagonal pyrrhotite.

The bond length calculated for bulk pyrrhotite polymorphs confirms that the average Fe-S bond length is slightly shorter in 5C-hexagonal pyrrhotite, suggesting that the Fe-S bonds are slightly stronger in 5C-hexagonal pyrrhotite compared to 4C-monoclinic pyrrhotite (Figure A-3). This bond strength difference is consistent with the slightly higher Fe_2S^-/FeS^- value of 5C-hexagonal pyrrhotite than that of 4C-monoclinic pyrrhotite in the deepest layers tested in the ToF-SIMS study (see inset, Figure 4-3d).

4.3.5. Discussion

XPS results showed that major oxidized products on pyrrhotite surfaces are Fe(III)-S, polysulfide, iron oxides, and sulfoxides, and variation of the oxidized layers was

characterized by ToF-SIMS. Depth profiles of oxidation products on pyrrhotite surfaces demonstrated two major steps for pyrrhotite oxidation: the first is from iron monosulfide (layer III) to iron polysulfide (layer II), and the second is from iron polysulfide (layer II) to oxides (layer I). XPS results confirmed that oxides, including both iron oxides and sulfoxides, mainly exist in the very superficial layers of oxidized pyrrhotite, while polysulfides still can be detected even after the superficial layer was removed (Figure 4-2). Note that even though oxides in layer III and deeper layers are not shown in XPS spectra (Figure 4-2e, Figure 4-2f, Figure 4-2g, and Figure 4-2h), they are still possible products in this layer. This is supported by Becker and Hochella's research that when S bonded with one or two O, the binding energy of S would be 162.0 eV and 163.3 eV, respectively [142].

Since polysulfide species are both major oxidized products and important intermediate products for forming oxides, faster oxidation of monoclinic pyrrhotite means the faster formation of polysulfide species. Polysulfide formation involves electron transfer, the oxidation of S from S^{2-} to high valence sulfur (S_2^{2-} or S_n^{2-}), and the breaking of Fe-S bonds[117, 136, 143, 144]. Electron transfer can readily happen when needed for oxidation since both pyrrhotites are conductors (Figure 4-4a and Figure 4-4b). As for sulfur oxidation, the higher S *3p* band center (relative to Fermi level) of monoclinic pyrrhotite (Figure 4-4c) suggested that its S could be more readily oxidized than that of hexagonal pyrrhotite. The breaking of Fe-S bonds would depend on the Fe-S bond strength. The slightly longer average Fe-S bond distance of 4C-monoclinic pyrrhotite showed that the Fe-S bonds inside monoclinic pyrrhotite are slightly weaker than that in 5C-hexagonal pyrrhotite (Figure A-3). Meanwhile, the ToF-SIMS depth profile suggested that the Fe-S bond strength (the Fe_2S^- /FeS^- ratio, see inset, Figure 4-3d) in monoclinic pyrrhotite becomes increasingly weaker than hexagonal pyrrhotite across layer III as it approaches layer II. Therefore, both the higher S *3p* band center and the weaker Fe-S bonds inside monoclinic pyrrhotite suggest

that polysulfide could form more easily in monoclinic pyrrhotite than in hexagonal pyrrhotite.

Admittedly, mechanisms of the Fe-S bond strength variation in layer III still cannot be accurately determined. However, ToF-SIMS results suggested that the Fe-S bond strength variation in layer III related to the oxygen anions diffused into layer III. The FeO^- and SO^- in layer III of the monoclinic pyrrhotite is more abundant than those in hexagonal pyrrhotite (Figure 4-3a and Figure 4-3b); the abundance of oxides in monoclinic pyrrhotite is likely one main reason for its much lower Fe_2S^-/FeS^- in layer III. Importantly, the formation of Fe-O or S-O would decrease the Fe-S bond strength due to the higher electronegativity of O than S and Fe. The more abundant oxides inside monoclinic pyrrhotite layer III and deeper layers (Figure 4-3a and Figure 4-3b) could be further explained by their electronic structures. The higher Fe *3d* and S *3p* band centers of monoclinic pyrrhotite (Figure 4-4c) suggested that its Fe and S could get oxidized more easily and form an under-layer with more oxygen anions (Figure 4-5).

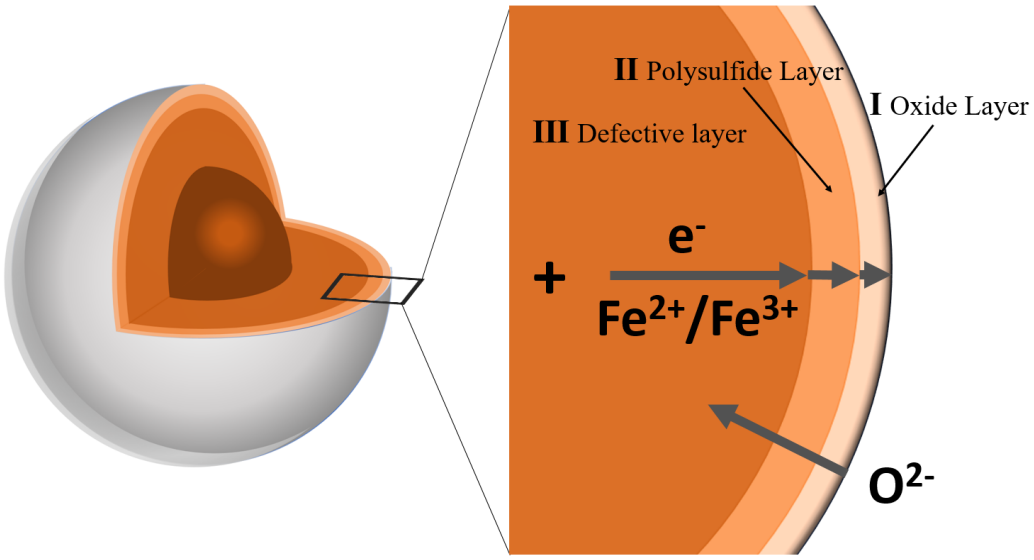

Figure 4-5. Schematic diagram of the pyrrhotite oxidation process.

The faster formation of polysulfide inside monoclinic pyrrhotite also means faster iron outward-diffusion, which helps to form iron oxides on the superficial layer. As the intermediate products for forming sulfoxides, more abundant polysulfide species inside monoclinic pyrrhotite also produced more sulfoxides, as shown in Table 4-1 (12.45% SO_x^{2-}, monoclinic pyrrhotite; 7.17% SO_x^{2-}, hexagonal pyrrhotite). As both iron oxides and sulfoxides are harmful for xanthate adsorption, the lower floatability of monoclinic pyrrhotite in alkaline solutions is expected [38, 104, 145].

4.4. Conclusions

For pyrrhotite oxidation in the alkaline environment, pyrrhotite oxidized from iron monosulfide to iron polysulfide and then to oxides. Since polysulfide species are both major oxidized products and important intermediate products in the formation of oxides, faster oxidation of monoclinic pyrrhotite also means faster polysulfide formation. As the breaking of Fe-S bonds is involved in forming polysulfide, the increasingly weaker Fe-S bond strength of monoclinic pyrrhotite than hexagonal pyrrhotite throughout layer III explained the higher oxidation rate of monoclinic pyrrhotite quite well. This much weaker Fe-S bond inside monoclinic pyrrhotite is likely related to more abundant oxide species diffused in layer III and in deeper layers. More importantly, the abundance of oxides in layer III of the monoclinic pyrrhotite can be further linked to the higher reactivity of iron and sulfur compared to hexagonal pyrrhotite. The higher Fe 3d band center and S 3p band center of monoclinic pyrrhotite suggested that its iron and sulfur can be oxidized more easily and form a layer III or deeper layers with more oxygen anions. With more abundant polysulfide species, monoclinic pyrrhotite would form an oxide layer with more abundant iron oxides and sulfoxide species on its surface during oxidation, leading to worse floatability with xanthate in alkaline flotation conditions.

Chapter 5. Unraveling H_2O_2-stimulated Surface Oxidation of Hexagonal Pyrrhotite and Pentlandite by Underlying Electronic Structures

Abstract

The selective flotation of pentlandite from hexagonal pyrrhotite is a long-standing issue. To contribute to solving this issue, we report our fundamental understanding of selective depression of hexagonal pyrrhotite in pentlandite flotation using H_2O_2. Reactions of H_2O_2 were studied using chronopotentiometry (CP) tests and dissolved oxygen (DO) tests. Surface oxidations were studied with surface composition depth profiles of X-ray photoelectron spectrometry (XPS) and time-of-flight secondary ion mass spectrometry (ToF-SIMS). It was found that H_2O_2 reduction stimulated the surface oxidation of hexagonal pyrrhotite, meanwhile, H_2O_2 reduction on pentlandite was balanced by the oxidation of H_2O_2. The different responses to H_2O_2 conditioning were attributed to the distinct electronic structures of pyrrhotite and pentlandite, which were calculated based on density functional theory (DFT). For pyrrhotite, the higher S *3p* band center than its Fe *3d* band center suggests a strong interaction between surface sulfur anions and H_2O_2 redox reaction intermediates such as OH* and OOH*, resulting in easy sulfur oxidation. For pentlandite, the lower S *3p* band center than its metal *d* band center suggests a weak interaction between the sulfur anions and the H_2O_2 redox reaction intermediates, protecting sulfur from oxidation and rendering high catalysis effects to active metallic centers.

Key Words: electronic structures; surface oxidation; hydrogen peroxide; pentlandite; hexagonal pyrrhotite.

5.1. Introduction

As described in Section 3.1, the flotation separation of pentlandite from hexagonal pyrrhotite has been calling for more effective measures. There are many obstacles to exploring effective techniques because of the complexity of the system. For example, there is still a debate about the desirable chemical environment for separating pentlandite from pyrrhotite using flotation. Some researchers have claimed that a reducing environment helps to suppress xanthate oxidation on the pyrrhotite surface, rendering pyrrhotite more hydrophilic and less floatable [80, 91]. Other researchers have reported that an oxidizing environment plays a key role in the flotation separation of pyrrhotite and pentlandite [59, 92]. Explanations for the effective chemicals, like oxygen, in surface science studies mainly investigate the different surface species created by the surrounding chemical environment [55, 80, 116, 131, 146-149]. For example, the different oxidation levels of iron in these two sulfides were used to explain their different flotation behaviors [116, 131, 146]. It is important to note that the different oxidation levels of these two sulfides were rarely thoroughly explained, which makes it difficult to find more effective chemicals or techniques to selectively oxidize hexagonal pyrrhotite over pentlandite.

For understanding the oxidation differences between pyrrhotite and pentlandite, it is important to find the determining nature property for their surface oxidation and define the relation between the determining nature property and their surface oxidation. Chapter 4 focused on a similar topic and explained the different electrochemical oxidation rates of polymorphic pyrrhotite with their underlying electronic structures. Chapter 4 discovered that the electrochemical oxidation rate of polymorphic pyrrhotite depends on the Fe-S bond strength in the layer under the passivation layer, in which the Fe-S bond strength changed differently due to the different Fe *3d* band centers and S *3p* band centers of polymorphic pyrrhotite. Note that Chapter 4 aimed at studying sulfides with tiny differences, whose

similar chemical compositions and oxidation mechanisms enabled authors to explain the different electrochemical oxidation rates with the variation of the Fe-S bond strength (rate-determining parameter for pyrrhotite oxidation). For pyrrhotite and pentlandite, previous surface analysis studies showed that they form different oxidation products: the oxidation of pentlandite forms violarite ($FeNi_2S_4$) and a thin oxide layer with iron oxides and nickel oxides [64, 65, 149], the oxidation of pyrrhotite forms iron-deficient polysulfide species and a thin FeOOH overlayer due to the preferential outward-diffusion of iron over sulfur [28, 30, 31, 34, 36, 150]. Due to their different oxidation products, comparison of the oxidation of these two sulfides was usually accomplished by comparing the forming rate of iron oxide species, and the different oxidation rates were attributed to the different outward-diffusion rates of iron [116, 131]. Legrand attributed the faster oxidation rate of pyrrhotite than pentlandite to two possible reasons: (1) pyrrhotite contains structural vacancies that are helpful for iron diffusion; (2) the high-spin iron in pyrrhotite is more reactive than the low-spin iron in pentlandite [116, 131]. However, it is still difficult to confirm either one as the determining reason for the oxidation difference between pyrrhotite and pentlandite.

The different oxidation products on pyrrhotite and pentlandite surfaces suggested different oxidation mechanisms of these two sulfides, rendering the finding and comparing the rate-determining steps for the oxidation of pyrrhotite and pentlandite solely from their surface oxidation products extremely difficult. Importantly, the surface oxidation of metal sulfides is commonly stimulated by oxidants, and a relation between the catalyzed reactions, e.g., oxygen reduction reactions (ORR), and the S *3p* band centers of sulfides was defined by Tao et al. (Tao et al. found that a high S *3p* band center indicates a strong interaction between the surface sulfur anions and the catalysis reaction intermediates, resulting in a low catalysis effect of the active metallic center) [109]. Therefore, it is important to

consider the catalyzed reaction of oxidants together with the surface oxidation products of these two sulfides to find the determining nature property for their surface oxidation. For defining a clear relation between the underlying electronic structures and the H_2O_2-stimulated surface oxidation of these two sulfides, two main parts need to be studied. The first is to identify the reactions on the surface and within the crystal structures of hexagonal pyrrhotite and pentlandite during conditioning with H_2O_2. The second is to explore how these reactions get controlled by the electronic structures of pentlandite and hexagonal pyrrhotite. For learning more about these two areas, the redox reactions and changes in the species on the sulfide surfaces need to be studied and evaluated through understanding the role of the electronic structures of these two sulfides.

The objective of this Chapter is to fundamentally understand the different oxidation behaviors of hexagonal pyrrhotite and pentlandite within aqueous H_2O_2 solutions via electrochemical tests, surface characterizations, and density functional simulation (DFT) studies. This approach complements previous surface analysis studies on comparing the oxidation reactions of the pyrrhotite and pentlandite, which would help us to identify the key difference between pyrrhotite and pentlandite that could determine their surface oxidation in H_2O_2 solutions.

5.2. Materials and Methods

5.2.1. Materials and Chemicals

The hexagonal pyrrhotite electrode used in this study was from Virginia, USA. The pentlandite electrode came from Ontario, Canada. Potassium isobutyl xanthate (PIBX) used for the sulfide flotation experiments was obtained from Prospec Chemicals (Alberta, Canada) and further purified according to the procedure proposed by DeWitt and Roper [151]. The H_2O_2 used to condition the sulfide mineral was diluted from a 30 wt.% H_2O_2

water solution (Sigma-Aldrich). The pH 9.2 buffer solutions were prepared using sodium tetraborate decahydrate (≥ 99.5% purity, Sigma-Aldrich). Bulk mineral electrodes were prepared with a non-conductive epoxy (West System 105 epoxy resin and 205 hardener) and polished with sand-paper and diamond polishing suspensions (MetaDi Supreme) purchased from Buehler (Illinois, USA). Milli-Q water (≥18.2 MΩ·cm) used was produced from an Elix 3 Ultraviolet (UV) followed by a Milli-Q Academic water purification system (Millipore, Massachusetts, USA). The N_2 (99.998% purity) used for floating minerals and blow-drying electrode samples was purchased from Praxair Inc. (Connecticut, USA).

5.2.2. Electrochemical Tests

Electrode Preparation

The mineral electrodes were prepared, and their purity was confirmed using procedures detailed in Chapter 4 Section 4.2.1.

Open-circuit Chronopotentiometry, Linear Polarization Resistance, and Linear Sweep Voltammetry

Three electrochemical datasets were collected using two types of electrochemical tests. In the first test, which is less destructive to the electrode material, open-circuit chronopotentiometry (CP) was briefly interrupted by linear polarization resistance (LPR, from E_{oc}-20 mV to E_{oc}+10 mV at 2 mV/s) at (0, 3, 10, 30, and 60) min. Linear sweep voltammetry (LSV, from E_{oc}-200 mV to E_{oc}+500 mV at 5 mV/s) was carried out after the last LPR interruption at 60 min. In the second test, another CP test was conducted following a similar procedure with two major differences: (1) the CP was interrupted by LSV (from E_{oc}-200 mV to E_{oc}+200 mV at 5 mV/s) instead of LPR, and (2) the total length of the test was 3 h.

For each experiment, the electrode was polished with (600, 800, 1200, and 2500) grit sandpaper for 5 min with each grit and then on a polishing cloth with 9 μm, 3 μm, and 0.05 μm diamond suspension for another 5 min for each size. The well-polished electrode was then sonicated with an ultrasonic bath in Milli-Q water for 5 min and blown dry with N_2. The electrode was then immediately transferred into a 0.05 M $Na_2B_4O_7$ buffer solution (pH 9.2) with a certain H_2O_2 concentration for the electrochemical tests.

5.2.3. Surface Analyses

Time-of-Flight Secondary Ion Mass Spectrometry (ToF-SIMS) Depth Profiles

The electrode for the ToF-SIMS depth profile test was prepared by following the procedure described in Chapter 4 Section 4.2.1. The ToF-SIMS tests were conducted with the procedure described in Chapter 4 Section 4.2.2. The ToF-SIMS sputtering rate was calibrated on a silicon wafer as 1.3 Å/s, which was then calculated to be 1.6 Å/s when applied on a pyrrhotite surface and 1.3 Å/s when applied on a pentlandite surface (for details, please refer to Appendix B.4. Sputtering Rate of ToF-SIMS and XPS).

X-ray Photoelectron Spectroscopy (XPS) Depth Profiles

X-ray photoelectron spectroscopy (XPS) depth profiling was performed with a PHI Versa Probe III (PHI 5000) (ULVAC-PHI, Inc., Kanagawa, Japan) equipped with a monochromatic Al Kα X-ray source (1486.6 eV). An Ar^+ ion source (2 kV) was used to create a crater-shape dent of a 3 mm × 3 mm area. The spectra were obtained with a source power of 23.2 W from a 100 μm × 100 μm square in the center of the sputtered area. The Ar^+ beam sputtering rate was calibrated on a SiO_2 surface as 3.2 nm/min, which was then calculated to be 17.7 nm/min on a pyrrhotite surface and 14.0 nm/min on a pentlandite surface (for details, please refer to Appendix B.4. Sputtering Rate of ToF-SIMS and XPS).

The collected spectra were then deconvoluted with CasaXPS (Casa Software LTD., Devon, UK) to obtain subtle chemical structure information.

5.2.4. Dissolved Ion Analysis and Dissolved Oxygen (DO) Tests

To better understand the oxidation of pyrrhotite and pentlandite in H_2O_2 solutions, pyrrhotite and pentlandite powders (-74/+38 μm) were conditioned in a 5.29 mM H_2O_2, pH 9.2 borate buffer solution for 3 h. Prior to the conditioning, both sulfides were sonicated in an ultrasonic bath for 10 min to minimize surface oxidation products. During conditioning, 15 ml aliquots were taken from the conditioning solution at (10, 30, 60, 120, and 180) min. Aqueous concentrations of sulfate were determined with a colorimetric method by the Natural Resources Analytical Laboratory (NRAL, University of Alberta), and those of metal ions (iron and nickel) were analyzed with inductively couple plasma mass spectroscopy ICP-MS after acidification with HNO_3 at the Department of Earth and Atmospheric Science (EAS, University of Alberta) to gain insight into the pyrrhotite and pentlandite oxidation rates.

The oxidation reaction of the H_2O_2 on these two sulfide particles was evaluated by recording the variation of the DO concentration. The DO test setup is shown in Appendix B.2 (Figure B-6). Before every test, 1.5 g of mineral particles were agitated in an ultrasonic bath for 10 min. After agitation, the particles were immediately transferred into a 100 ml N_2-purged pH 9.2 borate buffer solution with the desired concentration of H_2O_2. The DO was recorded for 1 h with a polarographic probe (Orion 083005MD) and an Orion Versa Star Pro benchtop meter (Thermo Scientific, Massachusetts, USA).

5.2.5. Density Functional Theory (DFT) Simulation.

In this Chapter, all simulations were carried out within the periodic plane-wave DFT framework using the Vienna Ab initio Simulation Package (VASP) [152, 153] and were

conducted by Mohammad Khalkhali. The projector augmented wave (PAW) method was used to describe the core electrons and their interaction with the valence configuration ($3d^6 4s^2$ for iron, $4s^2 3d^8$ for nickel, and $3s^2 3p^4$ for sulfur) [154]. The generalized gradient Perdew, Burke, and Ernzerhof (PBE) [155] exchange-correlation density function with a plane-wave expansion energy cutoff of 400 eV was used in all simulations. 4×4×4 (pentlandite) and 4×4×2 (pyrrhotite) Γ-centered Monkhorst-Pack k–meshes were used for Brillouin-zone integrations. The energy convergence criterion for the electronic self-consistent calculation was 10^{-4} eV and the convergence in geometry optimization was reached when the Hellmann-Feynman forces on the internal coordinates and the cell parameters are better than 0.006 eV/Å.

The initial magnetic configuration of pyrrhotite was set as high spin distribution on Fe atoms with a ferrimagnetic orientation, as suggested in the previous studies [156, 157]. Meanwhile, the spin-polarization was excluded for the pentlandite simulation since initial trials showed that all spin-polarized simulations of pentlandite converged to the non-magnetic solution. The initial crystal structures of pyrrhotite came from experimental tests [156]. Determining the pentlandite ($(Fe,Ni)_9S_8$) crystal structure (a cubic structure, similar to $Fm\bar{3}m$ space group) presents a challenge in explicitly arranging the Fe and Ni atoms into the 4 octahedral and 32 tetrahedral sites. To address this challenge, we used a low-energy configuration proposed by Lu and Yu, in which the atomic distribution of Fe and Ni atoms was derived through a DFT investigation [158].

To improve the description of local states in the localized and strongly correlated electrons in *d* orbitals, we used the Dudarev et al. [159] approach of the DFT+U [160] method. The bulk electronic properties calculated by the DFT+U method highly depend on the U value.

To determine the appropriate U value, we calculated the U parameter with the linear response approach proposed by Cococcioni et al. (formula (5-1)) [161]

$$U = \chi^{-1} - \chi_0^{-1} \tag{5-1}$$

where χ^{-1} and χ_0^{-1} are matrixes calculated by non-self-consistent and self-consistent DFT simulations, respectively. Elements of a response matrix are defined as

$$\chi_{ij} = \frac{\partial N_i}{\partial V_j} \tag{5-2}$$

which is the change in the number of *d* electrons on site *i* due to an additional spherical potential acting on the *d* orbital on site *j*. The linear response method automatically treats atoms that are not symmetrically equivalent differently and may result in different U values for one lattice. To double-check the U values calculated by the response method, we considered P1 symmetry for all minerals studied here and compared the U values calculated for the symmetrically equivalent atoms. Please refer to Appendix B.6 DFT Simulation Results for the details of calculated U values (Table B-5) and bulk properties (Table B-4) calculated by the DFT+U simulations.

The partial charges, magnetic moments, and bond orders were calculated via the DDEC6 atomic population analysis, a refined approach of the Density Derived Electrostatic and Chemical (DDEC) approach, implemented in the Chargemol program [162, 163].

5.3. Results and Discussion

5.3.1. Electrochemical Tests

Flotation results (Figure B-5) showed that H_2O_2 could selectively depress the hexagonal pyrrhotite from the pentlandite by selectively oxidizing the hexagonal pyrrhotite. For understanding the distinct effects of H_2O_2 on the oxidation of the hexagonal pyrrhotite and the pentlandite, electrochemical tests were conducted.

Open-circuit Chronopotentiometry

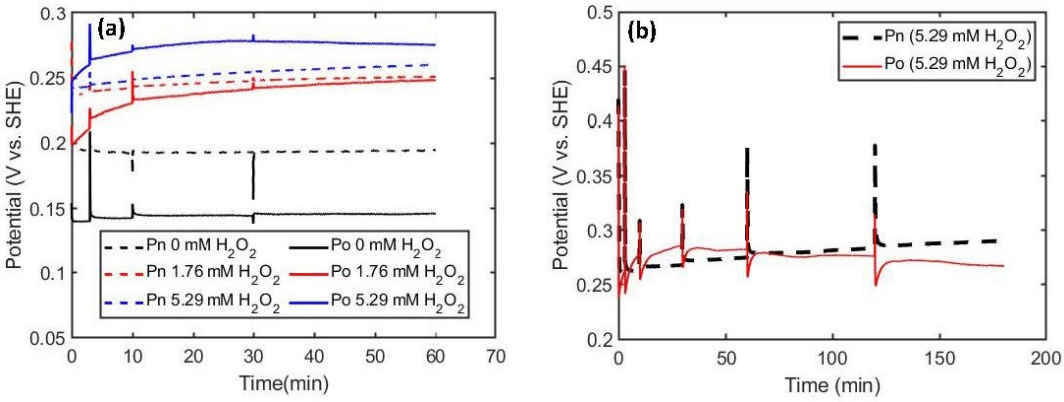

Figure 5-1. Open-circuit chronopotentiograms (CPs) for the stationary pentlandite (dashed lines) and hexagonal pyrrhotite (solid lines) electrodes intervened with LPR (a) and LSV (b) in pH 9.2 borate buffer solutions (0.05 M) with different concentrations of H_2O_2.

The CPs that intervened with LPR (Figure 5-1a) represent the continuous variation of the open-circuit potential (E_{oc}) during the one-hour conditioning of the sulfide electrode in pH 9.2 borate buffer solutions (0.05 M) with certain H_2O_2 concentrations. The hexagonal pyrrhotite showed a more dynamic response toward H_2O_2 conditioning than pentlandite in two aspects (Figure 5-1a). First, the E_{oc} of the hexagonal pyrrhotite increased more significantly over time than for the pentlandite in solutions with H_2O_2. Second, when the H_2O_2 concentration increased from 0 mM to 5.29 mM, the anodic shift of the initial E_{oc} of the hexagonal pyrrhotite (from 0.13 V to 0.25 V vs. SHE) was higher than that of the pentlandite (from 0.20 V to 0.24 V vs. SHE).

The CPs that intervened with LPR and LSV showed similar results for pentlandite, but an interesting difference was observed for the hexagonal pyrrhotite. When intervened with LSV, the CPs of the hexagonal pyrrhotite exhibited a sharp decrease in E_{oc} after the

interruption, followed by a quick increase. This phenomenon is further explained in the Section 5.3.7 Discussion.

Linear Polarization Resistance

To test the variation of the exchange current density (j_{ex}) and polarization resistance (R_p) during the H_2O_2 conditioning, LPR was conducted at (0, 3, 10, 30, and 60) min. The R_p was calculated using formula (5-3) and formula (5-4) [164, 165]. Note that the anodic (β_a) and cathodic (β_c) slopes in formula (5-4) were derived from the LSV at the end of the CP test (see Table B-2 and Figure B-8 in the Appendix B.3 Electrochemical Tests).

$$\left(\frac{\Delta E}{\Delta i}\right)_{E\to 0} = R_p = \frac{B}{i_{corr}} \tag{5-3}$$

$$\mathrm{B} = \frac{\beta_a \beta_c}{2.303(\beta_a + \beta_c)} \tag{5-4}$$

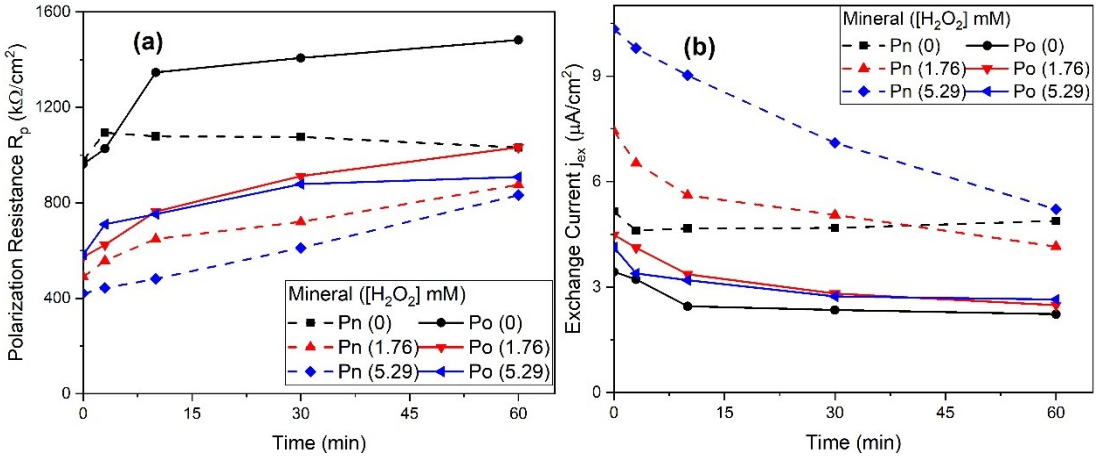

Figure 5-2. Comparison of (a) the polarization resistance (R_p) and (b) the exchange current density (j_{ex}) for the bulk pentlandite and the hexagonal pyrrhotite electrodes.[7]

[7] Note that the measured current in the LPR and LSV is named as the exchange current instead of corrosion current because the oxidation reactions on these two sulfide surfaces include both the mineral surface oxidation and the oxidation of H_2O_2 to O_2 (see Section 5.3.3 DO Tests).

In the solution without H_2O_2, the R_p of the hexagonal pyrrhotite increased over time, and the R_p of the pentlandite remained almost constant (Figure 5-2a). When the H_2O_2 concentration increased from 0 mM to 1.76 mM and then to 5.29 mM, the R_p of the pentlandite went up at an increasingly higher rate than the R_p of the hexagonal pyrrhotite (Figure 5-2a). The increase in the R_p of both sulfides can be attributed to reducing j_{ex} (Figure 5-2b). Figure 5-2b shows that when the H_2O_2 concentration increased from 0 mM to 1.76 mM and then to 5.29 mM, the j_{ex} of the pentlandite decreased at an increasingly higher rate than the j_{ex} of the hexagonal pyrrhotite. Reasons for the decrease of the j_{ex} (Figure 5-2b) on these two sulfide surfaces are further explained in Section 5.3.7 Discussion. It is also important to note that the j_{ex} of the pentlandite was nearly two times the j_{ex} of the hexagonal pyrrhotite. Note that similar changes of the j_{ex} of these two sulfides were observed in the CP tests intervened by the LSV (see Figure B-7).

5.3.2. Solution Analyses

Figure 5-3a shows that the aqueous sulfate concentration increased at a greater rate for the hexagonal pyrrhotite than the pentlandite. Meanwhile, Figure 5-3b displays a higher dissolving rate of iron from the hexagonal pyrrhotite than the pentlandite. Note that the solubility of nickel cations is higher than the solubility of iron cations in the pH 9.2 solution, making it difficult to compare the oxidation rate of pentlandite and hexagonal pyrrhotite via considering the nickel concentration.

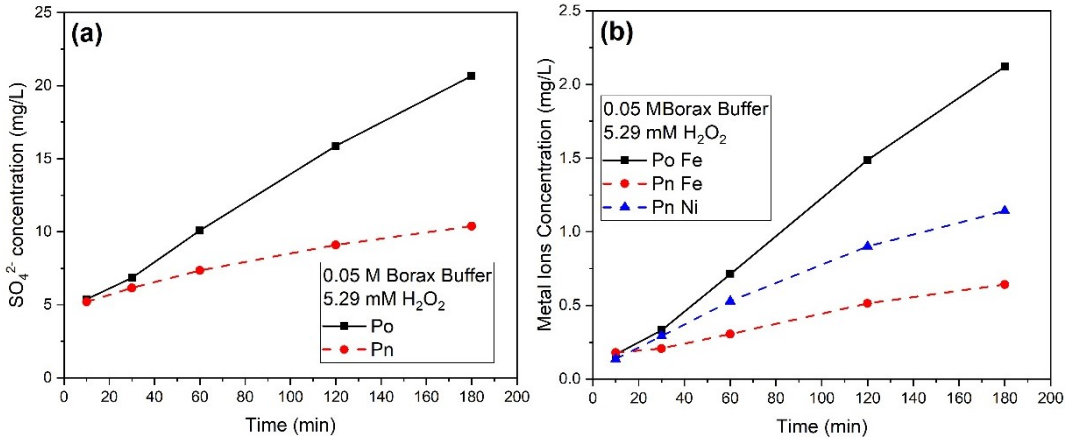

Figure 5-3. The variation of the concentration of SO_4^{2-} (a) and metal ions (b) when the hexagonal pyrrhotite and the pentlandite were conditioned respectively in pH 9.2 borate buffer solution with 5.29 mM H_2O_2.

5.3.3. DO Tests

To fully evaluate the oxidation reaction on pentlandite and hexagonal pyrrhotite during H_2O_2 conditioning, we conditioned mineral particles (the particle diameter ranges from 38 μm to 74 μm) in the N_2-purged pH 9.2 borate buffer solution with different H_2O_2 concentrations and recorded the changes of the DO concentration.

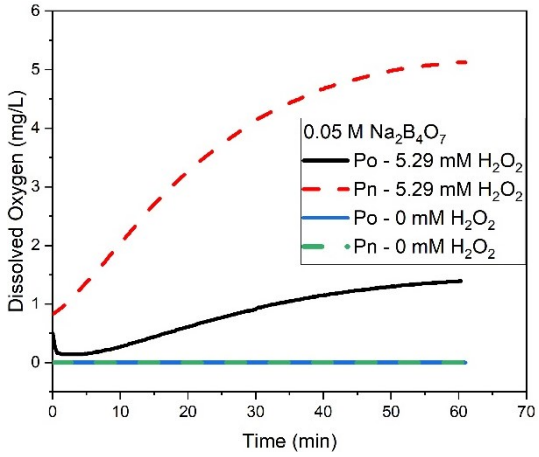

Figure 5-4. The variation of the concentration of the dissolved oxygen (DO) in the N_2-purged borate buffer solution with different H_2O_2 concentrations.

As shown in Figure 5-4, the DO concentration increased at a much higher rate in the pentlandite suspension than in the hexagonal pyrrhotite suspension. Assuming the appearance of molecular oxygen (O_2) is from the Fenton reaction of H_2O_2 with surface-bound Fe^{2+}/Fe^{3+} (see formula (B-10) to formula (B-13) in the Appendix B.5 Fenton Reactions of H_2O_2), DO production results in both anodic and cathodic processes at the mineral surfaces that have no net change in the oxidation state of the surface metal species. Since j_{ex} measures not only the reactions resulting in oxidation of the mineral but also the reactions involving aqueous species, faster catalytic production of DO results in a higher measured j_{ex}. This helps to explain why the pentlandite had a higher measured j_{ex} but a lower oxidative dissolution rate (sulfate concentration) in the solution with H_2O_2 than the hexagonal pyrrhotite. Furthermore, Figure 5-4 shows that the DO production rate of the pentlandite suspension decreased gradually, which is likely one important reason for the decrease of j_{ex} (Figure 5-2b) over time.

5.3.4. XPS Depth Profiles

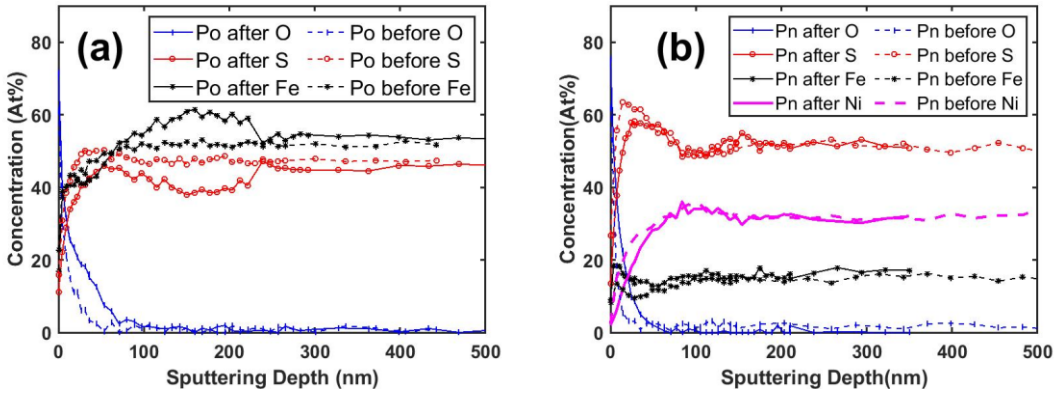

Figure 5-5. The atomic concentration variation of elements oxygen, sulfur, iron, and nickel in the hexagonal pyrrhotite (a) and the pentlandite (b) as a function of sputtering depth.

To study the impact of H_2O_2 on the surface composition of the hexagonal pyrrhotite and the pentlandite, we collected the XPS depth profile of sulfides before and after conditioning with 5.29 mM H_2O_2 for 3 h. The atomic concentration variation of elements O, Fe, Ni, and S within the crystal structure of these two sulfides is shown in Figure 5-5. Conditioning with H_2O_2 resulted in an increase in O and a decrease in S, with a stronger effect on the hexagonal pyrrhotite. As to the changes of the metal cations, the increase of Fe and decrease of Ni in the pentlandite passive layer (about 70 nm thick) suggested a preferential release of Ni over Fe. A strange change of the atomic percentage of Fe and S in deep layers (from ~70 nm deep to ~250 nm deep) of the hexagonal pyrrhotite was noticed, the reason for which is not known. The authors consider that it is possibly due to the ion bombardment (Ar^+), which can result in preferential sputtering. Research shows that the ion bombardment would preferentially sputter out the light element, as demonstrated for the pyrite [166]. However, there is still no agreement on the theory of preferential sputtering, particularly for the oxidized species, like the preferential sputtering exists for the Fe_2O_3 and Fe_3O_4, but not for FeO [167]. Based on the evidence that preferential sputtering exists for Fe_2O_3 and Fe_3O_4 but not for FeO, the argument that Fe(III)-O is essential for the preferential sputtering might be reasonable, which might even help to support that preferential sputtering exists for the oxidized pyrrhotite since the iron oxide on oxidized pyrrhotite is mainly in the form of Fe(III)-O. The preferential sputtering of the O over Fe might result in the accumulation of the Fe in the deeper layers. Note that the Fe(III)-O might be reduced to a lower oxidation state by the ion bombardment, like for Ta_2O_5 [168], and result in the simultaneous sputtering of the Fe and O. Therefore, an explicit explanation for the strange change of the atomic percentage of Fe and S in deep layers is still difficult even though the high concentration of the Fe in deep layers (from ~70 nm deep to ~250 nm deep) could be reasonably explained by the preferential sputtering of O and S.

Iron Spectra

The oxidation of pyrrhotite and pentlandite was further analyzed with the changes in the Fe *2p* spectra. Due to the unpaired electrons in the iron atom, the XPS peaks of the iron are split into multiplets [169, 170]. According to Pratt et al. [34, 150], the Fe $2p_{3/2}$ spectra can be fitted with three multiplets to represent the Fe(II)-S, Fe(III)-S and Fe(III)-O. They also developed the complex multiplet structures for all these three iron species (Fe(II)-S, Fe(III)-S, and Fe(III)-O), which were used in the fitting of the spectra presented in this study and listed in Table 5-1. Meanwhile, the Fe $2p_{3/2}$ of the pentlandite can be fitted with two singlets to represent fourfold-coordinated Fe(II)-S and the sixfold-coordinated Fe(II)-S and two multiplets to represent Fe(III)-S and Fe(III)-O (Table 5-2). Note that the multiplet structures of the Fe(III)-S and Fe(III)-O in pentlandite is similar to the multiplet structure of the Fe(III)-S and Fe(III)-O in pyrrhotite. In addition to the iron species, the Ni LMM Auger transitions also contribute to the intensity near 712.5 eV and 706.6 eV in the Fe $2p_{3/2}$ XPS spectra of pentlandite. For accounting for the Ni LMM Auger transitions, two broad peaks (full width at half maximum, FWHM = 3.2 eV) were included in fitting the Fe $2p_{3/2}$ spectra. The peak area of Ni LMM1 (712.5 eV) and Ni LMM2 (706.6 eV) is about 16 % and 7 % of the total area of Ni $2p_{3/2}$, respectively. The singlet peaks, individual multiplet peaks and the peak envelope generated are shown in Figure 5-6a, Figure 5-6b, Figure 5-6c, and Figure 5-6d. The binding energies and relative intensities of the individual multiplet peaks are listed in Table 5-1 and Table 5-2.

Table 5-1. Peak parameters, proportions, and corresponding chemical states information of XPS Fe $2p_{3/2}$ of the hexagonal pyrrhotite surface before and after H_2O_2 conditioning [34, 150].

Species	Peak	Binding Energy (eV)	FWHM (eV)	Area
Fe(II)-S	Multi. 1	706.2±0.1	1.3	1.00
	Multi. 2	+0.9	1.5	9.00
	Multi. 3	+2.2	1.3	3.30
	Multi. 4	+7.2	1.3	-
Fe(III)-S*	Multi. 1	709.0±0.2	1.3	1.00
	Multi. 2	+1.1	1.3	0.66
	Multi. 3	+2.1	1.3	0.35
	Multi. 4	+3	1.3	0.15
Fe(III)-O*	Multi. 1	710.4±0.1	1.6	1.00
	Multi. 2	+1	1.6	0.95
	Multi. 3	+2.2	1.6	0.59
	Multi. 4	+3.55	1.6	0.28

*Denotes multiplet structure

Po-before – hexagonal pyrrhotite electrode before being conditioned with H_2O_2

Po-after – hexagonal pyrrhotite electrode after being conditioned with H_2O_2

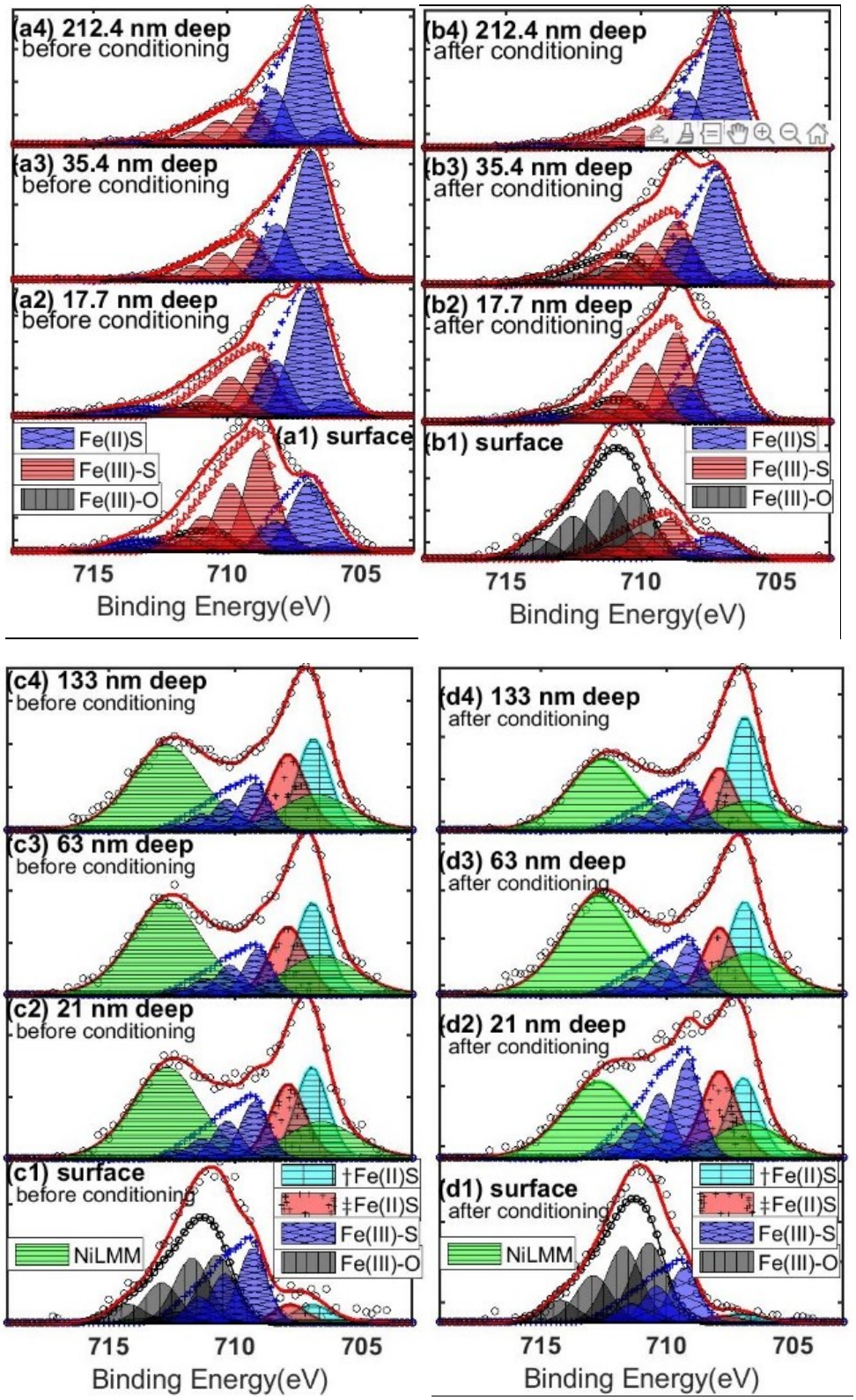
(a4) 212.4 nm deep
before conditioning
(a3) 35.4 nm deep
before conditioning
(a2) 17.7 nm deep
before conditioning
(a1) surface
Fe(II)S
Fe(III)-S
Fe(III)-O
715
710
705
Binding Energy(eV)
(b4) 212.4 nm deep
after conditioning
(b3) 35.4 nm deep
after conditioning
(b2) 17.7 nm deep
after conditioning
(b1) surface
Fe(II)S
Fe(III)-S
Fe(III)-O
715
710
705
Binding Energy(eV)
(c4) 133 nm deep
before conditioning
(c3) 63 nm deep
before conditioning
(c2) 21 nm deep
before conditioning
(c1) surface
before conditioning
†Fe(II)S
‡Fe(II)S
Fe(III)-S
Fe(III)-O
NiLMM
715
710
705
Binding Energy(eV)
(d4) 133 nm deep
after conditioning
(d3) 63 nm deep
after conditioning
(d2) 21 nm deep
after conditioning
(d1) surface
after conditioning
†Fe(II)S
‡Fe(II)S
Fe(III)-S
Fe(III)-O
NiLMM
715
710
705
Binding Energy(eV)

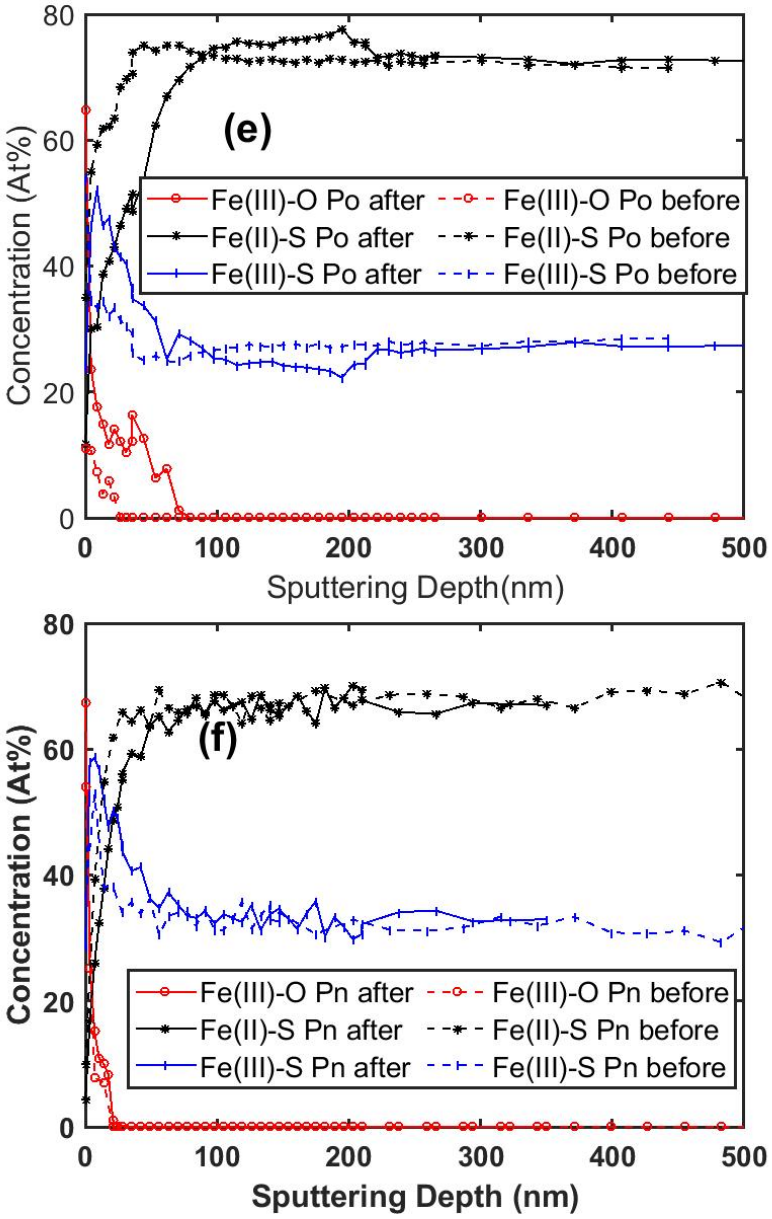

Figure 5-6. The fitting of the Fe $2p_{3/2}$ XPS spectra at several different depths of the hexagonal pyrrhotite before (a1, a2, a3, and a4) and after (b1, b2, b3, and b4) H_2O_2-conditioning; the fitting of the Fe $2p_{3/2}$ XPS spectra at several different depths of the pentlandite before (c1, c2, c3, and c4) and after (d1, d2, d3, and d4) H_2O_2-conditioning; comparison of the depth distribution of the deconvoluted Fe $2p_{3/2}$ species before (dashed line) and after (solid line) H_2O_2 conditioning for the hexagonal pyrrhotite (e) and the pentlandite (f).

Table 5-2. Peak parameters, proportions, and corresponding chemical states information of XPS Fe $2p_{3/2}$ of the pentlandite surface before and after H_2O_2 conditioning.

Species	Peaks Type	Binding Energy (eV)	FWHM (eV)	Area
Ni LMM1	Singlet	712.5	3.2	-
Ni LMM2	Singlet	706.6	3.2	-
Fe(II)-S†	Singlet	707.0	1.6	-
Fe(II)-S‡	Singlet	707.8	1.6	-
Fe(III)-S*	Multi. 1	709.0	1.3	1.00
	Multi. 2	710.1	1.3	0.66
	Multi. 3	711.1	1.3	0.35
	Multi. 4	712.0	1.3	0.15
Fe(III)-O*	Multi. 1	710.8	1.6	1.00
	Multi. 2	711.8	1.6	0.95
	Multi. 3	713.0	1.6	0.59
	Multi. 4	714.4	1.6	0.28

Fe(II)-S† denotes tetrahedrally coordinated ferrous sulfide

Fe(II)-S‡ denotes octahedrally coordinated ferrous sulfide

*Denotes multiplet structure

Pn-before – pentlandite electrode before being conditioned with H_2O_2

Pn-after – pentlandite electrode after being conditioned with H_2O_2

Comparison of the iron species before and after the H_2O_2 conditioning showed apparent differences among oxidation products on hexagonal pyrrhotite and pentlandite. As shown in Figure 5-6e and Figure 5-6f, the depth distribution of the major iron species indicated a similar increase of Fe(III)-S in both hexagonal pyrrhotite and pentlandite, while the increase of Fe(III)-O is more evident in the hexagonal pyrrhotite than in the pentlandite.

Sulfur Spectra

Table 5-3. Binding energies, FWHM, and area ratio of the doublets and the tail region used for fitting the S *2p* spectra of the Pentlandite [116, 131, 171].[8]

Species	Peak	Binding Energy (eV)	FWHM (eV)	Area
Pn-3 S^{2-}	Doublet	161.0	0.95	-
Pn-4 S^{2-}	Doublet	161.8	0.7	-
S_n^{2-}	Doublet	163.5	1.6	-
SOx^{2-}	Doublet	167.35	1.6	-
Pn-5 S^{2-}	Doublet	162.2	0.7	1.00
Pn-5 S^{2-} Tail 1		+0.5	×1.6	0.30
Pn-5 S^{2-} Tail 2		+1.6	×2.8	0.50
Pn-5 S^{2-} Tail 3		+3	×5.0	0.30

Pn-3 S^{2-}: threefold-coordinated sulfur species

Pn-4 S^{2-}: fourfold-coordinated sulfur species

Pn-5 S^{2-}: fivefold-coordinated sulfur species

[8] 3-S^{2-}: threefold-coordinated sulfur. 4-S^{2-}: fourfold-coordinated sulfur. 5-S^{2-}: fivefold-coordinated sulfur. 6-S^{2-}: sixfold-coordinated sulfur.

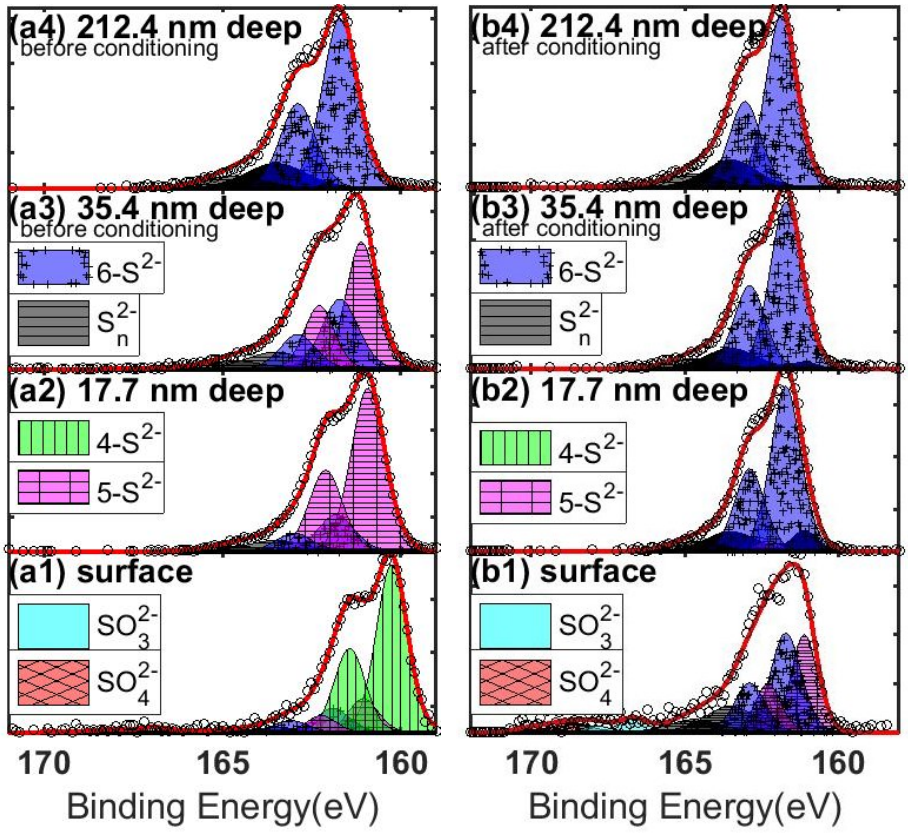
(a4) 212.4 nm deep
before conditioning
(b4) 212.4 nm deep
after conditioning
(a3) 35.4 nm deep
before conditioning
(b3) 35.4 nm deep
after conditioning
6-S2-
Sn2-
(a2) 17.7 nm deep
(b2) 17.7 nm deep
4-S2-
5-S2-
(a1) surface
(b1) surface
SO32-
SO42-
170
165
160
Binding Energy(eV)

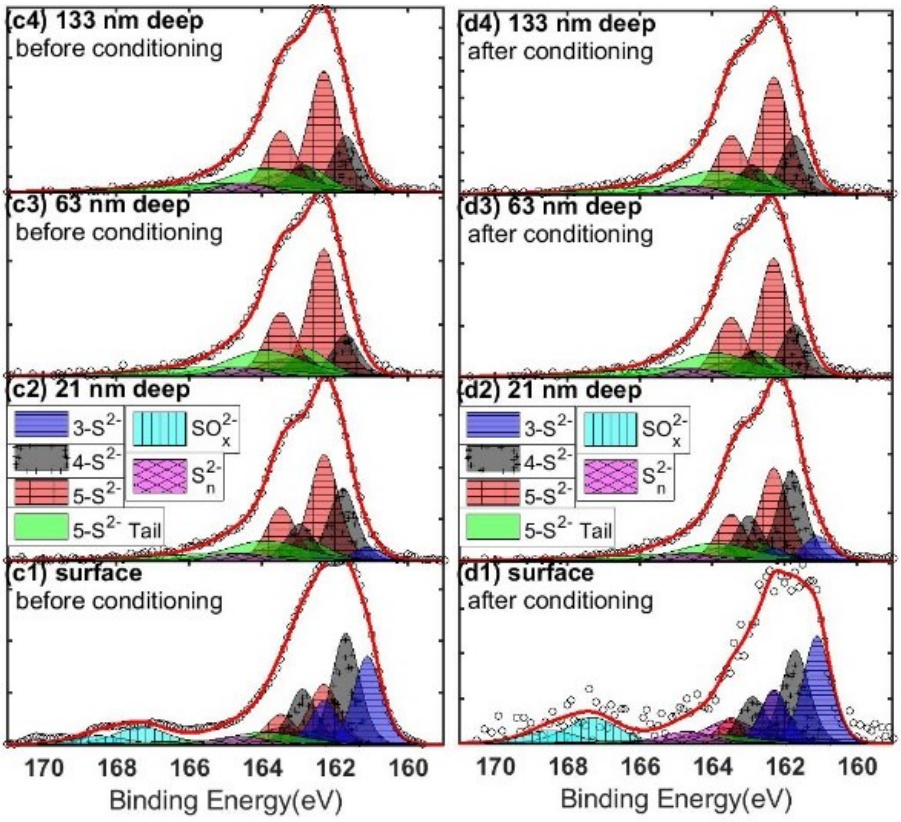
(c4) 133 nm deep
before conditioning
(d4) 133 nm deep
after conditioning
(c3) 63 nm deep
before conditioning
(d3) 63 nm deep
after conditioning
(c2) 21 nm deep
(d2) 21 nm deep
3-S2-
4-S2-
5-S2-
SOx2-
Sn2-
5-S2- Tail
(c1) surface
before conditioning
(d1) surface
after conditioning
170
168
166
164
162
160
Binding Energy(eV)

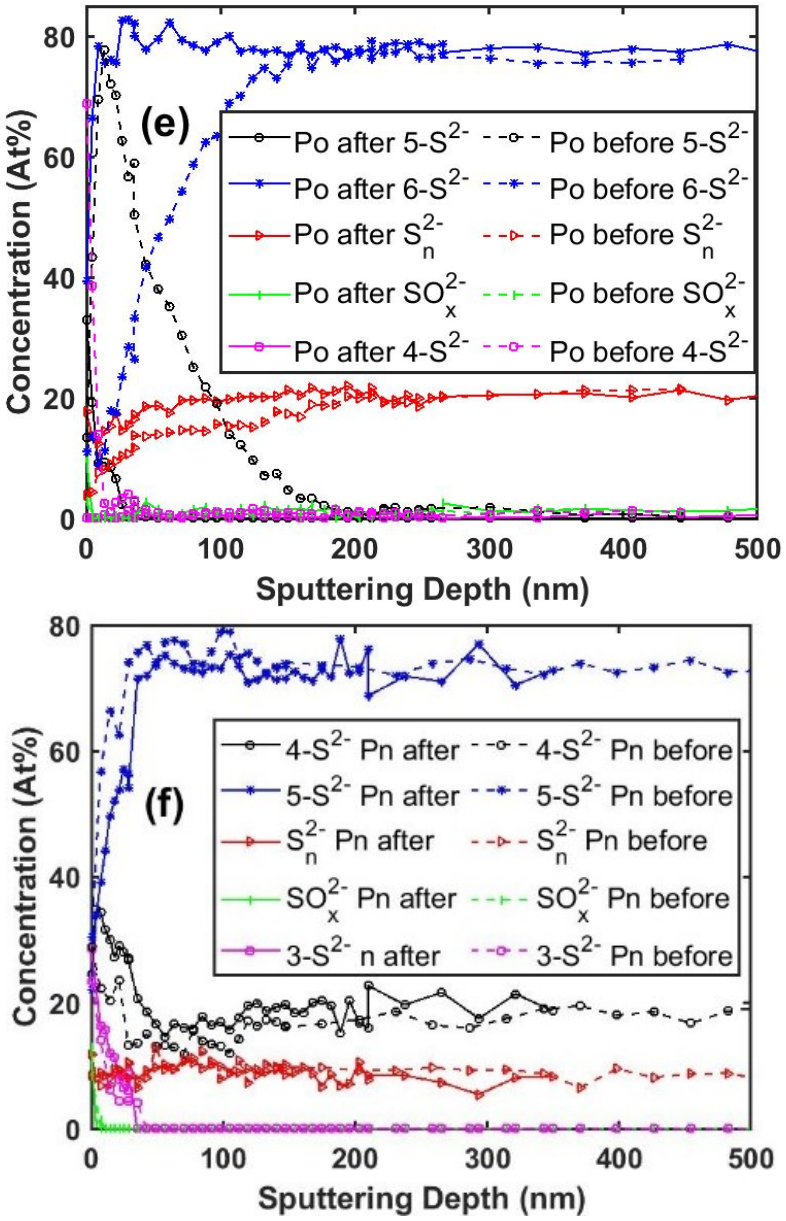

Figure 5-7. The fitting of the S *2p* XPS spectra at several different depths of the hexagonal pyrrhotite before (a1, a2, a3, and a4) and after (b1, b2, b3, and b4) H_2O_2-conditioning; the fitting of the S *2p* XPS spectra at several different depths of the pentlandite before (c1, c2, c3, and c4) and after (d1, d2, d3, and d4) H_2O_2-conditioning; comparison of the depth distribution of the deconvoluted S *2p* species before (dashed line) and after (solid line) H_2O_2-conditioning for the hexagonal pyrrhotite (e) and the pentlandite (f).

The S $2p_{3/2}$ and S $2p_{1/2}$ used for fitting the S *2p* spectra are of the same FWHM, and the area ratio of $2p_{3/2}$: $2p_{1/2}$ is constrained to 2:1 [135]. In addition, the binding energy of the $2p_{1/2}$ is 1.18 eV lower than the binding energy of $2p_{3/2}$. According to Pettifer et al. [171], the sulfur spectra of the pentlandite can be fitted with five doublets and one tail region to represent 3-coordinate sulfur, 4-cooridinate sulfur, 5-coordinate sulfur, polysulfides, and sulfoxide species. The tail region comprises three broad symmetric peaks and is fixed relative to the 5-coordinate S $2p_{3/2}$ peak. Detailed parameters of the S $2p_{3/2}$ peaks used for fitting the S *2p* spectra of pentlandite are listed in Table 5-3 and the fitting results are shown in Figure 5-7c and Figure 5-7d.

Except for the monosulfide, the peaks used for fitting the S *2p* spectra of the hexagonal pyrrhotite are mainly referenced from Legrand [116, 131] and are shown in Table 5-4. The S *2p* spectra of the pyrrhotite bulk could be fitted with one main monosulfide peak near 161.8 eV. However, the surface S *2p* spectra showed that the monosulfide appeared mainly around 160.3 eV and gradually shifted to 161.8 eV as the sputtering progress. Nesbitt et al. observed two monosulfide species in pyrrhotite surfaces and suggested that the XPS peak of the sixfold-coordinated sulfur is located around 0.9 eV higher than the XPS peak of the fivefold-coordinated sulfur [172]. XPS research about pentlandite and copper sulfides also showed that a low coordination number of the sulfur atoms rendered them low binding energy [65, 173]. Meanwhile, the formation of the iron-deficient sulfur-rich layers on pyrrhotite surfaces [34, 150] (Figure 5-5a) suggested that the sulfur atoms near pyrrhotite surfaces are of lower coordination than their bulk counterparts. Jones et al. [30] also observed that the acid reaction on pyrrhotite surface can restructure the pyrrhotite to the tetragonal Fe_2S_3, and Mycroft et al. [36] suggested that pyrrhotite oxidation in air can form disulfide and marcasite on pyrrhotite surfaces. Here, the peak around 160.3 eV and 161.0

eV was attributed to monosulfide species with lower coordination. For convenience, the peak around 160.3, 161.0, and 161.8 eV is named as the fourfold-coordinated sulfur, fivefold-coordinated sulfur, and sixfold-coordinated sulfur, respectively. Further studies are still required for accurately determining the sulfur coordination number for these three peaks.

Table 5-4. Binding energies and FWHM of doublets used for fitting the S *2p* spectra of the hexagonal pyrrhotite [8, 116, 131, 174].

Species	Peak	Binding Energy (eV)	FWHM (eV)
Po-4 S^{2-}	Doublet	160.3	1.1
Po-5 S^{2-}	Doublet	161.0	1.1
Po-6 S^{2-}	Doublet	161.8	1.1
S_n^{2-}	Doublet	163.6	1.9
$S_2O_3^{2-}$	Doublet	166.8	1.0
SO_4^{2-}	Doublet	168.8	1.4

Po-4 S^{2-}: fourfold-coordinated sulfur species

Po-5 S^{2-}: fivefold-coordinated sulfur species

Po-6 S^{2-}: sixfold-coordinated sulfur species

The depth distribution of the deconvoluted S *2p* species is shown in Figure 5-7e and Figure 5-7f. As to the sulfur species in the pentlandite, Figure 5-7f shows a decrease in the fivefold-coordinated sulfur and a simultaneous increase of the fourfold- and threefold-coordinated sulfur near the pentlandite surface both before and after H_2O_2 conditioning, with a slightly deeper effect observed after H_2O_2 conditioning. Meanwhile, Figure 5-7e shows that H_2O_2 conditioning significantly decreased the relative amount of the fourfold- and fivefold-coordinated sulfur and increased the relative amount of the sixfold-

coordinated sulfur. The decrease of the under-coordinated sulfur during the H_2O_2 conditioning is most likely due to the faster dissolution of sulfur over iron (Figure 5-3 and Figure 5-5).

5.3.5. ToF-SIMS Depth Profiles

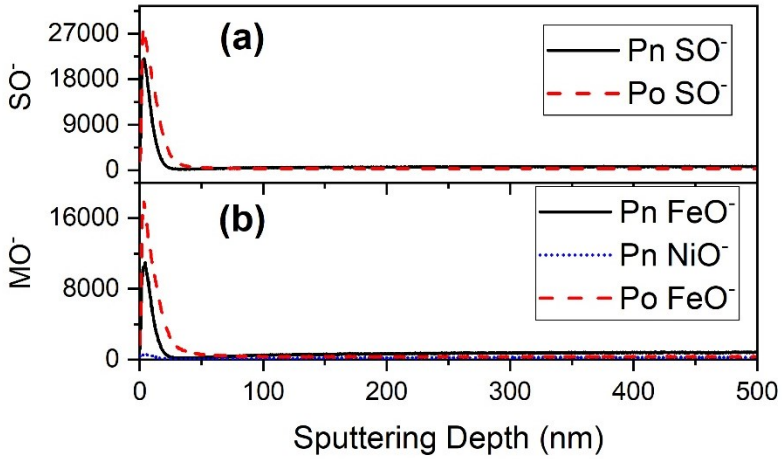

Figure 5-8. ToF-SIMS depth distribution of SO^- (a), FeO^-, and NiO^- (b) on the hexagonal pyrrhotite and the pentlandite. Electrodes were conditioned in the pH 9.2 borate solution with 5.29 mM H_2O_2 for 3 h.

To further confirm the effect of H_2O_2 on the chemical compositions of these two sulfides, we analyzed the H_2O_2-conditioned hexagonal pyrrhotite and pentlandite with ToF-SIMS. The ToF-SIMS depth profile showed that the very superficial layers of the H_2O_2-conditioned hexagonal pyrrhotite got more oxide species (FeO^-, NiO^-, and SO^-) than the pentlandite (Figure 5-8). Note that ToF-SIMS demonstrated that the sulfoxide species (SO^-) extended into slightly deep layers paralleling oxidation of iron (Figure 5-8a), while the XPS suggested that sulfoxide species (SO_x^{2-}) only existed on the mineral surfaces (Figure 5-8a). This apparent contradiction is because the *S 2p* peaks for sulfur bonded with one or two oxygen atoms (162.0 and 163.3 eV respectively [142]) overlap with peaks for sulfide,

disulfide, and polysulfide (See Table 5-3 and Table 5-4) and were completely obscured by these sulfides at depth in the XPS deconvolution analysis.

5.3.6. DFT Simulation Results

Figure 5-9 shows the calculated partial density of states (PDOS) for the optimized pyrrhotite and pentlandite unit cells, respectively. PDOS diagrams are normalized based on the number of corresponding atoms (Fe, Ni, or S) in their unit cells, the energy of the Fermi level (E_F) is set to 0 eV, and the bulk band centers are calculated according to formula (A-1) in the Appendix B.6 DFT Simulation Results .

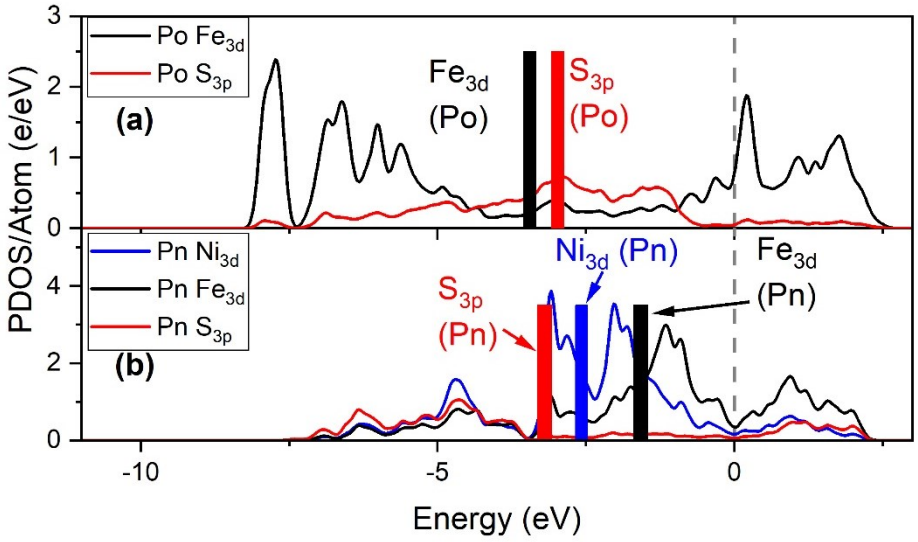

Figure 5-9. Partial density of states (lines) and the bulk band centers (including S *3p*, Fe *3d*, and Ni *3d*) of the pyrrhotite (a) and the pentlandite (b). Note that the height of the band center columns contains no physical meaning here.[9]

The catalytic activity of metal sulfides can be explained by the relative position of their metal *d* band center and the S *3p* band center. In metal sulfides, the metal cations work as

[9] This simulation work was carried out by Mohammad Khalkhali.

the active centers for the catalysis reaction, as the oxygen reduction reaction (ORR) [109], i.e., the catalytic activity of metal sulfides depends mainly on the interaction between adsorbates and the surface metal cations. Tao et al. proposed that the interaction between the adsorbates and the surface metal cations is affected by the interaction between the adsorbates and the surface sulfur anions: strong interaction between the adsorbates and the surface sulfur anions results in a weak interaction between the adsorbates and the surface metal cations and a weak catalytic role of the active metallic centers [109]. The intensity of the interaction between the adsorbates and the surface sulfur anions can be told via the relative position of the bulk S *3p* band center and metal *d* band center: a higher sulfur *3p* band center than the metal *d* band center means a strong interaction between the adsorbates and the surface sulfur anions [109]. Here, the higher Fe *3d* band center and Ni *3d* band center than the S *3p* band center in the pentlandite indicates a high catalytic activity; meanwhile, the lower Fe *3d* band center than the S *3p* band center of the pyrrhotite indicates a low catalytic activity.

The low sulfur stability of hexagonal pyrrhotite (Figure 5-3 and Figure 5-7e) can also be explained by the relative position of its metal *d* band center and S *3p* band center. During sulfur oxidation or dissociation, oxygen atoms form bonds with surface sulfur atoms and gradually weaken the surrounding metal-sulfur bonds until finally break them. For a configurative understanding of sulfur oxidation, readers can refer to Sit et al. research about pyrite oxidation [175]. The strong interaction between the adsorbates and the surface sulfur anions in pyrrhotite, as suggested by its higher S *3p* band center than Fe *3d* band center, is one important reason for the low stability of the sulfur in the hexagonal pyrrhotite. Another important reason for the low stability of the sulfur in the pyrrhotite is its weak metal-sulfur (Me-S) bonds, which are shown by the longer Me-S bonds of the pyrrhotite than the pentlandite (Figure B-9b).

5.3.7. Discussion

In the flotation tests, the H_2O_2 was employed to selectively separate the pentlandite from the hexagonal pyrrhotite (Figure B-5). For understanding the different oxidation behaviors of these two sulfides in the H_2O_2 solution, their responses toward the H_2O_2 were studied with electrochemical studies, DO experiments, solutions tests, and surface analyses. Detailed analysis of test results demonstrated different oxidation levels and different conditioning mechanisms of H_2O_2 on the pentlandite and the hexagonal pyrrhotite.

The surface and solution tests showed more severe oxidation of the hexagonal pyrrhotite than the pentlandite. XPS showed that iron in pentlandite oxidized from Fe(II)-S to Fe(III)-S (Figure 5-6f), while Fe(II)-S in the hexagonal pyrrhotite was oxidized to both Fe(III)-S and Fe(III)-O (Figure 5-6e). ToF-SIMS showed that the hexagonal pyrrhotite got more oxide species in its surface layers than the pentlandite (Figure 5-8). Solution analysis showed that the dissolution of iron and sulfur from the hexagonal pyrrhotite occurred at a much higher rate than from the pentlandite (Figure 5-3). The severe oxidation of the hexagonal pyrrhotite induced the accumulation of oxidized species, which, when effectively formed on the surfaces, can induce hydrophilicity, resulting in its flotation depression [176].

Monitoring the DO concentration during conditioning revealed distinct H_2O_2 conditioning mechanisms on these two sulfides that explain their electrochemical potential variation during the one-hour conditioning (Figure 5-1). Since DO comes from the oxidation of the H_2O_2, the increasing rate of DO reflects one part of the anodic current, with the rest part coming from the mineral surface oxidation. The lower surface oxidation rate of the pentlandite than the hexagonal pyrrhotite, together with the fact that the j_{ex} of the

pentlandite (Figure 5-2 and Figure B-7) is nearly two times of the j_{ex} of the hexagonal pyrrhotite in solutions with H_2O_2 suggested that the anodic current of ($H_2O_2 \rightarrow O_2$) on the pentlandite surface is higher than the anodic current coming from the pentlandite surface oxidation. Therefore, the oxidation of H_2O_2 to O_2 can be taken as the dominant oxidation reaction on the pentlandite surface. Meanwhile, the reduction of H_2O_2 to H_2O is taken as the dominant reduction reaction on both the hexagonal pyrrhotite and the pentlandite since H_2O_2 heightened their E_{oc} (Figure 5-1 and Figure B-5). Therefore, the variation of E_{oc} of the pentlandite (Figure 5-1) can be attributed to the change in the balance between the oxidation and reduction of H_2O_2. Meanwhile, the decrease of the j_{ex} of the pentlandite (Figure 5-2b) can be attributed to the decrease of DO increasing rate (Figure 5-4). Unlike the pentlandite, the variation of the E_{oc} of the hexagonal pyrrhotite (Figure 5-1) is attributed to the accumulation of the passive layer based on the following considerations. First, the low increasing rate of DO in the hexagonal pyrrhotite suspension indicates that the H_2O_2 oxidation rate is low (Figure 5-4). Second, the E_{oc} increasing rate of the hexagonal pyrrhotite in the H_2O_2 solution decreased gradually with time (Figure 5-1a), paralleling a decreasing accumulation rate of a passive layer. Third, the E_{oc} of the hexagonal pyrrhotite dropped after every LSV (from E_{oc}-200 mV to E_{oc}+200 mV) (Figure 5-1b), suggesting that the hexagonal pyrrhotite is susceptible to polarization. It is likely that the polarization partially changed or destroyed the oxidized surface species, driving the electrochemical potential to be slightly lower.

The distinct H_2O_2 conditioning mechanism on the hexagonal pyrrhotite and the pentlandite can be further explained by their different electronic structures. The fact that the j_{ex} of the pentlandite is two times higher than that of hexagonal pyrrhotite (Figure 5-2b) together with the fact that the redox reactions of H_2O_2 are dominant reactions on the pentlandite indicate a higher catalysis effect of the pentlandite to the redox reaction of H_2O_2 than the

hexagonal pyrrhotite. This higher catalysis effect of the pentlandite than the hexagonal pyrrhotite is attributed to their different electronic structures. According to Tao et al. [109], the S *3p* band center can reflect the contribution degree of the sulfide metallic cations to the catalytic activity of the whole mineral. The higher metal *d* band center than the S *3p* band center of the pentlandite (Figure 5-9) suggests that the electronic structures around the Fermi level are dominated by the metallic cations. In this case, the H_2O_2 can provide electrons at the anode and get oxidized, and obtain electrons at the cathode and get reduced. This is to say that a low competing capability of sulfur anions for the intermediates of the H_2O_2 redox reaction indicates a low effect of sulfur anions on the interaction between the H_2O_2 and surface metallic cations and hence a strong catalysis effect of pentlandite towards the redox reaction of H_2O_2. Meanwhile, the lower Fe *3d* band center than the S *3p* band center of the pyrrhotite reflects that sulfur anions dominate the electronic structures around the Fermi level. As a result, the H_2O_2 tends to obtain electrons from the sulfur, leading to sulfur lose electrons and get oxidized. The strong interaction between intermediates of the H_2O_2 redox reaction and the sulfur anions on the pyrrhotite surfaces turn out to be one important reason for the high sulfur dissolution rate from pyrrhotite (Figure 5-3) and the low stability of the under-coordinated sulfur (Figure 5-7e). Another important reason for the lower stability of sulfur in the pyrrhotite than sulfur in the pentlandite is that the pyrrhotite got weaker Me-S bonds than the pentlandite (Figure B-9b). Importantly, the lower stability of the sulfur in the pyrrhotite than that in the pentlandite helps to explain the different oxidations of their metal cations. For the hexagonal pyrrhotite, the easy dissociation of sulfur requires the fast infiltration of oxygen atoms to balance its surface charge, changing the iron from bonding with sulfur atoms to bonding with oxygen atoms. For the pentlandite, the slow sulfur oxidation and dissociation resulted in the slow incorporation of oxygen atoms, leading to the oxidation of iron from Fe(II)-S to Fe(III)-S (Figure 5-6f).

Importantly, the high catalyzing effects of the pentlandite can increase its hydrophobicity by promoting the oxidation of xanthate on its surfaces. As one of the most widely used collectors for sulfides, xanthate can enhance sulfide floatability via forming metal xanthates, dixanthogens, or a combination of both on sulfide surfaces. Among these forms, dixanthogens are the species responsible for the superior hydrophobicity of pentlandite and pyrrhotite [54, 80]. The adsorption (i.e., metal-xanthate) and oxidation (i.e., dixanthogen) of xanthates on sulfide minerals, as proposed by Tao et al. [109], depending on the catalytic effects of the metal atoms on sulfide surfaces. When the metal atoms exhibit weak catalytic effects toward reactions, like the oxygen reduction reaction (ORR), there is competing adsorption of the reactions intermediates onto surface sulfur and metal sites. Due to this competitive adsorption, oxygen atoms obtain electrons from the sulfur sites, enhancing the interaction between the xanthate anions and the surface metal sites (i.e., promoting the formation of metal-xanthate). Meanwhile, the strong catalytic effects of metallic centers toward ORR facilitate oxygen atoms to obtain electrons from xanthate (i.e., forming dixanthogen). The high catalytic effects of active metallic centers of pentlandite on the redox reaction of H_2O_2 suggested that the H_2O_2 obtained electrons from metallic centers, promoting dixanthogen formation on its surfaces.

It is important to note that the comparison of the H_2O_2 and O_2 would be extremely valuable since large-scale peroxide addition seems to be impractical in a mineral processing plant. However, this chapter aimed at fundamentally understanding the differential oxidation mechanism of non-magnetic pyrrhotite and pentlandite. Therefore, only H_2O_2 was used to investigate their distinctive oxidation behaviors since H_2O_2 can be easily controlled in the lab than oxygen. This chapter pointed out conditioning the pyrrhotite and pentlandite in a mildly oxidizing environment for a long enough time (like 30 mins or 1 h) would

significantly improve the flotation selectivity of pentlandite from non-magnetic pyrrhotite. Therefore, it is reasonable to assume that replacing the H_2O_2 with persisting and low-rate aeration would also help improve the flotation selectivity of pentlandite from non-magnetic pyrrhotite, which certainly requires further tests to explore the ideal condition.

5.4. Conclusions

In this Chapter, the H_2O_2-stimulated surface oxidation of hexagonal pyrrhotite and pentlandite was studied using electrochemical methods, surface analyses, solution tests, and DFT simulations. The following surface and solution analysis results support the finding that a one-hour low-concentration H_2O_2-conditioning oxidized the hexagonal pyrrhotite more severely than the pentlandite: (1) the higher iron and sulfate dissolving rate from the hexagonal pyrrhotite during H_2O_2 conditioning than from pentlandite; (2) more abundant FeO^- and SO^- species in the surface layers of the hexagonal pyrrhotite than the pentlandite; and (3) iron in the pentlandite oxidized from the Fe(II)-S to the Fe(III)-S while iron in the hexagonal pyrrhotite oxidized from the Fe(II)-S to both the Fe(III)-S and the Fe(III)-O. Their oxidation differences come from their different responses to the H_2O_2 conditioning. The H_2O_2 reduction induced significant surface oxidation and rapid accumulation of oxide species on its surfaces for the hexagonal pyrrhotite. While for pentlandite, the reduction of the H_2O_2 mainly induced the oxidation of the H_2O_2 to O_2, rendering limited effects on its surface oxidation. The different responses of the hexagonal pyrrhotite and the pentlandite to the H_2O_2-conditioning can be further explained by their distinct electronic structures. For pyrrhotite, the higher S *3p* band center than the Fe *3d* band center suggests a strong interaction between its sulfur anions and the catalytic reaction intermediates like OH* and OOH*, promoting its sulfur oxidation and sulfur dissociation. Meanwhile, the higher metal *d* band center than the S *3p* band center of the pentlandite suggests a weak interaction between the sulfur anions, which keeps the pentlandite from

oxidation and renders pentlandite strong catalysis effects. To conclude, both the catalysis reaction of H_2O_2 and the H_2O_2-stimulated surface oxidation can be explained by the different underlying electronic structures of the hexagonal pyrrhotite and pentlandite.

Chapter 6. A Fundamental Study of the Cu Activation Effects on the Hexagonal Pyrrhotite

Abstract

Pyrrhotite ($Fe_{(1-x)}S$, $0< x \leq 0.125$) is an important gangue mineral in Ni-Cu ores, which, when reported to the concentrate, wastes energy, and emits SO_2 in the metallurgical process. Pyrrhotite depression in the flotation of Ni-Cu ores has been a long-standing issue, which requires a better understanding of the pyrrhotite flotation behaviors in the complex chemical environment. Among all factors in the complex chemical environment, copper activation effects on pyrrhotite flotation have been identified and widely accepted. The present study aimed at fundamentally understanding the copper activation effects on the flotation of the hexagonal pyrrhotite by investigating Cu^{2+}'s effects on hexagonal pyrrhotite surface oxidation and xanthate adsorption to hexagonal pyrrhotite surfaces. The xanthate adsorption tests showed that copper promoted far more xanthate to adsorb on pyrrhotite surfaces than the amount of added Cu^{2+} (e.g., 0.005 μM Cu^{2+} increased another 0.0175 μM xanthate to adsorb on pyrrhotite surfaces compare to no Cu^{2+} condition), which indicated that Cu^{2+}'s effects on promoting xanthate adsorption are more than just working as bridges for xanthate adsorption. An investigation of the oxidation reactions on the hexagonal pyrrhotite surfaces with the cyclic voltammetry (CV) and the X-ray photoelectron spectroscopy (XPS) showed that the copper adsorption effectively inhibited the dissolution of sulfur, which is different from the traditional opinion that pyrrhotite oxidation depends on the outward diffusion rate of iron. Meanwhile, the XPS depth profile of the copper-activated hexagonal pyrrhotite showed that the Cu(I)S is the first and foremost species formed during copper activation. Cu(I)S came from the interaction between the Cu^{2+} and the surface sulfur anions, in which the Cu^{2+} was reduced to cuprous copper by oxidizing the surrounding sulfur anions. The formation of Cu(I)S means that the

surface sulfur anions can, at least partially, be occupied by Cu^{2+} ions. Based on this, it was proposed that the occupancy of the surface sulfur anions by Cu^{2+} ions reduced the interaction between surface sulfur anions and the oxygen atoms, leading to a low dissolution rate of the sulfur from the hexagonal pyrrhotite. Importantly, the weakened interaction between the surface sulfur anions and the oxygen atoms can render the hexagonal pyrrhotite strong catalysis effects toward the oxidation of xanthate to dixanthogen, further enhancing the floatability of the hexagonal pyrrhotite.

Keywords: hexagonal pyrrhotite; copper activation; flotation; Surface characterization.

6.1. Introduction

As described in Section 3.1 Introduction, pyrrhotite depression is essential in the flotation of Ni-Cu ores and requires a complete understanding of the responses of pyrrhotite towards the complex chemical environment. Among all factors in the complex chemical environment, copper activation on pyrrhotite flotation has been identified and widely accepted [61, 63, 174, 177-179], which is also well shown in Chapter 3. Becker's research on the polymorphic pyrrhotite implied the activation effect of Cu^{2+} ions [18]. Yoon et al. [59] showed that diethylenetriamine (DETA) could chelate the Cu^{2+} to effectively depress pyrrhotite in the flotation of Clarabelle Mill ore, indicating the strong activation effects of Cu^{2+} on the pyrrhotite flotation.

Previous investigations of the copper activation effects on pyrrhotite showed that the adsorbed copper could facilitate the adsorption of xanthate and the subsequent oxidation of xanthate to dixanthogen [56]. During the interaction between xanthate and copper-activated pyrrhotite surfaces, CuX_2 was considered formed initially and then oxidized to X_2 via the reduction of cupric copper [180]. Meanwhile, the copper's effect on increasing

the zeta potential of pyrrhotite was also claimed as a critical reason for promoting xanthate adsorption because a high zeta potential of pyrrhotite means a high coulombic attraction force between pyrrhotite and xanthate [62, 63]. Multani and Waters [181] showed that 10^{-4} M $CuSO_4$ increased the zeta potential of polymorphic pyrrhotite significantly. Acar and Somasundaran [62] showed that 10^{-2} M $CuCl_2$ reversed the pyrrhotite potential from negative to positive even at pH 10. However, copper's effects on improving the adsorption and oxidation of xanthate on pyrrhotite surfaces were not limited in these two parts because numerous studies claimed that the copper activation could efficiently protect pyrrhotite from oxidation [38, 61] and a low oxidation level of sulfide is important for the adsorption of xanthate [182-185].

Pyrrhotite oxidation mechanism is complicated and still not well defined, but numerous studies showed the formation of the oxide surface layer with abundant iron oxides and gradual sulfur enrichment during pyrrhotite oxidation [29, 30, 36, 150]. The chemical composition depth profile of the oxidized pyrrhotite surfaces with XPS, auger electron spectroscopy (AES), and Time-of-Flight secondary ion mass spectroscopy (ToF-SIMS) showed that pyrrhotite oxidation mainly involves, hence depends on, the outward-diffusion of iron atoms and electrons from inner layers to the top surfaces [34, 36, 37]. Meanwhile, oxygen atoms are incorporated by reducing the adsorbed oxygen molecules to O^{2-} by electrons diffused from the pyrrhotite interior [34]. Copper's effects on protecting pyrrhotite from severe oxidation were noticed but still not adequately understood.

For understanding copper's effects on protecting the pyrrhotite from surface oxidation, it is important to understand the copper adsorption mechanism. Early studies about copper adsorption suggested that copper adsorbed on pyrrhotite surface mainly via exchanging the ferrous iron on pyrrhotite surfaces. Recent research suggested that copper adsorption on

pyrrhotite mainly resembles the copper adsorption process on pyrite, in which Cu^{2+} is directly adsorbed on its surfaces and then reduced to cuprous copper by oxidizing the surrounding sulfur [38, 61]. Gerson [61] also noticed the ratio of Cu^{+}/Cu^{2+} ratio decreased with the increased oxidation of pyrrhotite, and the copper activation can protect the surface from severe oxidation. However, copper's effects on protecting the pyrrhotite surface from severe oxidation were still not thoroughly understood as well as that for the pyrrhotite oxidation.

For understanding copper's effects on protecting pyrrhotite oxidation, pyrrhotite electrodes oxidized in solution with and without copper ions was studied. Detailed analyses demonstrated that the copper adsorption did not affect the outward diffusion of iron as much as the dissolution of sulfur. Based on the analysis results, we proposed our explanations for the copper activation effects on pyrrhotite.

6.2. Materials and Methods

6.2.1. Materials and Chemicals

Single Mineral Preparation and Characterization

The hexagonal pyrrhotite used in this Chapter was of the same origin as Chapter 3, Chapter 4, and Chapter 5. Single hexagonal pyrrhotite minerals of -74/+38 μm size range were obtained via dry grinding, sieving, and magnetic separation (Frantz Magnetic Separator). For removing surface oxidation species, about 20 g of hexagonal pyrrhotite was added to 500 ml of Milli-Q water, and the suspension was sonicated (ultrasonic cleaning bath, Fisher, 9.5 L, 160 W output) for 1 min. The suspension then sat quiescently for 1 min, and the supernatant was decanted to separate the fine, peeled-off oxidized particles. The settled particles were then mixed with 500 ml of Milli-Q water, and the cleaning process repeated until the supernatant is clear after sonication. Surface-cleaned samples were then frozen

overnight in a freezer (-4 ℃) followed by drying in a freeze-dryer (Labconco Corporation, Missouri, USA). Well-dried samples were split into aliquots of desired weight using a Quantachrome rotary micro-riffler, and the aliquots were bagged into zipper seal sample bags. Zipper bags were then stored in bags vacuumed with a FoodSaver (V3835, Amazon), which were then placed in nitrogen-filled air-impermeable foil bags and stored in a Bel-Art desiccator (Fisher, 35 L, kept around 40 kPa) until further use.

Chemicals

Potassium isobutyl xanthate (PIBX), non-conductive epoxy, sand-papers, diamond polishing suspensions, N_2 gas, and Milli-Q water used in this chapter were the same as those used in Chapter 5. The copper(II) nitrate trihydrate (99%) obtained from the Thermo Fisher Scientific was used for preparing all copper solutions.

6.2.2. Micro-flotation Procedures

For every micro-flotation test, 1.5 g mineral particles were conditioned in a beaker and then floated in a Hallimond tube for 5 min. Before the micro-flotation, the mineral particles were cleaned by agitating in an ultrasonic cleaning bath for 10 min. Meanwhile, the pH 9.2 conditioning solution with specified copper concentration was prepared. After agitation, the supernatant water was emptied, and the agitated particles were transferred to the conditioning solution. Maintain the pH at 9.2 to condition the particles for 2 min and then add the PIBX to 2.65 μM to condition the particles for another 5 min. After conditioning, the pulp was transferred to the Hallimond tube to do the flotation. For the flotation, the N_2 was introduced at a rate of 30 cm^3/min, and the concentrates were collected at (1, 2, 5, 7, and 10) min. Each flotation condition was repeated at least three times to limit the errors.

6.2.3. X-ray Photoelectron Spectroscopy (XPS) Depth Profiles

Following the procedure described in Chapter 4, the bulk mineral electrodes were prepared and polished for the XPS depth profile tests. The XPS experiments were conducted with the same equipment and procedure as described in Section 5.2.3. Calibration of the sputtering rate of the Ar^+ beam on a SiO_2 surface confirmed the sputtering rate as 3.2 nm/min on SiO_2, which means 17.7 nm/min (3.2 nm/min × 5.53≈ 17.7 nm/min) on a hexagonal pyrrhotite surface as shown in formula (B-8) and Table B-3 (details were shown in Appendix B.4 Sputtering Rates of ToF-SIMS and XPS)**.** CasaXPS (Casa Software LTD., Devon, UK) was used for the deconvolution of the collected spectra.

6.2.4. Electrochemical Tests

The mineral electrodes were prepared, and their purity was confirmed using procedures described in Section 4.2.1.

Linear Sweep Voltammetry (LSV) Tests

For evaluating the variation of reaction rate on the hexagonal pyrrhotite surfaces, the LSV (from E_{oc}-200 mV to E_{oc}+200 mV at 5 mV/s) tests of the hexagonal pyrrhotite electrodes in the N_2-purged pH 9.2 borate solution (0.05 M $Na_2B_4O_7$) were conducted at (0, 3, 10, 30, 60, 120, and 180) min. The corrosion potential (E_{corr}) and corrosion current density (j_{corr}) were obtained by the Tafel analysis of the LSV data.

Cyclic Voltammetry (CV) Tests

CV tests were performed in a pH 9.2 borate solution (0.05 M $Na_2B_4O_7$) with a certain concentration of copper. Before the CV tests, the solution was deoxygenated by purging the solution with N_2 for 15 min. After polishing and rinsing with the procedure described in Chapter 4 Section 4.2.1, the electrode was immediately transferred into the de-oxygenated borate buffer solution. The electrode was firstly conditioned with the solution

for 5 min before conducting the CV test. For testing copper's effects on the hexagonal pyrrhotite oxidation, the CV scanning was commenced from an open circuit potential towards the positive direction at a 20 mV/s scan rate.

6.2.5. Ultraviolet-visible (UV-vis) Tests

For testing the amount of the adsorbed PIBX, 0.5 g hexagonal pyrrhotite mineral particles were conditioned in 50 ml pH 9.2 borate buffer solution (0.05 M $Na_2B_4O_7$) with a certain copper concentration for 5 min, and then the PIBX was added to 53 μM to condition mineral particles for another 10 min, followed by filtrating out the solution with a 0.02 μM syringe filter. Immediately after the filtration, the filtrate was tested in the UV-vis (Shimadzu UV-3600, Shimadzu Corporation, Kyoto, Japan). For each experiment, the hexagonal pyrrhotite mineral particles (+38/-74 μm) were gently ground in a mortar pestle within 5 ml borate buffer solution to smear against each other and expose new surfaces before conditioning. Each condition was repeated at least twice to confirm the stability of the result. Conditioning was achieved by shaking the solution on a shaker.

6.3. Results and Discussion

6.3.1. Flotation Results

As shown in Figure 6-1, the final hexagonal pyrrhotite flotation recovery at pH 9.2 gradually increased from around 50% to around 90% as the copper concentration increased from 0 μM/L to 8 μM/L. It is worth noting that the Cu^{2+} can increase the hexagonal pyrrhotite flotation recovery at a concentration as low as 0.5 μM/L.

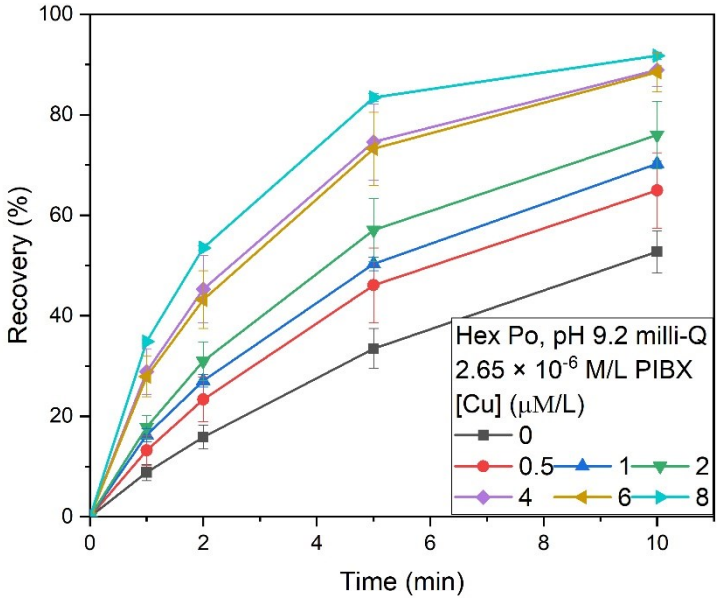

Figure 6-1. The flotation results of the hexagonal pyrrhotite at different copper concentrations

6.3.2. UV Tests

For understanding the copper activation mechanism on the hexagonal pyrrhotite, the amount of the xanthate adsorbed on the hexagonal pyrrhotite surfaces was calculated according to the remnant xanthate concentration (Table 6-1).Compared to the baseline (no Cu^{2+}), the copper increased the xanthate adsorption for all tested copper concentrations. When the copper concentration increased from 0 to (0.1, 1, and 10) μM/L, the remnant xanthate concentration changed from 25.6 μM/L to (22.1, 12.8, and 5.6) μM/L, respectively. This means that the 0.005 μM (0.1 μM/L × 0.05 L) Cu^{2+} increased 0.0175 μM ((25.6-22.1) μM/L × 0.05 L) xanthate adsorbed on pyrrhotite, 0.05 μM (1 μM/L × 0.05 L) Cu^{2+} increased 0.64 μM ((25.6-12.8) μM/L × 0.05 L) xanthate adsorbed on pyrrhotite, and 0.5 μM (10 μM/L × 0.05 L) Cu^{2+} increased 1 μM ((25.6-5.6) μM /L × 0.05 L) xanthate adsorbed on pyrrhotite, indicating that the adsorbed copper not only works as bridges for the xanthate

adsorption but also changed the surface chemical properties to facilitate xanthate adsorption on spots without copper.

Table 6-1. The remnant and adsorbed amount of xanthate onto the hexagonal pyrrhotite particles in pH 9.2 borax buffer solutions with different copper concentrations

$[Cu^{2+}]$ (μM/L)	Abs. of 300 nm	Remnant $[X^-]$(μM/L)	Adsorbed $[X^-]$(μM/L)	Adsorbed X^- (μM)
0	0.4506	25.6	27.4	1.37
0.1	0.3893	22.1	30.9	1.55
1	0.2258	12.8	40.2	2.01
10	0.0987	5.6	47.4	2.37

6.3.3. Electrochemical Experiments

LSV Tests

For understanding the copper activation mechanisms on the hexagonal pyrrhotite flotation, electrochemical tests were conducted. The changes in the corrosion current and the corrosion potential of the hexagonal pyrrhotite electrodes were calculated (Figure 6-2) from the LSV tests. Figure 6-2b showed that the corrosion potential of the hexagonal pyrrhotite in the solution with 2 μM Cu^{2+} and 20 μM Cu^{2+} got a higher rest potential than the hexagonal pyrrhotite in the solution without Cu^{2+}, which is most likely due to the oxidizing effects of Cu^{2+}. Meanwhile, the corrosion current density (j_{corr}) of the hexagonal pyrrhotite decreased when the concentration of Cu^{2+} increased from 0 μM to 2 μM and then to 20 μM (Figure 6-2a). In this electrochemical test, the surface oxidation of pyrrhotite is taken as the main oxidation reaction in the system. As we know, the surface oxidation rate of sulfides usually increases with the pulp potential. The low j_{corr} of pyrrhotite in solutions with 2 μM and 20 μM Cu^{2+} indicate that added copper cations inhibit the surface oxidation of the hexagonal pyrrhotite.

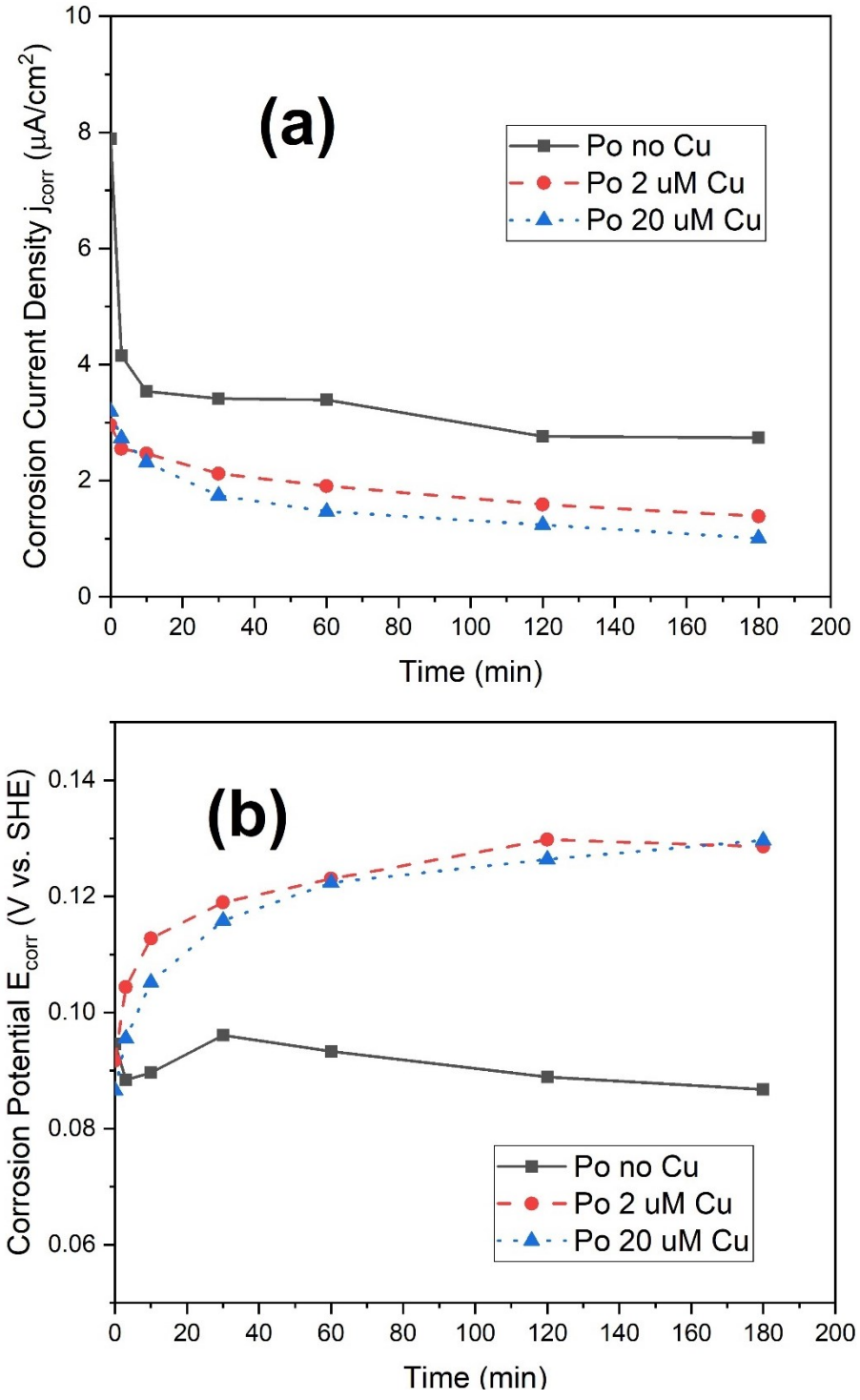

Figure 6-2. Variation of the corrosion current density (j_{corr}) (a) and corrosion potential (E_{corr}) (b) for the stationary hexagonal pyrrhotite electrode in pH 9.2 borate buffer solutions (0.05 M $Na_2B_4O_7$) with different Cu^{2+} concentration.

CV Tests

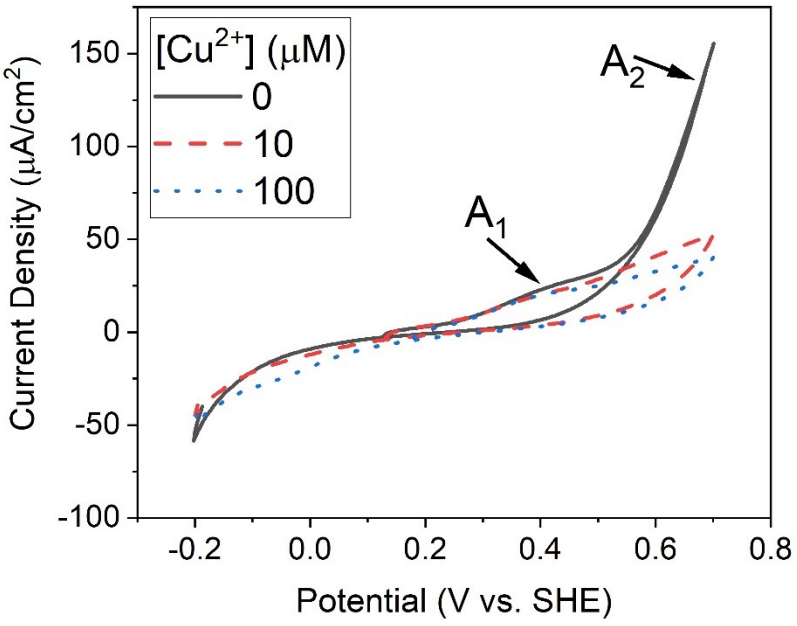

Figure 6-3. First cyclic voltammetry (CV) loop of the static hexagonal pyrrhotite electrode in the deoxygenated pH 9.2 borate buffer solutions (0.05 M $Na_2B_4O_7$) with different copper concentrations.

To further understand the effects of Cu^{2+} on the surface oxidation reaction of hexagonal pyrrhotite, the cyclic voltammetry (CV) tests were conducted to compare the surface oxidation reactions of hexagonal pyrrhotite under different copper concentrations. As shown in Figure 6-3, peak A_1 and A_2 are two dominant surface oxidation reactions of the hexagonal pyrrhotite. Previous research about pyrrhotite oxidation claimed that A_1 represented the oxidation reaction of pyrrhotite to the iron oxides and the iron-deficient sulfur-rich species (formula (6-1)), and A_2 represented the oxidation reaction of pyrrhotite to sulfate and ferric hydroxides (formula (6-2)) [38, 104]. CV tests (Figure 6-3) showed that when the copper concentration increased gradually from 0 μM to 10 μM and 100 μM, the peak intensity of A_2 decreased significantly while the peak intensity of A_1 remained

almost unaffected. The significant decrease of peak A_2 suggested that the adsorbed copper inhibited the oxidation of pyrrhotite to sulfate and ferric hydroxides on the pyrrhotite surfaces.

$$Fe_{1-x}S + 3yOH^- \rightarrow Fe_{1-x-y}S + yFe(OH)_3 + 3ye^- \quad (6\text{-}1)$$

$$FeS_{1.13} + 4.52H_2O \rightarrow Fe(OH)_3 + 1.13SO_4^{2-} + 9.04H^+ + 3e^- \quad (6\text{-}2)$$

6.3.4. XPS Depth Profiles

For further confirming Cu^{2+}'s effects on protecting the hexagonal pyrrhotite surfaces from oxidation, the hexagonal pyrrhotite mineral electrodes were oxidized in solutions with and without 10 μM Cu^{2+} and the oxidized surfaces were characterized with XPS. Figure 6-4a and Figure 6-4c showed the depth profiles of S *2p* and the O *1s* spectra of the hexagonal pyrrhotite oxidized in solutions with 10 μM Cu^{2+}, while Figure 6-4b and Figure 6-4d showed the depth profiles of the S *2p* and O *1s* of the hexagonal pyrrhotite electrode oxidized in solution without copper. The relative atomic percentage of S, O, Fe, and Cu were shown in Figure 6-4e. Oxidizing the hexagonal pyrrhotite in both solutions resulted in a surface with a low atomic concentration of sulfur and a high atomic concentration of oxygen on the hexagonal pyrrhotite surfaces, with a much deeper influence from the solution without Cu^{2+}. Meanwhile, pyrrhotite oxidation in these two solutions resulted in similar depth distribution of iron. Therefore, the copper adsorption on the pyrrhotite surfaces inhibited the fast oxidation and dissolution of sulfur from the hexagonal pyrrhotite crystal to the solution, which is consistent with the CV tests (Figure 6-3).

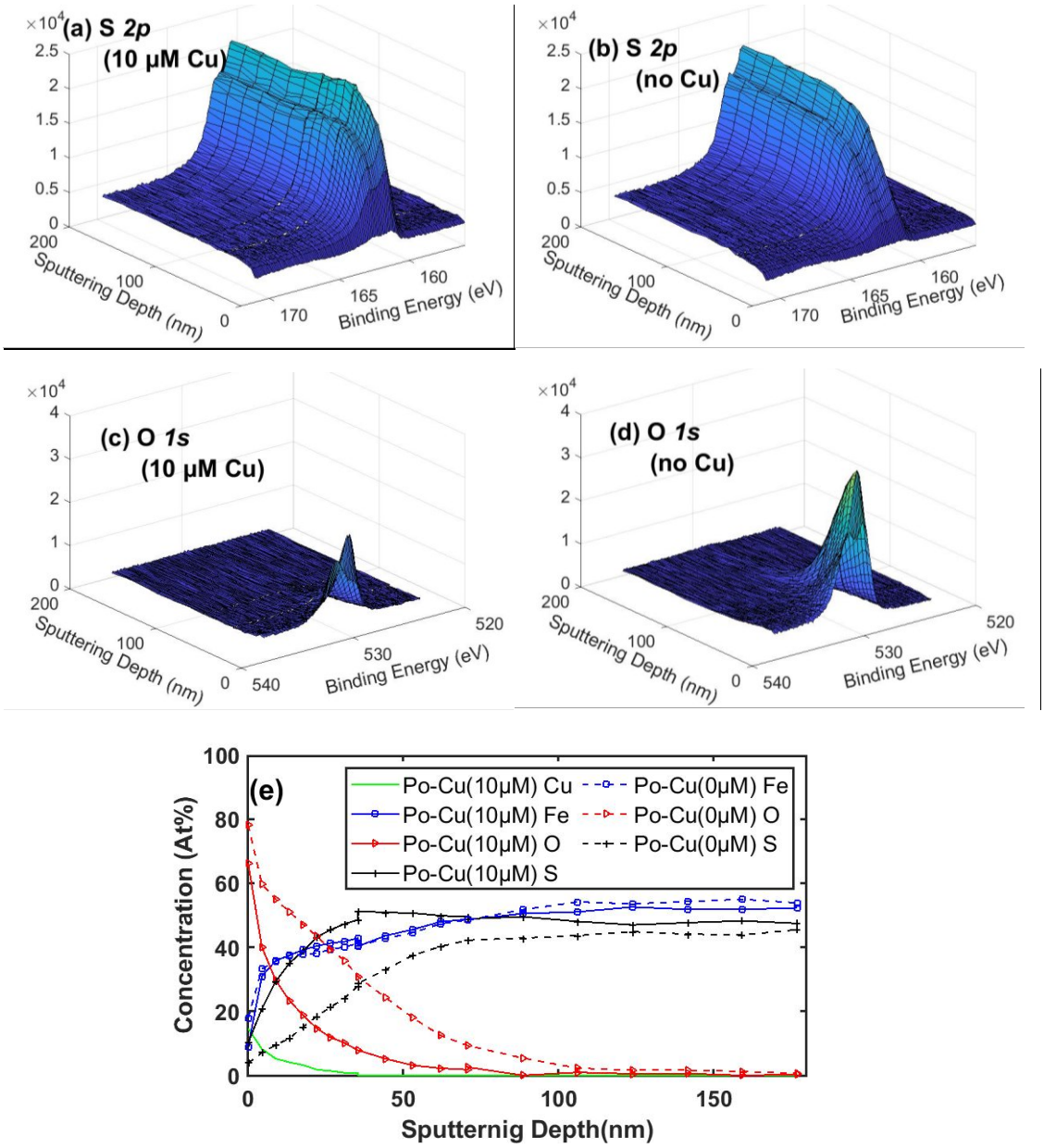

Figure 6-4. The depth profile of the S *2p* (a, b) and O *1s* (c, d) spectra of the Cu-activated (a and c) and non-activated (b and d) hexagonal pyrrhotite; (e) the variation of the atomic concentration of the S, O, Fe, and Cu as a function of depth in the Cu-activated (solid lines) and non-activated (dashed lines) hexagonal pyrrhotite.

For assessing copper's effects on the oxidation of iron in the hexagonal pyrrhotite, the Fe $2p_{3/2}$ spectra were deconvoluted. According to Pratt et al. [34, 150], the iron in the oxidized

pyrrhotite can be divided into three species: Fe(II)-S, Fe(III)-S, and Fe(III)-O. Due to the unpaired electrons in the iron atom, the XPS peaks of the iron were split into three multiplets. The complex multiplet structures for these three iron species (Fe(II)-S, Fe(III)-S, and Fe(III)-O) were developed by Pratt and used in the fitting of the spectra presented in this chapter (Figure 6-5a, Figure 6-5b and Table 6-2). Deconvolution of the Fe $2p_{3/2}$ (Figure 6-5c) showed that hexagonal pyrrhotite conditioned in the solution with 10 μM Cu^{2+} got less Fe(III)-O, less Fe(III)-S, and more Fe(II)-S species than the hexagonal pyrrhotite conditioned in the solution without Cu^{2+}. Therefore, the 10 μM Cu^{2+} also effectively prevented the oxidation of iron.

Table 6-2. Species, binding energies, FWHM, and area ratios for the multiplets used for fitting the Fe $2p_{3/2}$ of the oxidized hexagonal pyrrhotite [34, 150].

Species	Peak	Binding Energy (eV)	FWHM (eV)	Area
Fe(II)-S	Multi. 1	706.2±0.1	1.3	1.00
	Multi. 2	+0.9	1.5	9.00
	Multi. 3	+2.2	1.3	3.30
	Multi. 4	+7.2	1.3	-
Fe(III)-S*	Multi. 1	709.0±0.2	1.3	1.00
	Multi. 2	+1.1	1.3	0.66
	Multi. 3	+2.1	1.3	0.35
	Multi. 4	+3	1.3	0.15
Fe(III)-O*	Multi. 1	710.4±0.1	1.6	1.00
	Multi. 2	+1	1.6	0.95
	Multi. 3	+2.2	1.6	0.59
	Multi. 4	+3.55	1.6	0.28

*Denotes multiplet structure

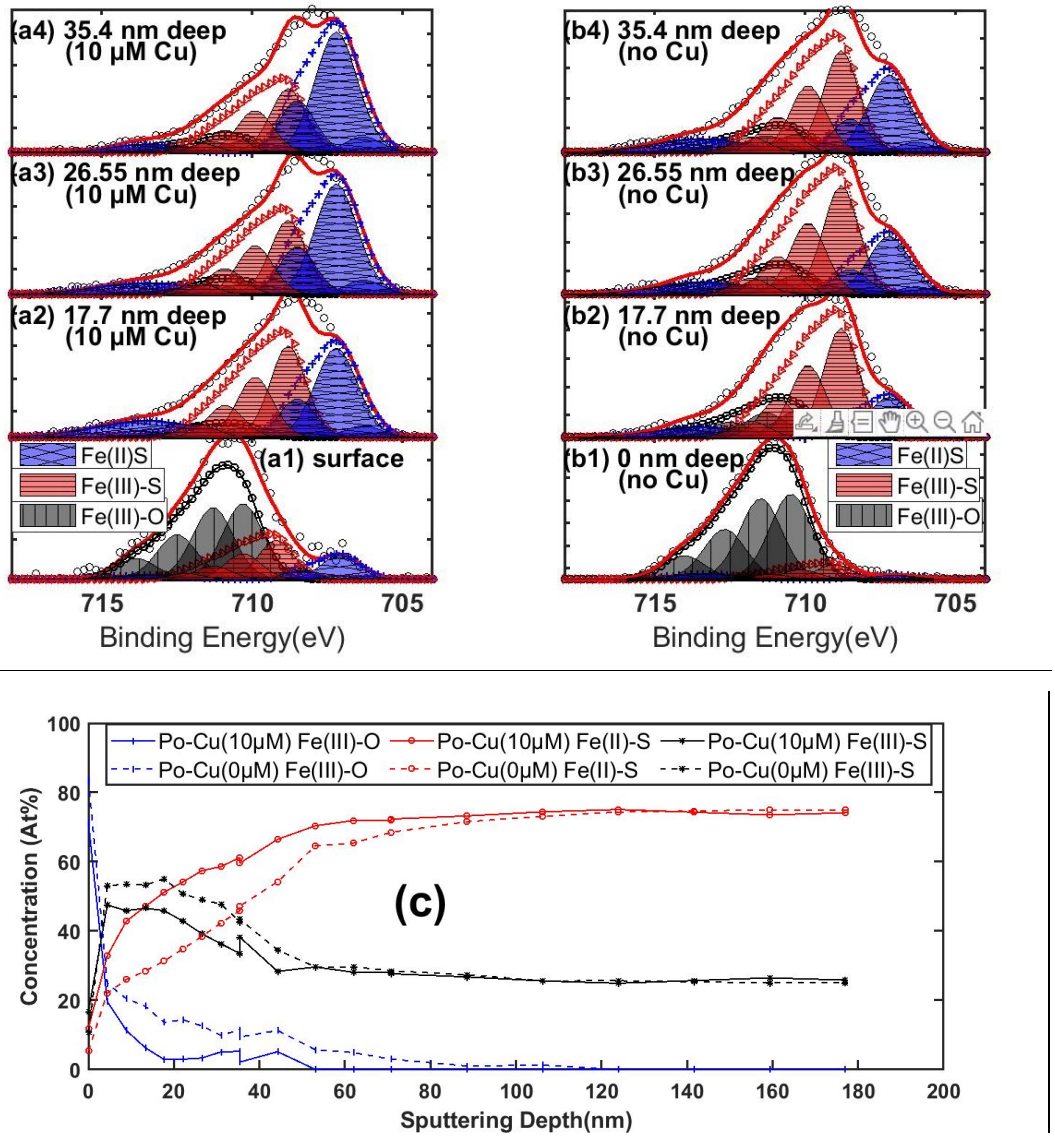

Figure 6-5. The fitting results of the Fe $2p_{3/2}$ spectra of the Cu-activated (a1, a2, a3, and a4) and non-activated (b1, b2, b3, and b4) hexagonal pyrrhotite at (0, 17.7, 26.55, and 35.4) nm deep; (c) the variation of the deconvoluted Fe $2p_{3/2}$ species as a function of depth for the Cu-activated (solid lines) and non-activated (dashed lines) hexagonal pyrrhotite.

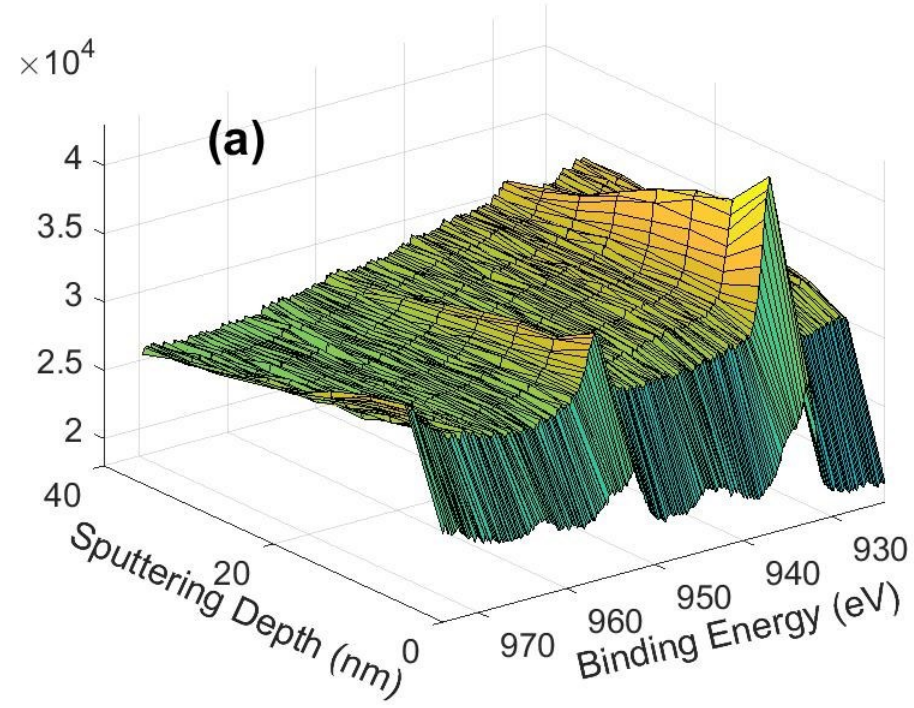
×10^4
(a)
4
3.5
3
2.5
2
40
20
0
Sputtering Depth (nm)
970
960
950
940
930
Binding Energy (eV)

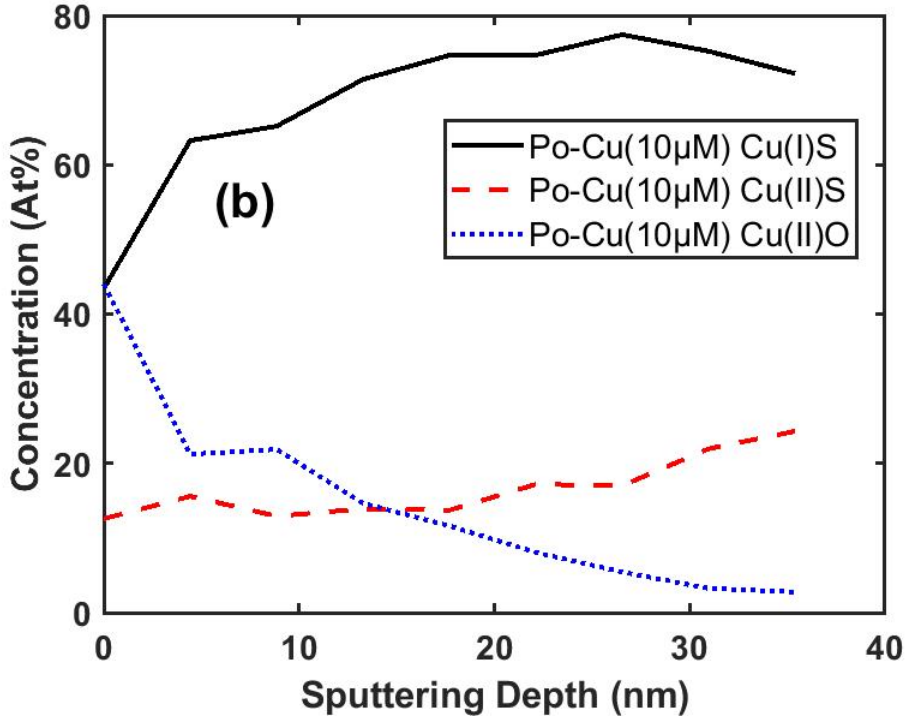
(b)
Po-Cu(10μM) Cu(I)S
Po-Cu(10μM) Cu(II)S
Po-Cu(10μM) Cu(II)O
Concentration (At%)
80
60
40
20
0
0
10
20
30
40
Sputtering Depth (nm)

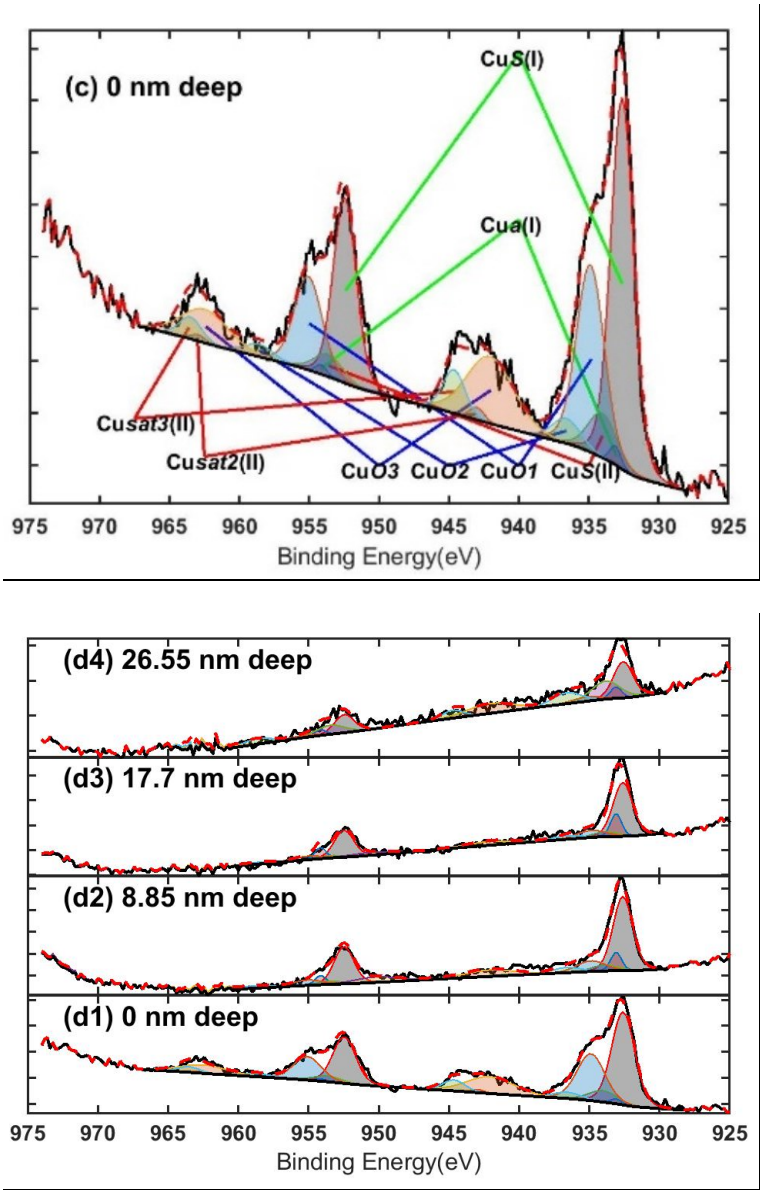

Figure 6-6. (a) The depth profile of the Cu *2p* spectra of the Cu-activated hexagonal pyrrhotite; (b) the variation of the copper species as a function of depth for the Cu-activated hexagonal pyrrhotite; (c) the fitting results of surface Cu *2p* spectra for the Cu-activated hexagonal pyrrhotite; (d) the fitting results of Cu *2p* spectra of the Cu-activated hexagonal pyrrhotite at (0, 8.85, 17.7, and 26.55) nm deep as indicated from d1 to d4 (the same fitting lines were used in (c) and (d)).

For further understanding the Cu^{2+}'s effects on preventing hexagonal pyrrhotite from oxidation, the Cu *2p* spectra were deconvoluted. The peak-fitting parameters developed by Cabrera-German et al. [186] were used in this chapter (Table 6-3 and Figure 6-6c) to determine the species of copper formed on the hexagonal pyrrhotite surfaces. As shown in Figure 6-6b, the relative atomic concentration of Cu(I)S increased with the sputtering depth, suggesting that copper is mainly incorporated into the hexagonal pyrrhotite crystal in the form of Cu(I)S during the initial activation. Meanwhile, Figure 6-6b showed that the increase of Cu(I)S with the sputtering depth happened simultaneously with the decrease of the CuO, suggesting that the copper sulfide species formed on the hexagonal pyrrhotite got gradually oxidized to CuO as the oxidation progresses.

Table 6-3. Species, peak labels, binding energies, spin-orbit splitting, and FWHM for the peaks used for fitting the Cu *2p* spectra of the Cu-activated hexagonal pyrrhotite [186].

Species	Peak label	$2p_{3/2}$ BE (eV)	Spin-orbit splitting (eV)	FWHM (eV)
Cu(I)S	CuS(I)	932.60 ± 0.01	19.86	1.935 ± 0.3
	Cua(I)	933.09 ± 0.05	21.05	0.83 ± 0.1
Cu(II)S	CuS(II)	933.93 ± 0.09	19.61	2.32 ± 0.1
	Cusat1(II)	941.67 ± 0.19	20.27	2.81 ± 0.1
	Cusat2(II)	943.08 ± 0.09	19.94	1.15 ± 0.1
	Cusat3(II)	944.68 ± 0.04	18.87	1.81 ± 0.1
Cu(II)O	CuO1	935.07 ± 0.17	20.19	2.32 ± 0.1
	CuO2	936.43 ± 0.17	21.98	2.32 ± 0.1
	CuO3	942.55 ± 0.50	20.43	4.08 ± 0.1
	CuO4	945.05 ± 0.50	18.06	4.08 ± 0.1

6.3.5. Discussion

This chapter investigated the copper activation mechanism on the hexagonal pyrrhotite by investigating the copper species formed on the hexagonal pyrrhotite surfaces, and copper's effects on the adsorption of xanthate and oxidation of the hexagonal pyrrhotite.

Analysis of results showed that the copper adsorption kept the hexagonal pyrrhotite from severe oxidation by preventing the sulfur dissolution. The LSV tests showed that the Cu^{2+} increased the corrosion potential of the hexagonal pyrrhotite but decreased its corrosion current density j_{corr} (Figure 6-2). Apparently, copper adsorption decreased the surface oxidation rate of the hexagonal pyrrhotite. According to the CV tests, the decreased oxidation rate is most likely due to the decreased oxidation rate of sulfur to sulfate and iron to ferric hydroxides (Figure 6-3), which has been further confirmed in the XPS studies (Figure 6-4). The XPS depth profile showed that the hexagonal pyrrhotite conditioned in the solution with 10 μM Cu^{2+} got much less amount of sulfur atoms replaced by the oxygen atoms, indicating that the 10 μM Cu^{2+} in the solution decreased the sulfur dissociation rate. Meanwhile, the XPS depth profile showed that the 10 μM Cu^{2+} protected Fe(II)-S in the hexagonal pyrrhotite from oxidizing to Fe(III)-O and Fe(III)-S.

For understanding Cu^{2+}'s working mechanism in keeping the sulfur from dissolution, it is important to first understand the oxidation and dissolution process of sulfur from metal sulfides. The interaction between the oxygen atoms with the surface sulfur anions was shown as the main process for sulfur oxidation and dissolution [175]. It is most likely that Cu^{2+} interfered with the direct interaction between surface sulfur anions and oxygen atoms. As the main form of the copper species incorporated into the hexagonal pyrrhotite crystal structure, the Cu(I)S came from the direct interaction between Cu^{2+} and sulfur anions,

during which the Cu(II) was reduced to Cu(I) by oxidizing surrounding sulfur species [61]. The occupancy of the readily active sulfur sites by the oxidant – Cu^{2+} would then keep the sulfur from interacting with the oxygen atoms, leading to a low oxidation and dissolution rate of sulfur. A low oxidation level of the pyrrhotite would promote more xanthate to adsorb on its surfaces, which explains why added Cu^{2+} promoted much more xanthates adsorb on the hexagonal pyrrhotite than its own amount (Table 6-1).

Importantly, a weak interaction between the sulfur anions and oxygen atoms might facilitate the oxidation of xanthate to dixanthogen on the hexagonal pyrrhotite surfaces to further enhance the hexagonal pyrrhotite floatability. According to Tao et al. [109], a strong interaction between the oxygen reduction intermediates (like OOH*, OH*, and O*) and the surface sulfur anions would render sulfides a low catalysis effect. Therefore, when the interaction between oxygen reduction intermediates and the surface sulfur anions gets blocked or partially inhibited, more xanthates can be oxidized to be dixanthogen, which is claimed as the species responsible for the superior hydrophobicity of pyrrhotite [54, 80].

6.4. Conclusions

In this study, the Cu^{2+}'s effects on improving the hexagonal pyrrhotite flotation were studied by investigating the effects of adsorbed copper on the surface oxidation of the hexagonal pyrrhotite and the adsorption of xanthate. The LSV tests showed that copper adsorption decreased the oxidation rate of the hexagonal pyrrhotite, which, according to the CV tests and the XPS studies, turns out to be the decreased dissolution rate of sulfur. Meanwhile, deconvolutions of the Cu *2p* spectra showed that Cu(I)S was the major activation species formed on hexagonal pyrrhotite surfaces. The Cu(I)S came from the interaction between Cu^{2+} and the readily active surface sulfur anions, and the formation of Cu(I)S indicated that the Cu^{2+} blocked or partially inhibited the interaction between the

oxygen atoms and the surface sulfur anions, decreasing the sulfur dissolution rate. Importantly, the weakened interaction between the surface sulfur anions and the oxygen atoms renders hexagonal pyrrhotite strong catalysis effects toward the oxidation of xanthate to dixanthogen, further enhancing the hexagonal pyrrhotite floatability.

Chapter 7. Conclusions and Future Work

7.1. Conclusions

The major findings of this thesis and contributions to engineering and science are listed as follows.

In plant surveys, the higher proportions of Fe(III)-O and SO_4^{2-} on pyrrhotite in the tail than that in the concentrate indicated that extensive oxidation is of key importance for pyrrhotite depression. Therefore, the higher floatability of hexagonal pyrrhotite than that of monoclinic pyrrhotite could be attributed to the naturally higher oxidation rate of the monoclinic pyrrhotite than that of the hexagonal pyrrhotite.

The pyrrhotite oxidation rate is related to the Fe-S bond strength since breaking Fe-S bonds is essential for the formation of oxidation products, such as polysulfides and iron oxy-hydroxides. ToF-SIMS depth profile showed that polymorphic pyrrhotite got similar Fe-S bond strength in bulk (layers deeper than 169 nm) but different Fe-S bond strength near the surface. Evaluation of the variation of the Fe-S bond strength with ToF-SIMS showed that the Fe-S bond strength decreased gradually over the 'defective layer' from 18.2 to 169 nm deep. Over this 'defective layer,' the Fe-S bond strength of the monoclinic pyrrhotite dropped more severely than that in the hexagonal pyrrhotite, which is correlated to the faster incorporation of the oxygen atoms into the monoclinic pyrrhotite than into the hexagonal pyrrhotite. The fast incorporation of the oxygen atoms into the monoclinic pyrrhotite reflected a high affinity of monoclinic pyrrhotite to the oxygen atoms. Meanwhile, the DFT simulation results showed that the Fe *3d* and S *3p* band centers of the monoclinic pyrrhotite are higher than those of the hexagonal pyrrhotite, which suggested that monoclinic pyrrhotite got more electrons near the Fermi level available for interacting with oxygen atoms than the hexagonal pyrrhotite.

As to the flotation depression of hexagonal pyrrhotite in the pentlandite flotation, Chapter 5 found that one-hour conditioning of the hexagonal pyrrhotite and pentlandite in 5.29 μM H_2O_2 can render hexagonal pyrrhotite more severely oxidized than pentlandite, leading to effective pyrrhotite depression in the pentlandite flotation. During the one-hour conditioning, the H_2O_2 selectively oxidized hexagonal pyrrhotite to enlarge the oxidation level difference between the hexagonal pyrrhotite and pentlandite. Investigations of the selective oxidation effects of the H_2O_2 showed that the H_2O_2 stimulated different reactions on the hexagonal pyrrhotite and pentlandite surfaces. On the hexagonal pyrrhotite surfaces, the reduction of the H_2O_2 was mainly balanced by its surface oxidation; on the pentlandite surfaces, the reduction of the H_2O_2 was mainly balanced by the oxidation of the hydrogen peroxide, indicating a high catalysis power of the metallic centers towards the redox reactions of the H_2O_2. The high catalysis effect of the metallic centers on the pentlandite surfaces is related to its electronic structure. DFT simulation showed that the metal *d* band center of the pentlandite is higher than its S *3p* band center, which means that the interaction between the metallic centers and the reactants on pentlandite surfaces is weakly affected by the sulfur atoms and hence the strong catalysis effect of the active metallic centers. Meanwhile, the S *3p* band center of the hexagonal pyrrhotite is higher than its Fe *3d* band center, indicated that the interaction between the metallic centers and the reactants on hexagonal surfaces is strongly affected by the sulfur atoms and hence a weak catalysis power of the metallic centers. In sum, the bulk electronic structure differences between the hexagonal pyrrhotite and the pentlandite enabled the H_2O_2 to selectively oxidize hexagonal pyrrhotite.

As to the copper activation effects on the pyrrhotite flotation, Chapter 6 showed that copper could effectively protect the pyrrhotite from severe oxidation. Electrochemical studies and

the XPS depth profiles showed that copper effectively hindered the oxidation and dissolution of sulfur from pyrrhotite. The decreased oxidation and dissolution rate of sulfur means a weak interaction between the surface-active sulfur anions and the adsorbed oxygen atoms since the oxidation and dissolution of sulfur involves the direct interaction between the sulfur anions and the adsorbed oxygen atoms. Meanwhile, XPS depth profiles showed that cupric ions mainly adsorbed in the form of Cu(I)S on the hexagonal pyrrhotite surfaces. Cu(I)S came from the reduction of Cu^{2+} and the oxidation of the surrounding sulfur anions, reducing the number of reactive sulfur anions to interact with oxygen atoms. It is important to note that a weak interaction between sulfur anions and oxygen atoms is helpful for xanthate adsorption and oxidation.

In summary, this study revealed that the flotation performance of polymorphic pyrrhotite and pentlandite is directly related to their oxidation behaviors, and their oxidation behaviors are controlled both by their electronic structures and the chemical environment. The higher electrochemical oxidation rate of monoclinic pyrrhotite than the hexagonal pyrrhotite is mainly due to their slight difference in their electronic structures. H_2O_2 can selectively oxidize hexagonal pyrrhotite since the hexagonal pyrrhotite and pentlandite responded differently towards reducing H_2O_2, which can also be attributed to their different electronic structures. Copper can reduce the interaction between adsorbed oxygen atoms and the surface reactive sulfur anions to protect pyrrhotite from severe oxidation, which reflected the important influence of the chemical environment. These findings are valuable for the fundamental studies of sulfides and flotation industries need finding more effective measures for the flotation separation of pentlandite from pyrrhotite.

7.2. Future Research

Findings in this study suggest some further research. Several possibilities are listed below.

(1) Chapter 6 revealed copper's effects on protecting the hexagonal pyrrhotite from oxidation. Therefore, it is essential to explore effective ways to enhance the interaction between the adsorbed oxygen atoms and the surface sulfur anions to enlarge the oxidation level differences between hexagonal pyrrhotite and pentlandite.

(2) Chapter 5 and chapter 6 showed the importance of considering the oxidation of sulfur over metal cations, which suggested that future research about sulfide oxidation needs to devote more effort to explore the sulfur dissolution instead of only focusing on the oxidation of metal cations.

(3) The exploration of the relation between surface oxidation and the electronic structures of polymorphic pyrrhotite and pentlandite showed the possibility of defining a relation between surface oxidation rates and their electronic structures that might fit for most sulfides.

References:

1. Barnes, H.L., *Geochemistry of hydrothermal ore deposits*. 1997: John Wiley & Sons.
2. de Villiers, J.P., D.C. Liles, and M. Becker, *The crystal structure of a naturally occurring 5C pyrrhotite from Sudbury, its chemistry, and vacancy distribution.* American Mineralogist, 2009. **94**(10): p. 1405-1410.
3. Multani, R.S. and K.E. Waters, *A review of the physicochemical properties and flotation of pyrrhotite superstructures (4C-Fe_7S_8/5C-Fe_9S_{10}) in Ni-Cu sulphide mineral processing.* The Canadian Journal of Chemical Engineering, 2018. **96**(5): p. 1185-1206.
4. Pósfai, M., T.G. Sharp, and A. Kontny, *Pyrrhotite varieties from the 9.1 km deep borehole of the KTB project.* American Mineralogist, 2000. **85**(10): p. 1406-1415.
5. Wang, H. and I. Salveson, *A review on the mineral chemistry of the non-stoichiometric iron sulphide, $Fe_{1-x}S$ ($0 \leqslant x \leqslant 0.125$): polymorphs, phase relations and transitions, electronic and magnetic structures.* Phase Transitions, 2005. **78**(7-8): p. 547-567.
6. Vaughan, D., E. Schwarz, and D. Owens, *Pyrrhotites from the Strathcona Mine, Sudbury, Canada; a thermomagnetic and mineralogical study.* Economic Geology, 1971. **66**(8): p. 1131-1144.
7. Theodossiou, A., *Measurements of the Hall effect and resistivity in pyrrhotite.* Physical Review, 1965.
8. Qi, C., et al., *Unraveling polymorphic pyrrhotite electrochemical oxidation by underlying electronic structures.* The Journal of Physical Chemistry C, 2019. **123**(43): p. 26442-26449.
9. Kondoro, J., *Mössbauer study of vacancies in natural pyrrhotite.* Journal of alloys and compounds, 1999. **289**(1-2): p. 36-41.
10. Levinson, L.M. and D. Treves, *Mössbauer study of the magnetic structure of Fe_7S_8.* Journal of Physics and Chemistry of Solids, 1968. **29**(12): p. 2227-2231.
11. Corlett, M., *Low-iron polymorphs in the pyrrhotite group.* Zeitschrift für Kristallographie-Crystalline Materials, 1968. **126**(1-6): p. 124-134.
12. Kitamura, M., M. Tokonami, and N. Morimoto, *Distribution of titanium atoms in oxy-kaersutite.* Contributions to Mineralogy and Petrology, 1975. **51**(3): p. 167-172.
13. Ôno, K., A. Ito, and E. Hirahara, *Mössbauer study of hyperfine field, quadrupole interaction, and isomer shift of Fe^{57} in $FeS_{1.00}$, $FeS_{1.05}$ and $FeS_{1.07}$.* Journal of the Physical Society of Japan, 1962. **17**(10): p. 1615-1620.
14. Igaki, K., M. Sato, and T. Shinohara, *Mössbauer study on the distribution of iron vacancies in iron sulfide $Fe_{1-x}S$.* Transactions of the Japan Institute of Metals, 1982. **23**(5): p. 221-228.

15. Igaki, K., M. Sato, and T. Shinohara, *Mössbauer study on the iron vacancy distribution in iron sulfide $Fe_{1-x}S$ ($0.083 \leqslant x \leqslant 0.125$).* Transactions of the Japan Institute of Metals, 1981. **22**(9): p. 627-632.
16. Marusak, L. and L. Tongson, *Soft X-ray emission and Auger electron spectroscopic study of FeS, $Fe_{0.9}S$, $Fe_{0.875}S$, and $Fe_{0.5}S$.* Journal of Applied Physics, 1979. **50**(6): p. 4350-4355.
17. O'Reilly, W., et al., *Magnetic properties of synthetic analogues of pyrrhotite ore in the grain size range 1-24 μm.* Geophysical Journal International, 2000. **142**(3): p. 669-683.
18. Becker, M., *The mineralogy and crystallography of pyrrhotite from selected nickel and PGE ore deposits and its effect on flotation performance*. 2009, University of Pretoria.
19. Kolahdoozan, M., *Adsorption and flotation characteristics of hexagonal and monoclinic pyrrhotite*. 1996.
20. Lawson, V., et al. *The separation of pentlandite from chalcopyrite, pyrrhotite and gangue in nickel projects throughout the world*. in *Proceedings Twelfth Mill Operators Conference*. 2014.
21. Janzen, M.P., *Role of ferric iron, trace metal content, and crystal structure on pyrrhotite oxidation*. 1996, University of Waterloo.
22. Yakhontova, L., L. Nesterovich, and A. Grudev, *New data on natural oxidation of pyrrhotite.* Vestnik Moskovskogo Universiteta Geologiya, 1983. **38**: p. 41-44.
23. Miller, J., et al., *A review of pyrrhotite flotation chemistry in the processing of PGM ores.* Minerals Engineering, 2005. **18**(8): p. 855-865.
24. Grønvold, F. and S. Stølen, *Thermodynamics of iron sulfides II. Heat capacity and thermodynamic properties of FeS and of $Fe_{0.875}S$ at temperatures from 298.15 K to 1000 K, of $Fe_{0.98}S$ from 298.15 K to 800 K, and of $Fe_{0.89}S$ from 298.15 K to about 650 K. Thermodynamics of formation.* The Journal of Chemical Thermodynamics, 1992. **24**(9): p. 913-936.
25. Wang, H., et al., *Effect of cation vacancy and crystal superstructure on thermodynamics of iron monosulfides.* Journal of Sulfur Chemistry, 2006. **27**(03): p. 271-282.
26. Hu, Y., W. Sun, and D. Wang, *Electrochemistry of flotation of sulphide minerals*. 2010: Springer Science & Business Media.
27. Buckley, A., I. Hamilton, and R. Woods, *Studies of the surface oxidation of pyrite and pyrrhotite using X-ray photoelectron spectroscopy and linear potential sweep voltammetry.* 1988.
28. Buckley, A.N. and R. Woods, *X-ray photoelectron spectroscopy of oxidized pyrrhotite surfaces: I. Exposure to aire.* Applications of Surface Science, 1985. **22**: p. 280-287.

29. Buckley, A.N. and R. Woods, *X-ray photoelectron spectroscopy of oxidised pyrrhotite surfaces.* Applications of Surface Science, 1985. **20**(4): p. 472-480.
30. Jones, C.F., et al., *Compositional and structural alteration of pyrrhotite surfaces in solution: XPS and XRD studies.* Applied Surface Science, 1992. **55**(1): p. 65-85.
31. Belzile, N., et al., *A review on pyrrhotite oxidation.* Journal of Geochemical Exploration, 2004. **84**(2): p. 65-76.
32. Steger, H., *Oxidation of sulfide minerals: VII. Effect of temperature and relative humidity on the oxidation of pyrrhotite.* Chemical Geology, 1982. **35**(3-4): p. 281-295.
33. Buckley, A. and R. Woods, *X-ray photoelectron spectroscopy of oxidised pyrrhotite surfaces.* Applications of Surface Science, 1985. **20**(4): p. 472-480.
34. Pratt, A.R., I.J. Muir, and H.W. Nesbitt, *X-ray photoelectron and Auger electron spectroscopic studies of pyrrhotite and mechanism of air oxidation.* Geochimica et Cosmochimica Acta, 1994. **58**(2): p. 827-841.
35. Pratt, A. and H. Nesbitt, *Generation of acids from mine waste: Oxidative leaching of pyrrhotite in dilute H_2SO_4 solutions at pH 3.0.* Geochimica et Cosmochimica Acta, 1994. **58**(23): p. 5147-5159.
36. Mycroft, J.R., H.W. Nesbitt, and A.R. Pratt, *X-ray photoelectron and Auger electron spectroscopy of air-oxidized pyrrhotite: Distribution of oxidized species with depth.* Geochimica et Cosmochimica Acta, 1995. **59**(4): p. 721-733.
37. Smart, R.S.C., et al., *SIMS studies of oxidation mechanisms and polysulfide formation in reacted sulfide surfaces.* Minerals Engineering, 2000. **13**(8-9): p. 857-870.
38. Ekmekçi, Z., et al., *The relationship between the electrochemical, mineralogical and flotation characteristics of pyrrhotite samples from different Ni Ores.* Journal of Electroanalytical Chemistry, 2010. **647**(2): p. 133-143.
39. Ekmekçi, Z., et al., *An impedance study of the adsorption of $CuSO_4$ and SIBX on pyrrhotite samples of different provenances.* Minerals Engineering, 2010. **23**(11-13): p. 903-907.
40. Janzen, M.P., R.V. Nicholson, and J.M. Scharer, *Pyrrhotite reaction kinetics: reaction rates for oxidation by oxygen, ferric iron, and for nonoxidative dissolution.* Geochimica et Cosmochimica Acta, 2000. **64**(9): p. 1511-1522.
41. Kwong, Y.-T.J., *Prediction and prevention of acid rock drainage from a geological and mineralogical perspective*. 1993: MEND.
42. Bozkurt, V., Z. Xu, and J. Finch, *Effect of depressants on xanthate adsorption on pentlandite and pyrrhotite: single vs mixed minerals.* Canadian metallurgical quarterly, 1999. **38**(2): p. 105-112.

43. Adam, K., K. Natarajan, and I. Iwasaki, *Grinding media wear and its effect on the flotation of sulfide minerals.* International journal of mineral processing, 1984. **12**(1-3): p. 39-54.
44. Cheng, X. and I. Iwasaki, *Effect of chalcopyrite and pyrrhotite interaction on flotation separation.* Mining, Metallurgy & Exploration, 1992. **9**(2): p. 73-79.
45. Nakazawa, H. and I. Iwasaki, *Effect of pyrite-pyrrhotite contact on their floatabilities.* Mining, Metallurgy & Exploration, 1985. **2**(4): p. 206-211.
46. Nakazawa, H. and I. Iwasaki, *Galvanic contact between nickel arsenide and pyrrhotite and its effect on flotation.* International journal of mineral processing, 1986. **18**(3-4): p. 203-215.
47. Pozzo, R., A. Malicsi, and I. Iwasaki, *Pyrite-pyrrhotite-grinding media contact and its effect on flotation.* Mining, Metallurgy & Exploration, 1990. **7**(1): p. 16-21.
48. Becker, M., J. De Villiers, and D. Bradshaw. *Evaluation of pyrrhotite from selected Ni and platinum group element (PGE) ore deposits and the influence of its mineralogy on flotation performance*. 2008. Australasian Institute of Mining and Metallurgy.
49. Buckley, A. and K. Riley, *Self-induced floatability of sulphide minerals: Examination of recent evidence for elemental sulphur as the hydrophobic entity.* Surface and interface analysis, 1991. **17**(9): p. 655-659.
50. Buckley, A. and R. Woods, *Relaxation of the lead-deficient sulfide surface layer on oxidized galena.* Journal of applied electrochemistry, 1996. **26**(9): p. 899-907.
51. Finkelstein, N. and G. Poling. *The role of dithiolates in the flotation of sulphide minerals*. 1977. Mintek.
52. Hayes, R., et al., *Collectorless flotation of sulphide minerals.* Mineral Procesing and Extractive Metallurgy Review, 1987. **2**(3): p. 203-234.
53. Hodgson, M. and G. Agar, *Electrochemical investigations into the flotation chemistry of pentlandite and pyrrhotite: Process water and xanthate interactions.* Canadian Metallurgical Quarterly, 1989. **28**(3): p. 189-198.
54. Fornasiero, D., M. Montalti, and J. Ralston, *Kinetics of adsorption of ethyl xanthate on pyrrhotite: in situ UV and infrared spectroscopic studies.* Journal of Colloid and Interface Science, 1995. **172**(2): p. 467-478.
55. Kelebek, S., B. Nanthakumar, and P.D. Katsabanis, *Oxidation of complex Ni-Cu sulphide ores and its implication for flotation practice.* Canadian Metallurgical Quarterly, 2007. **46**(3): p. 279-284.
56. Rao, S.R. and J.A. Finch, *Adsorption of amyl xanthate at pyrrhotite in the presence of nitrogen and implications in flotation.* Canadian Metallurgical Quarterly, 1991. **30**(1): p. 1-6.
57. Kolahdoozan, M., *Adsorption and flotation characteristics of hexagonal and monoclinic pyrrhotite*. 1996.

58. Xu, M. and S. Wilson, *Investigation of seasonal metallurgical shift at INCO's clarabelle mill.* Minerals engineering, 2000. **13**(12): p. 1207-1218.
59. Yoon, R.H., et al., *A study of the pyrrhotite depression mechanism by diethylenetriamine.* Minerals Engineering, 1995. **8**(7): p. 807-816.
60. Allison, S. and C. O'Connor, *An investigation into the flotation behaviour of pyrrhotite.* International Journal of Mineral Processing, 2011. **98**(3-4): p. 202-207.
61. Gerson, A.R., *The effect of surface oxidation on the Cu activation of pentlandite and pyrrhotite*. 2008, Science Press.
62. Acar, S. and P. Somasundaran, *Effect of dissolved mineral species on the electrokinetic behaviour of sulfides.* Minerals engineering, 1992. **5**(1): p. 27-40.
63. Multani, R.S., et al., *The effect of superstructure on the zeta potential, xanthate adsorption, and flotation response of pyrrhotite.* Colloids and Surfaces A: Physicochemical and Engineering Aspects, 2018. **551**: p. 108-116.
64. Buckley, A.N. and R. Woods, *Surface composition of pentlandite under flotation-related conditions.* Surface and Interface Analysis, 1991. **17**(9): p. 675-680.
65. Legrand, D.L., G.M. Bancroft, and H.W. Nesbitt, *Surface characterization of pentlandite, $(Fe,Ni)_9S_8$, by X-ray photoelectron spectroscopy.* International Journal of Mineral Processing, 1997. **51**(1-4): p. 217-228.
66. Richardson, S. and D. Vaughan, *Surface alteration of pentlandite and spectroscopic evidence for secondary violarite formation.* Mineralogical magazine, 1989. **53**(370): p. 213-222.
67. Marape, G. and M. Vermaak, *Fundamentals of pentlandite mineralogy and its effect on its electrochemical behaviour.* Minerals Engineering, 2012. **32**: p. 60-67.
68. Thornber, M., *Mineralogical and electrochemical stability of the nickel-iron sulphides—pentlandite and violarite.* Journal of Applied Electrochemistry, 1983. **13**(2): p. 253-267.
69. Rajamani, V. and C. Prewitt, *Crystal chemistry of natural pentlandites.* The Canadian Mineralogist, 1973. **12**(3): p. 178-187.
70. Pearson, A.D. and M. Buerger, *Confirmation of the crystal structure of pentlandite*. 1956, Mineralogical Society of America.
71. Etschmann, B., et al., *A kinetic study of the exsolution of pentlandite $(Ni,Fe)_9S_8$ from the monosulfide solid solution (Fe,Ni)S.* American Mineralogist, 2004. **89**(1): p. 39-50.
72. Tenailleau, C., et al., *A neutron powder diffraction study of Fe and Ni distributions in synthetic pentlandite and violarite using ^{60}Ni isotope.* American Mineralogist, 2006. **91**(8-9): p. 1442-1447.
73. Knop, O., C.-H. Huang, and F. Woodhams, *Chalcogenides of the transition elements. VII. A Mössbauer study of pentlandite.* American Mineralogist: Journal of Earth and Planetary Materials, 1970. **55**(7-8): p. 1115-1130.

74. Legrand, D., G. Bancroft, and H. Nesbitt, *Oxidation/alteration of pentlandite and pyrrhotite surfaces at pH 9.3: Part 1. Assignment of XPS spectra and chemical trends.* American mineralogist, 2005. **90**(7): p. 1042-1054.
75. Bozkurt, V., Z. Xu, and J. Finch, *Pentlandite/pyrrhotite interaction and xanthate adsorption.* International journal of mineral processing, 1998. **52**(4): p. 203-214.
76. Gebhardt, J. and P. Richardson, *Differential flotation of a chalcocite-pyrite particle bed by electrochemical control.* Mining, Metallurgy & Exploration, 1987. **4**(3): p. 140-145.
77. Rao, M.Y. and K. Natarajan, *Electrochemical effects of mineral-mineral interactions on the flotation of chalcopyrite and sphalerite.* International Journal of Mineral Processing, 1989. **27**(3-4): p. 279-293.
78. Rao, M.Y. and K. Natarajan, *Effect of electrochemical interactions among sulphide minerals and grinding medium on the flotation of sphalerite and galena.* International Journal of Mineral Processing, 1990. **29**(3-4): p. 175-194.
79. Rao, S.R. and J. Finch, *Galvanic interaction studies on sulphide minerals.* Canadian Metallurgical Quarterly, 1988. **27**(4): p. 253-259.
80. Khan, A. and S. Kelebek, *Electrochemical aspects of pyrrhotite and pentlandite in relation to their flotation with xanthate. Part-I: cyclic voltammetry and rest potential measurements.* Journal of Applied Electrochemistry, 2004. **34**(8): p. 849-856.
81. Kelebek, S. and C. Tukel, *The effect of sodium metabisulfite and triethylenetetramine system on pentlandite–pyrrhotite separation.* International journal of mineral processing, 1999. **57**(2): p. 135-152.
82. Manouchehri, H., *Pyrrhotite flotation and its selectivity against pentlandite in the beneficiation of nickeliferous ores: An electrochemistry perspective.* Minerals & Metallurgical Processing, 2014. **31**(2): p. 115-125.
83. Tukel, C. and S. Kelebek, *Modulation of xanthate action by sulphite ions in pyrrhotite deactivation/depression.* International Journal of Mineral Processing, 2010. **95**(1-4): p. 47-52.
84. Kelebek, S., P. Wells, and S. Fekete, *Differential flotation of chalcopyrite, pentlandite and pyrrhotite in Ni-Cu sulphide ores.* Canadian metallurgical quarterly, 1996. **35**(4): p. 329-336.
85. Multani, R.S. and K.E. Waters, *Pyrrhotite depression studies with DETA and SMBS on a Ni-Cu sulphide ore.* The Canadian Journal of Chemical Engineering, 2019. **97**(7): p. 2121-2130.
86. Wiese, J.G., *Investigating depressant behaviour in the flotation of selected Merensky ores*. 2009, University of Cape Town.
87. Bulatovic, S.M., *Handbook of flotation reagents: chemistry, theory and practice: Volume 1: flotation of sulfide ores*. 2007: Elsevier.

88. Prestidge, C.A., J. Ralston, and R.S.C. Smart, *The competitive adsorption of cyanide and ethyl xanthate on pyrite and pyrrhotite surfaces.* International journal of mineral processing, 1993. **38**(3-4): p. 205-233.
89. Lawson, V., et al. *Improving pentlandite pyrrhotite separation at INCO's Clarabelle Mill*. in *Centenary of Flotation Symposium. AusIMM, Brisbane*. 2005.
90. Bobicki, E.R., C.E. Gison, and J.-F. Boulanger, *Canadian Milling Practice*. 2020 ed. 2020. 318.
91. Manouchehri, H.R., *Pyrrhotite flotation and its selectivity against pentlandite in the beneficiation of nickeliferous ores: an electrochemistry perspective.* Mining, Metallurgy & Exploration, 2014. **31**(2): p. 115-125.
92. Kelebek, S. *The effect of oxidation on the flotation behaviour of nickel–copper ores*. in *XVIII Mineral Processing Congress. Sydney*. 1993.
93. Agar, G.E., *Flotation of chalcopyrite, pentlandite, pyrrhotite ores.* International Journal of Mineral Processing, 1991. **33**(1-4): p. 1-19.
94. Lotter, N., et al., *Modern process mineralogy: two case studies.* Minerals Engineering, 2011. **24**(7): p. 638-650.
95. Multani, R.S. and K.E. Waters, *A review of the physicochemical properties and flotation of pyrrhotite superstructures (4C-Fe_7S_8/5C-Fe_9S_{10}) in Ni-Cu sulphide mineral processing.* The Canadian Journal of Chemical Engineering, 2018. **96**(5): p. 1185-1206.
96. Powell, A.V., et al., *Structure and magnetism in synthetic pyrrhotite Fe_7S_8: A powder neutron-diffraction study.* Physical Review B, 2004. **70**(1): p. 014415.
97. Néel, L., *Some new results on antiferromagnetism and ferromagnetism.* Reviews of Modern Physics, 1953. **25**(1): p. 58.
98. Becker, M., *The mineralogy and crystallography of pyrrhotite from selected nickel and PGE ore deposits and its effect on flotation performance*. 2010, University of Pretoria.
99. Yoon, R.-H., et al., *A study of the pyrrhotite depression mechanism by diethylenetriamine.* Minerals Engineering, 1995. **8**(7): p. 807-816.
100. Chen, W., et al., *Investigations on flotation separation of scheelite from calcite by using a novel depressant: sodium phytate.* Minerals Engineering, 2018. **126**: p. 116-122.
101. Glencore, *Annual Report 2017*. 2018, Glencore. p. 73.
102. Multani, R.S. and C. Deredin, *Pyrrhotite rejection at the strathcona mill*, in *Canadian Mineral Processors' Conference*. 2018: Ottawa, Canada. p. 225-237.
103. Legrand, D., G. Bancroft, and H. Nesbitt, *Oxidation of pentlandite and pyrrhotite surfaces at pH 9.3: Part 2. Effect of xanthates and dissolved oxygen.* American mineralogist, 2005. **90**(7): p. 1055-1061.

104. Buswell, A. and M. Nicol, *Some aspects of the electrochemistry of the flotation of pyrrhotite.* Journal of applied electrochemistry, 2002. **32**(12): p. 1321-1329.
105. Smart, R.S., et al., *Surface analytical studies of oxidation and collector adsorption in sulfide mineral flotation*, in *Solid—Liquid Interfaces*. 2003, Springer. p. 3-62.
106. Jeldres, R.I., L. Forbes, and L.A. Cisternas, *Effect of seawater on sulfide ore flotation: A review.* Mineral Processing and Extractive Metallurgy Review, 2016. **37**(6): p. 369-384.
107. Wills, B.A. and J. Finch, *Wills' mineral processing technology: an introduction to the practical aspects of ore treatment and mineral recovery*. 2015: Butterworth-Heinemann.
108. Mikhlin, Y.L., et al., *Electronic structure of the non-equilibrium iron-deficient layer of hexagonal pyrrhotite.* Applied Surface Science, 1998. **125**(1): p. 73-84.
109. Tao, H., et al., *Descriptor of catalytic activity of metal sulfides for oxygen reduction reaction: a potential indicator for mineral flotation.* Journal of Materials Chemistry A, 2018. **6**(20): p. 9650-9656.
110. Kulkarni, A., et al., *Understanding catalytic activity trends in the oxygen reduction reaction.* Chemical Reviews, 2018. **118**(5): p. 2302-2312.
111. Jiao, Y., et al., *Design of electrocatalysts for oxygen-and hydrogen-involving energy conversion reactions.* Chemical Society Reviews, 2015. **44**(8): p. 2060-2086.
112. Liu, F., et al., *Thermal upgrading of nickeliferous pyrrhotite tailings: formation mechanism of ferronickel alloy.* Minerals Engineering, 2019. **134**: p. 206-214.
113. Elliot, A.D., *Structure of pyrrhotite 5C (Fe_9S_{10}).* Acta Crystallographica Section B: Structural Science, 2010. **66**(3): p. 271-279.
114. Liles, D.C. and J.P. de Villiers, *Redetermination of the structure of 5C pyrrhotite at low temperature and at room temperature.* American Mineralogist, 2012. **97**(2-3): p. 257-261.
115. Becker, M., J. De Villiers, and D. Bradshaw, *The flotation of magnetic and non-magnetic pyrrhotite from selected nickel ore deposits.* Minerals Engineering, 2010. **23**(11-13): p. 1045-1052.
116. Legrand, D.L., *Oxidation/alteration of pentlandite and pyrrhotite surfaces at pH 9.3: Part 1. Assignment of XPS spectra and chemical trends.* American Mineralogist, 2005. **90**(7): p. 1042-1054.
117. Mikhlin, Y., et al., *Hard X-ray photoelectron and X-ray absorption spectroscopy characterization of oxidized surfaces of iron sulfides.* Applied Surface Science, 2016. **387**: p. 796-804.
118. Mikhlin, Y., et al., *Layered structure of the near-surface region of oxidized chalcopyrite ($CuFeS_2$): hard X-ray photoelectron spectroscopy, X-ray absorption*

spectroscopy and DFT+ U studies. Physical Chemistry Chemical Physics, 2017. **19**(4): p. 2749-2759.
119. Powell, A.V., et al., *Structure and magnetism in synthetic pyrrhotite Fe_7S_8: A powder neutron-diffraction study.* Physical Review B, 2004. **70**(1): p. 014415.
120. Morimoto, N., et al., *Crystallography and stability of pyrrhotites.* Economic Geology, 1975. **70**(4): p. 824-833.
121. Morimoto, N., et al., *Superstructure and nonstoichiometry of intermediate pyrrhotite.* American Mineralogist: Journal of Earth and Planetary Materials, 1975. **60**(3-4): p. 240-248.
122. Clark, S.J., et al., *First principles methods using CASTEP.* Zeitschrift für Kristallographie-Crystalline Materials, 2005. **220**(5/6): p. 567-570.
123. Segall, M., et al., *First-principles simulation: ideas, illustrations and the CASTEP code.* Journal of Physics: Condensed Matter, 2002. **14**(11): p. 2717.
124. Perdew, J.P., K. Burke, and M. Ernzerhof, *Generalized gradient approximation made simple.* Physical review letters, 1996. **77**(18): p. 3865.
125. Anisimov, V.I., et al., *Density-functional theory and NiO photoemission spectra.* Physical Review B, 1993. **48**(23): p. 16929.
126. Hubbard, J., *Electron correlations in narrow energy bands.* Proc. R. Soc. Lond. A, 1963. **276**(1365): p. 238-257.
127. Ricci, F. and E. Bousquet, *Unveiling the room-temperature magnetoelectricity of troilite FeS.* Physical Review Letters, 2016. **116**(22): p. 227601.
128. Roberts, D.M., et al., *Nanocrystalline iron monosulfides near stoichiometry.* Scientific Reports, 2018. **8**.
129. Rohrbach, A., J. Hafner, and G. Kresse, *Electronic correlation effects in transition-metal sulfides.* Journal of Physics: Condensed Matter, 2003. **15**(6): p. 979.
130. Zhang, Y., et al., *Effect of surface stoichiometry on the band gap of the pyrite FeS_2(100) surface.* Physical Review B, 2012. **85**(8): p. 085314.
131. Legrand, D.L., *Oxidation of pentlandite and pyrrhotite surfaces at pH 9.3: Part 2. Effect of xanthates and dissolved oxygen.* American Mineralogist, 2005. **90**(7): p. 1055-1061.
132. Biesinger, M.C., et al., *Resolving surface chemical states in XPS analysis of first row transition metals, oxides and hydroxides: Cr, Mn, Fe, Co and Ni.* Applied Surface Science, 2011. **257**(7): p. 2717-2730.
133. Knipe, S., et al., *X-ray photoelectron spectroscopic study of water adsorption on iron sulphide minerals.* Geochimica et Cosmochimica Acta, 1995. **59**(6): p. 1079-1090.
134. Moulder, J., et al., *Handbook of X-ray photoelectron spectroscopy.* Perkin-Elmer Corporation, 1992. p. 128.

135. Scofield, J.H., *Hartree-Slater subshell photoionization cross-sections at 1254 and 1487 eV.* Journal of Electron Spectroscopy and Related Phenomena, 1976. **8**(2): p. 129-137.
136. Mikhlin, Y. and Y. Tomashevich, *Pristine and reacted surfaces of pyrrhotite and arsenopyrite as studied by X-ray absorption near-edge structure spectroscopy.* Physics and Chemistry of Minerals, 2005. **32**(1): p. 19-27.
137. Smart, R.S., et al., *SIMS studies of oxidation mechanisms and polysulfide formation in reacted sulfide surfaces.* Minerals Engineering, 2000. **13**(8-9): p. 857-870.
138. Ignatova, V., et al., *Depth profiling of $ZrO_2/SiO_2/Si$ stacks—a TOF-SIMS and computer simulation study.* Applied Surface Science, 2004. **231**: p. 603-608.
139. Ignatova, V., et al., *Interpretation of TOF–SIMS depth profiles from ultrashallow high-k dielectric stacks assisted by hybrid collisional computer simulation.* Applied Physics A, 2005. **81**(1): p. 71-77.
140. Hammer, B. and J. Norskov, *Why gold is the noblest of all the metals.* Nature, 1995. **376**(6537): p. 238.
141. Nørskov, J., *Electronic factors in catalysis.* Progress in Surface Science, 1991. **38**(2): p. 103-144.
142. Becker, U. and M.F. Hochella Jr, *The calculation of STM images, STS spectra, and XPS peak shifts for galena: new tools for understanding mineral surface chemistry.* Geochimica et Cosmochimica Acta, 1996. **60**(13): p. 2413-2426.
143. Harries, D., K. Pollok, and F. Langenhorst, *Oxidative dissolution of 4C-and NC-pyrrhotite: intrinsic reactivity differences, pH dependence, and the effect of anisotropy.* Geochimica et Cosmochimica Acta, 2013. **102**: p. 23-44.
144. Kuklinskii, A., et al., *Conditions for the formation of a nonequilibrium nonstoichiometric layer on pyrrhotite in acid solutions.* Russian Journal of Electrochemistry, 2001. **37**(12): p. 1269-1276.
145. Hamilton, I. and R. Woods, *An investigation of surface oxidation of pyrite and pyrrhotite by linear potential sweep voltammetry.* Journal of Electroanalytical Chemistry and Interfacial Electrochemistry, 1981. **118**: p. 327-343.
146. Acres, R.G., S.L. Harmer, and D.A. Beattie, *Synchrotron PEEM and ToF-SIMS study of oxidized heterogeneous pentlandite, pyrrhotite and chalcopyrite.* Journal of Synchrotron Radiation, 2010. **17**(5): p. 606-615.
147. Graham, A., *Quantitative determination of hexagonal and monoclinic pyrrhotites by X-ray diffraction.* The Canadian Mineralogist, 1969. **10**(1): p. 4-24.
148. Li, G., et al., *In-situ XRD and EDS method study on the oxidation behaviour of Ni-Cu sulphide ore.* Scientific reports, 2017. **7**(1): p. 3212-3212.
149. Richardson, S. and D.J. Vaughan, *Surface alteration of pentlandite and spectroscopic evidence for secondary violarite formation.* Mineralogical Magazine, 1989. **53**(370): p. 213-222.

150. Pratt, A.R., H.W. Nesbitt, and I.J. muir, *Generation of acids from mine waste: oxidative leaching of pyrrhotite in dilute H_2SO_4 solutions at pH 3.0.* Geochimica et Cosmochimica Acta, 1994. **58**(23): p. 5147-5159.
151. DeWitt, C.C. and E.E. Roper, *The surface relations of potassium ethyl xanthate and pine oil. I.* Journal of the American Chemical Society, 1932. **54**(2): p. 444-455.
152. Kresse, G. and J. Hafner, *Ab initio molecular dynamics for liquid metals.* Physical Review B, 1993. **47**(1): p. 558-561.
153. Kresse, G. and J. Hafner, *Ab initio molecular-dynamics simulation of the liquid-metal–amorphous-semiconductor transition in germanium.* Physical Review B, 1994. **49**(20): p. 14251-14269.
154. Kresse, G. and D. Joubert, *From ultrasoft pseudopotentials to the projector augmented-wave method.* Physical Review B, 1999. **59**(3): p. 1758-1775.
155. Perdew, J.P., K. Burke, and M. Ernzerhof, *Generalized Gradient Approximation Made Simple.* Physical Review Letters, 1996. **77**(18): p. 3865-3868.
156. Powell, A.V., et al., *Structure and magnetism in synthetic pyrrhotite Fe_7S_8: A powder neutron-diffraction study.* Physical Review B, 2004. **70**(1).
157. Roldan, A. and N.H. de Leeuw, *A density functional theory study of the hydrogenation and reduction of the thio-spinel Fe_3S_4{111} surface.* Physical Chemistry Chemical Physics, 2019. **21**(5): p. 2426-2433.
158. Lu, L. and S. Yu, *Metal distribution in iron-nickel sulfide mineral pentlandite: first-principles study.* Chemical Physics Letters, 2019. **736**: p. 136786.
159. Dudarev, S.L., et al., *Electron-energy-loss spectra and the structural stability of nickel oxide: an LSDA+U study.* Physical Review B, 1998. **57**(3): p. 1505-1509.
160. Anisimov, V.I., et al., *Spin bags, polarons, and impurity potentials in $La_{2-x}Sr_xCuO_4$ from first principles.* Physical Review Letters, 1992. **68**(3): p. 345-348.
161. Cococcioni, M. and S. De Gironcoli, *Linear response approach to the calculation of the effective interaction parameters in the LDA+ U method.* Physical Review B, 2005. **71**(3): p. 035105.
162. Limas, N.G. and T.A. Manz, *Introducing DDEC6 atomic population analysis: part 2. Computed results for a wide range of periodic and nonperiodic materials.* RSC Advances, 2016. **6**(51): p. 45727-45747.
163. Manz, T.A. and N.G. Limas, *Introducing DDEC6 atomic population analysis: part 1. Charge partitioning theory and methodology.* RSC Advances, 2016. **6**(53): p. 47771-47801.
164. Stern, M., *Closure to "Discussion of 'electrochemical polarization, 1. A theoretical analysis of the shape of polarization curves' [M. Stern and A. L. Geary (pp. 56–63, Vol. 104)]".* Journal of the Electrochemical Society, 1957. **104**(12): p. 751.

165. Turcio-Ortega, D., et al., *Reactivity of Fe/FeS nanoparticles: electrolyte composition effects on corrosion electrochemistry.* Environmental Science & Technology, 2012. **46**(22): p. 12484-12492.
166. Schaible, M.J., et al., *Characterization and simulation of natural pyrite surfaces: a combined experimental and theoretical study.* The Journal of Physical Chemistry C, 2019. **123**(43): p. 26397-26405.
167. Kelly, R., *An attempt to understand preferential sputtering.* Nuclear Instruments and Methods, 1978. **149**(1-3): p. 553-558.
168. Benito, N. and C. Palacio, *Nanostructuring of Ta_2O_5 surfaces by low energy Ar^+ bombardment.* Applied Surface Science, 2015. **351**: p. 753-759.
169. Briggs, D., *Practical Surface analysis second edition Vol. 1, Auger and X-ray photoelectron spectroscopy.* John Wiley & Sons Ltd., New York, 1990.
170. Carlson, T., *Photoelectron and Auger spectroscopy*. 2013: Springer Science & Business Media.
171. Pettifer, Z.E., et al., *New interpretation and approach to curve fitting synchrotron X-ray photoelectron spectra of $(Fe,Ni)_9S_8$ fracture surfaces.* Applied Surface Science, 2020. **504**: p. 144458.
172. Nesbitt, H.W., et al., *XPS measurement of fivefold and sixfold coordinated sulfur in pyrrhotites and evidence for millerite and pyrrhotite surface species.* American Mineralogist, 2001. **86**(3): p. 318-326.
173. Laajalehto, K., et al. *Investigation of copper sulfide surfaces using synchrotron radiation excited photoemission spectroscopy*. in *European Conference on Applications of Surface and Interface Analysis ECASIA*. 1996.
174. Qi, C., et al., *The role of Cu ion activation and surface oxidation for polymorphic pyrrhotite flotation performance in Strathcona Mill.* Minerals Engineering, 2019. **134**: p. 87-96.
175. Sit, P.H.L., M.H. Cohen, and A. Selloni, *Interaction of oxygen and water with the (100) surface of pyrite: mechanism of sulfur oxidation.* The Journal of Physical Chemistry Letters, 2012. **3**(17): p. 2409-2414.
176. Senior, G.D. and W.J. Trahar, *The influence of metal hydroxides and collector on the flotation of chalcopyrite.* International Journal of Mineral Processing, 1991. **33**(1-4): p. 321-341.
177. Leppinen, J.O., *FTIR and flotation investigation of the adsorption of ethyl xanthate on activated and non-activated sulfide minerals.* International Journal of Mineral Processing, 1990. **30**(3-4): p. 245-263.
178. Senior, G.D., W.J. Trahar, and P.J. Guy, *The selective flotation of pentlandite from a nickel ore.* International Journal of Mineral Processing, 1995. **43**(3-4): p. 209-234.

179. Wiese, J., et al., *Interpreting the role of reagents in the flotation of platinum-bearing Merensky ores.* Journal of the Southern African Institute of Mining and Metallurgy, 2007. **107**(1): p. 29-36.
180. Allison, S.A. and C.T. O'Connor, *An investigation into the flotation behaviour of pyrrhotite.* International Journal of Mineral Processing, 2011. **98**(3-4): p. 202-207.
181. Multani, R.S. and K.E. Waters, *A review of the physicochemical properties and flotation of pyrrhotite superstructures (4C-Fe_7S_8/5C-Fe_9S_{10}) in Ni-Cu sulphide mineral processing.* The Canadian Journal of Chemical Engineering, 2018. **96**(5): p. 1185-1206.
182. Barzyk, W., K. Malysa, and A. Pomianowski, *The influence of surface oxidation of chalcocite on its floatability and ethyl xanthate sorption.* International Journal of Mineral Processing, 1981. **8**(1): p. 17-29.
183. Newell, A.J.H., W.M. Skinner, and D.J. Bradshaw, *Restoring the floatability of oxidised sulfides using sulfidisation.* International Journal of Mineral Processing, 2007. **84**(1-4): p. 108-117.
184. Niu, X., et al., *Correlation of surface oxidation with xanthate adsorption and pyrite flotation.* Applied Surface Science, 2019. **495**: p. 143411.
185. Szczypa, J., J. Solecki, and A. Komosa, *Effect of surface oxidation and iron contents on xanthate ions adsorption of synthetic sphalerites.* International Journal of Mineral Processing, 1980. **7**(2): p. 151-157.
186. Cabrera-German, D., et al., *Assessing the chemical state of chemically deposited copper sulfide: a quantitative analysis of the X-ray photoelectron spectra of the amorphous-to-covellite transition phases.* Applied Surface Science, 2019. **481**: p. 281-295.
187. Sanchez-Portal, D., E. Artacho, and J.M. Soler, *Projection of plane-wave calculations into atomic orbitals.* Solid State Communications, 1995. **95**(10): p. 685-690.
188. Schaufuß, A.G., et al., *Reactivity of surface chemical states on fractured pyrite.* Surface Science, 1998. **411**(3): p. 321-328.
189. Mikhlin, Y., *Reactivity of pyrrhotite surfaces: an electrochemical study.* Physical Chemistry Chemical Physics, 2000. **2**(24): p. 5672-5677.
190. Baryshev, S.V. and E. Thimsen, *Enthalpy of formation for Cu–Zn–Sn–S (CZTS) calculated from surface binding energies experimentally measured by ion sputtering.* Chemistry of Materials, 2015. **27**(7): p. 2294-2298.
191. Borrajo-Pelaez, R., F. Saiz, and M. Gamero-Castaño, *The effect of the molecular mass on the sputtering of Si, SiC, Ge, and GaAs by electrosprayed nanodroplets at impact velocities up to 17 km/s.* Aerosol Science and Technology, 2015. **49**(4): p. 256-266.

192. Henkel, H., *Standard diagrams of magnetic properties and density—a tool for understanding magnetic petrology.* Journal of Applied Geophysics, 1994. **32**(1): p. 43-53.
193. Fujii, K., et al., *Absolute measurement of the density of silicon crystals in vacuo for a determination of the Avogadro constant.* IEEE Transactions on Instrumentation and Measurement, 1995. **44**(2): p. 542-545.
194. Qiu, Z., et al., *Separation of pyrite from chalcopyrite and molybdenite by using selective collector of N-isopropoxypropyl-N'-ethoxycarbonyl thiourea in high salinity water.* Minerals Engineering, 2017. **100**: p. 93-98.
195. Lide, D.R., *CRC handbook of chemistry and physics*. Vol. 85. 2004: CRC press.
196. Chauke, H.R., et al., *Electronic structure and stability of the pentlandites Co_9S_8 and $(Fe,Ni)_9S_8$.* Physical Review B, 2002. **66**(15).
197. Borrajo-Pelaez, R., F. Saiz, and M. Gamero-Castaño, *The effect of the molecular mass on the sputtering of Si, SiC, Ge, and GaAs by electrosprayed nanodroplets at impact velocities up to 17 km/s.* Aerosol Science and Technology, 2015. **49**(4): p. 256-266.
198. Francis, A., et al., *Computation of the cohesive energies of NaCl, SiO_2 and Al using density functional theory.* Physical Science International Journal, 2016. **11**(3): p. 1-9.
199. Maezono, R., et al., *Quantum Monte Carlo study of sodium.* Physical Review B, 2003. **68**(16).
200. Awadallah, S., *Protein antioxidants in thalassemia*, in *Advances in Clinical Chemistry*. 2013. **60**: p. 85-128.
201. Gil-Lozano, C., et al., *Quantifying Fenton reaction pathways driven by self-generated H_2O_2 on pyrite surfaces.* Scientific Reports, 2017. **7**: p. 43703-43703.

Appendix A. Supporting Information: Unraveling Polymorphic Pyrrhotite Electrochemical Oxidation by Underlying Electronic Structures

A.1. DFT Simulation

There are major computational challenges when it comes to using DFT simulations to study pyrrhotite. First, there is great uncertainty regarding the crystal structure of defective FeS systems, particularly in the case of 5C-hexagonal pyrrhotite. The second major challenge is the size of the unit cells. Again, the 5C-hexagonal pyrrhotite is the major challenge as its unit cell is very big in the scale of DFT simulations. This means that pyrrhotite structures studied here contain many electrons, which demand a considerable computational cost. The third challenge is that FeS compounds exhibit strong electron correlation due to the presence of iron. This correlation makes the conventional DFT method inaccurate for these components and necessitates a computational method that can reasonably capture the effects of strong electron correlation. This method should also be computationally feasible for large periodic systems such as pyrrhotite. The DFT simulation parameters should be carefully chosen to perform the time-consuming DFT simulation with high certainty and minimal need for repeating.

A.1.1. Geometry Optimization

The optimum value of U in the DFT+U method was determined by comparing the lowest energy structures with the experimentally measured unit cell. For this purpose, a series of geometry optimization simulations were performed for both 4C-monoclinic and 5C-hexagonal pyrrhotite using different U values. The value of U=1.8 eV gave the best agreement between the calculated and experimentally measured unit cell volumes (Figure A-1).

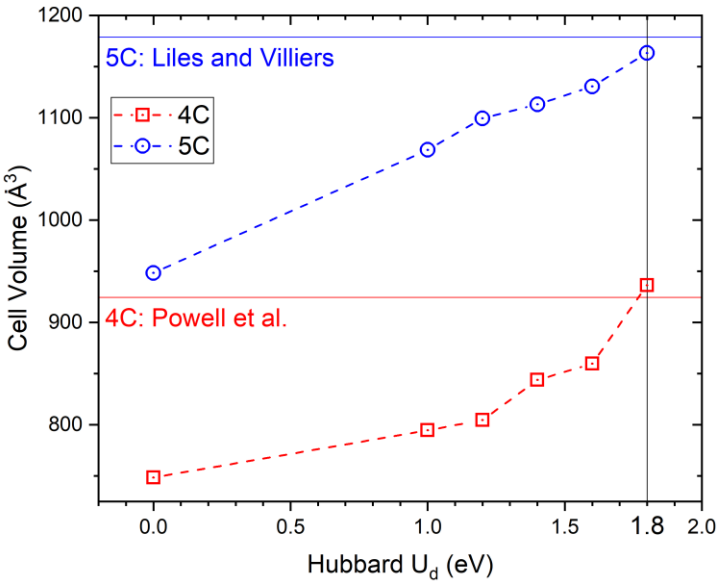

Figure A-1. The relationship between U term in DFT+U calculations and cell volumes of 4C-monoclinic and 5C-hexagonal pyrrhotite. The horizontal straight lines show the corresponding experimental values (4C [119] and 5C [114]).[10]

As mentioned in the simulation details in Chapter 4, the U = 1.8 eV was used to obtain the optimized unit cell structures of 4C-monoclinic and 5C-hexagonal pyrrhotite. The ferrimagnetic (4C) and anti-ferromagnetic (5C) spin configurations were assigned according to the atomic magnetic moment structure proposed by Wang and Salveson [5]. The monoclinic unit cell with C2/c symmetry [119] is well compatible with the ferrimagnetic structure of 4C-monoclinic pyrrhotite. However, we could not represent the anti-ferromagnetic structure of 5C-hexagonal pyrrhotite in any of the proposed symmetries. Thus, the 5C-hexagonal unit cell was modeled in the P1 symmetry. The total magnetic moment of the 4C-monoclinic pyrrhotite optimized unit cell was 3.92 μ_B which is in a

[10] This simulation work was carried out by Mohammad Khalkhali.

good agreement with the experimentally measured value of 3.16 μ_B [119]. Table A-1 dimensions of the optimized unit cells.

Table A-1. The optimized crystal structures of 4C-monoclinic and 5C-hexagonal pyrrhotite calculated using U=1.8 eV.[11]

		a (Å)	b (Å)	c (Å)	α (°)	β (°)	γ (°)	V (Å^3)
4C	Calc.	11.87	6.92	12.92	90	118.02	90	936.40
(C2/c)	Exp. [119]	11.87	6.85	12.90	90	118.075	90	924.58
5C	Calc.*	6.89	28.55	6.83	89.55	119.98	89.91	1163.37
	Exp. [114]	6.89	28.63	6.89	90	120	90	1178.27

A.1.2. Electronic Structure

Figure A-2a and Figure A-2b show the band structure for 4C-monoclinic and 5C-hexagonal pyrrhotite. Note that the band structure of the 5C-hexagonal pyrrhotite is denser due to more atoms in its unit cell.

For metallic components, its atomic chemical activity is also related to the amount of the available states near the Fermi level. To further analyze the electronic structure difference, we performed population analyses to calculate partial atomic charges. As CASTEP applies the plane-wave pseudopotential method, electrons localizations in the system are calculated via projecting the PW states onto a localized basis as explained by Sanchez-

[11] To be able to model the 5C pyrrhotite with the spin configurations mentioned, the crystal should be modeled in P1 symmetry. This simulation work was carried out by Mohammad Khalkhali.

Portal et al. [187]. As Figure A-2c and Figure A-2d show, both Hirshfeld and Mulliken population analyses confirmed that iron atoms are more positively charged in the 4C pyrrhotite.

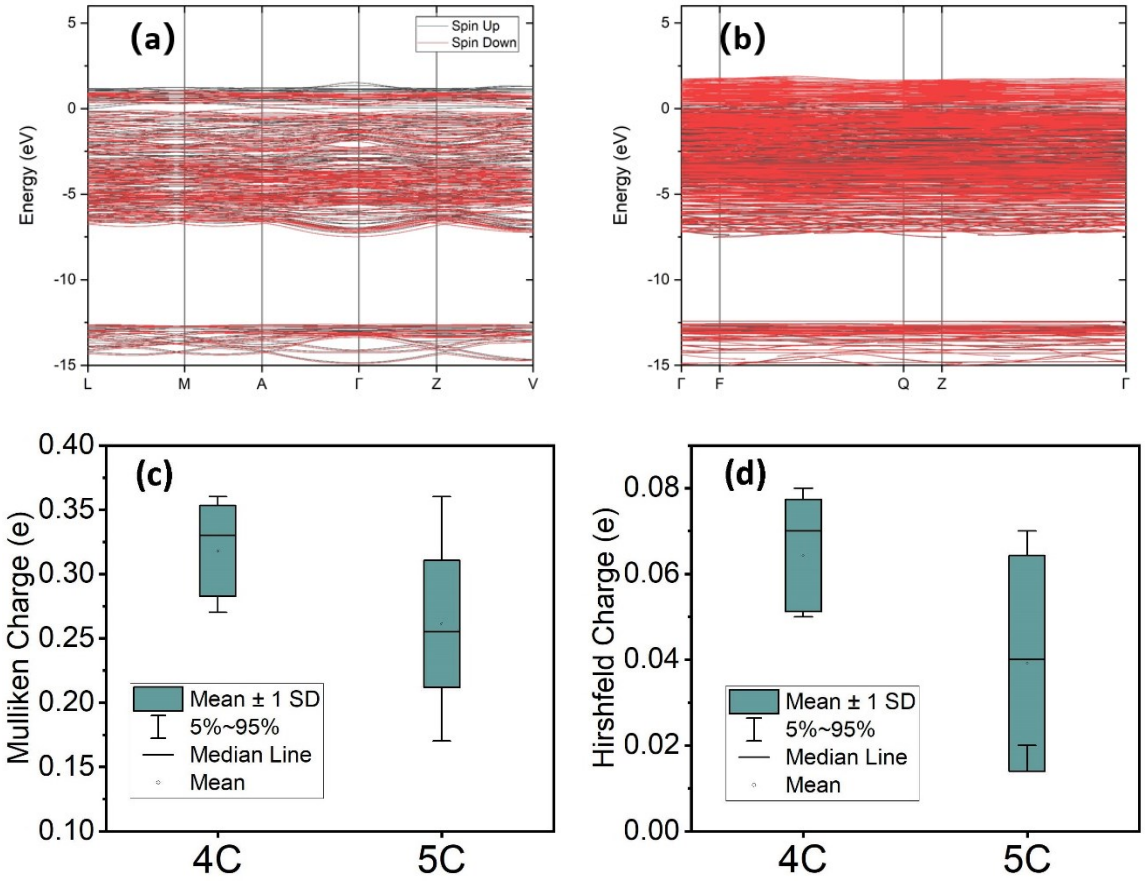

Figure A-2. Band structure of 4C-monoclinic pyrrhotite (a) and 5C-hexagonal pyrrhotite (b); Average partial charges of iron atoms in 4C-monoclinic and 5C-hexagonal pyrrhotite calculated using Mulliken (c) and Hirshfeld (d) population analyses (Error bars represent the standard deviation).[12]

[12] This simulation work was carried out by Mohammad Khalkhali.

A.1.3. Band Center

The occupied bulk S *3p* band center and bulk Fe *3d* band center (Figure 4-4c) were calculated with the formula (A-1) [109]:

$$\text{band center} = \frac{\int E \cdot f(E) dE}{\int f(E) dE} \quad \text{(A-1)}$$

Here, E refers to the electron energy, and $f(E)$ refers to their PDOS value.

A.1.4. Bond Strength

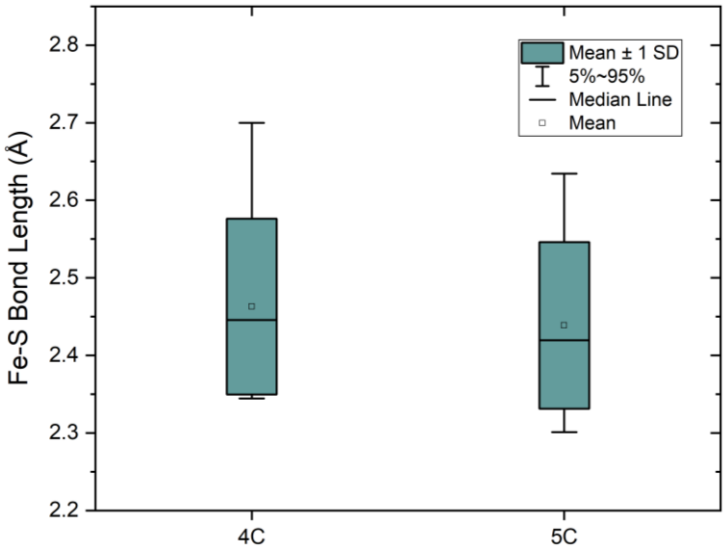

Figure A-3. Average Fe-S bond length in optimized unit cells of 4C-monoclinic and 5C-hexagonal pyrrhotite (Error bars represent the standard deviation).[13]

The average Fe-S bond length in two pyrrhotite structures was calculated and shown in Figure A-3. Figure A-3 shows that the average Fe-S bond length is slightly smaller in 5C-hexagonal pyrrhotite. Although this difference is not considerable, it confirms the Fe-S bonding is stronger in 5C-hexagonal pyrrhotite than that in 4C-monoclinic pyrrhotite,

[13] This simulation work was carried out by Mohammad Khalkhali.

consistent with the slightly higher Fe_2S^-/FeS^- intensity in hexagonal pyrrhotite deep layers (layers deeper than the III layer) than that in monoclinic pyrrhotite (see inset, Figure 4-3d).

A.2. XPS Analysis Details

The S $2p_{3/2}$ and S $2p_{1/2}$ peaks are assigned to have the same full width at half maximum (FWHM) with an intensity ratio around 1.96:1 for the $2p_{3/2}$:$2p_{1/2}$ peaks [135]. The spin-orbit-split doublet S $2p_{3/2}$ and S $2p_{1/2}$ peak energies are split by 1.19 eV [188]. Note that only binding energies of the S $2p_{3/2}$ are listed in Table 4-1.

Table A-2. Binding energies, FWHM and area ratio of multiplets for individual components of Fe(II)-S, Fe(III)-S, and Fe(III)-O used for fitting Fe $2p_{3/2}$ [174].

Species	Peak	Binding Energy (eV)	FWHM (eV)	Area
Fe(II)-S	Multi. 1	706.2	1.0	1.00
	Multi. 2	707.2	1.2	3.80
	Multi. 3	708.1	1.0	1.32
	Multi. 4	713.0	2.6	1.61
Fe(III)-S	Multi. 1	709.0	1.3	1.00
	Multi. 2	710.1	1.3	0.66
	Multi. 3	711.1	1.3	0.35
	Multi. 4	712.0	1.3	0.15
Fe(III)-O	Multi. 1	710.4	1.6	1.00
	Multi. 2	711.4	1.6	0.95
	Multi. 3	712.6	1.6	0.59
	Multi. 4	713.9	1.6	0.28

According to Legrand [131], Pratt and Nesbitt [35], iron can be affected by multiplet splitting due to unpaired electrons in the valence band, especially in intermediate and high spin states [132, 134, 136]. The parameters used for multiplet splitting for Fe $2p_{3/2}$ are listed

in Table A-2 [35, 174]. For a clear demonstration, their narrow spectra fitting peaks are shown in Figure A-4.

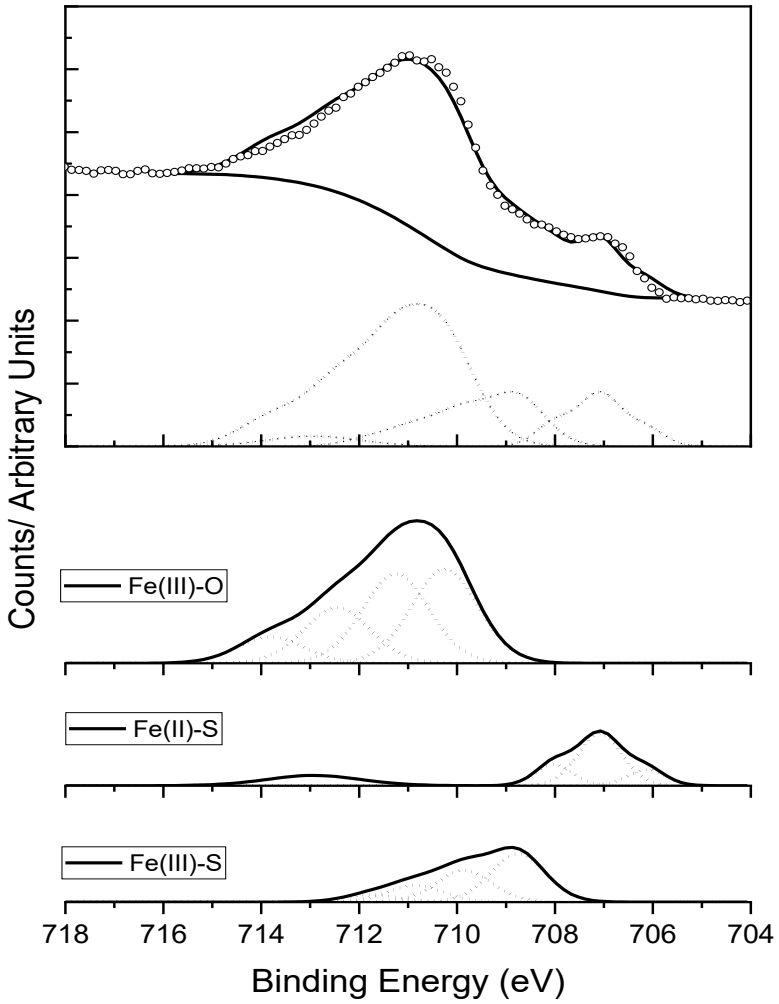

Figure A-4. XPS Fe $2p_{3/2}$ of oxidized monoclinic pyrrhotite. The top part is the fitting of the spectrum with only envelopes. The lower part is the detailed multiplet peaks for envelopes of different chemical species.

A.3. Chemical Reactions Summarized for CV studies

Chemical reactions that happened at peak A_1 (Figure 4-1) are summarized in Table A-3.

Table A-3. Summary of Electrochemical Reactions for the Anodic Peak A_1.

Chemical Reaction Equations	Potential	Reference
$Fe_{(1-x)}S+3yOH^- \rightarrow Fe_{(1-(x+y))}S+yFe(OH)_3+3ye^-$	$E_h=E_h^0-0.059*pH$	[38, 104]
$FeS+H_2O \rightarrow Fe(OH)[S]^+ +H^+ +2e^-$	$E_h=E_h^0-0.0295*pH$	[53]
$2S^{2-} \rightarrow S_2^{2-}+2e^-$	$E_h=E_h^0+0.059*lg([S_2^{2-}]/[S^{2-}]^2)$	[189]

A.4. ToF-SIMS

A.4.1. Data Interpretation

ToF-SIMS data interpretation is complicated, and the model that could be used to fully interpret their data is still not known by the authors. As an important technique to learn about the defective layer properties, particularly the bond strength, ToF-SIMS principles used in Chapter 4 are presented here via Ignatova et al.'s work [138, 139]. Ignatova et al. did semi-quantitatively reproduce the ToF-SIMS depth profile data of $ZrO_2/SiO_2/Si$ stacks with computer simulation, including the ZrO and SiO [138, 139]. For the emission of ZrO and SiO, the O atom was picked up by a more reactive atom (Zr or Si) [138, 139]. Since the O atom needed to be picked up, a high molecular binding energy between O and Zr or Si is required. The simulation model proposed by Ignatova et al. was presented as formula (A-2) [138, 139].

$$Y_i^{mol} = g_i \cdot c_o \cdot Y_i^*(U_i^{mol}) \quad \text{(A-2)}$$

Here, Y_i^{mol} refers to the molecular yield, c_o refers to the oxygen surface concentration, g_i indicates a probability factor, and $Y_i^*(U_i^{mol})$ means a modified sputter yield characterized by its surface binding energy U_i^{mol} [138, 139].

For our case, we take FeS^- as the reactive atom (one major species) and the emission of the Fe_2S^- therefore need a strong Fe-S bond to pick another iron out. So, the faster dropping of Fe_2S^-/FeS^- inside monoclinic pyrrhotite in layer III than that of hexagonal pyrrhotite seems

to suggest a faster dropping Fe-S bond strength inside monoclinic pyrrhotite than that of hexagonal pyrrhotite.

A.4.2. Sputtering Rate Estimation

According to Baryshev and Thimsen [190], the relation of the ToF-SIMS sputtering rate on pyrrhotite and silicon can be described as formula (A-3).

$$\left(\frac{SR_{Po}}{SR_{Si}}\right) = \frac{U_{o,Si}}{U_{o,Po}} \frac{n_{Si}}{n_{Po}} \frac{\alpha_{Po}}{\alpha_{Si}} \frac{\gamma_{Po}}{\gamma_{Si}} \tag{A-3}$$

Here, SR is the sputtering rate; $U_{o,Si}$ and $U_{o,Po}$ means the surface binding energy of silicon and pyrrhotite; n (atoms/volume) refers to the atomic density of the material, which can be calculated based on formula (A-4) [190]; α and γ are functions of number-average atomic mass M_t (formula (A-7)) and the projectile atomic mass M_p (Cs^+ in our case), as shown in formula (A-5) and formula (A-6) [190], respectively.

$$n = \frac{\rho}{M_t} \tag{A-4}$$

$$\alpha = 0.08 + 0.164\left(\frac{M_t}{M_p}\right)^{0.4} + 0.0145\left(\frac{M_t}{M_p}\right)^{1.29} \tag{A-5}$$

$$\gamma = \frac{4M_tM_p}{\left(M_t + M_p\right)^2} \tag{A-6}$$

Here, M_t can be calculated based on formula (A-7) [190].

$$M_t = \frac{\sum v_i M_i}{\sum v_i} \tag{A-7}$$

Here, v_i refers to the number of atoms of element i in the material, M_i is the atomic mass of the element i.

The surface binding energy of silicon $U_{o,Si}$ was estimated to be 4.67 eV/atom [191]. The cohesive energy of monoclinic and hexagonal pyrrhotite is calculated with our DFT

modeling work and listed in Table A-4. With their cohesive energy, their surface binding energy could be calculated with formula (A-8) [190].

$$U_{o,Po} = \frac{E_{coh,Po}}{\sum \nu_i} \tag{A-8}$$

Parameters used in the calculation are listed Table A-4. According to formula (A-9) [190], the ratio of sputtering rate on pyrrhotite against on silicon is 1.26 for both hexagonal and monoclinic pyrrhotite. Based on the sputtering rate on silicon (1.3 Å/s), the sputtering rate on pyrrhotite is about 1.6 Å/s. Based on this, the thickness of the oxide layer, the polysulfide layer (from 65s to 200s in Figure 4-3), and the defective layer (from 200s to 1500s in Figure 4-3) are about 10, 20, and 200 nm.

$$\left(\frac{SR_{Po}}{SR_{Si}}\right) = \frac{U_{o,Si}}{U_{o,Po}} \frac{n_{Si}}{n_{Po}} \frac{\alpha_{Po}}{\alpha_{Si}} \frac{\gamma_{Po}}{\gamma_{Si}} \approx 1.26 \tag{A-9}$$

Table A-4. Summary of Parameters and Values Used for Estimating the ToF-SIMS Sputtering Rate.[14]

Parameter	Value	Units
$E_{coh,hex\text{-}Po}$	313.72	eV/unit cell
$E_{coh,mono\text{-}Po}$	123.45	eV/unit cell
ρ_{Po}	4.6[192]	g/cm^3
ρ_{Si}	2.33[193]	g/cm^3
$M_{t,hex\text{-}Po}$	43.33	a.m.u.
$M_{t,mono\text{-}Po}$	43.16	a.m.u.
$M_{t,Si}$	28.09	a.m.u.
M_p	132.91	a.m.u.
$\gamma_{(Hex\text{-}Po,\ Cs)}$	0.74	-
$\gamma_{(Mono\text{-}Po,\ Cs)}$	0.74	-
$\gamma_{(Si,\ Cs)}$	0.58	-
$\alpha_{(Hex\text{-}Po,\ Cs)}$	0.19	-
$\alpha_{(Mono\text{-}Po,\ Cs)}$	0.19	-
$\alpha_{(Si,\ Cs)}$	0.17	-
$n_{(Hex,Po)}$	6.39×10^{22}	cm^{-3}
$n_{(Mono,Po)}$	6.42×10^{22}	cm^{-3}
$n_{(Si)}$	5.00×10^{22}	cm^{-3}
$U_{o,mono\text{-}Po}$	4.12	eV $atom^{-1}$
$U_{o,hex\text{-}Po}$	4.13	eV $atom^{-1}$
$U_{o,Si}$	4.67[191]	eV $atom^{-1}$

[14] Note that the cohesive energy and the surface binding energy listed in this table are their absolute value.

Note that the unit cell of monoclinic pyrrhotite contains 14 iron atoms and 16 sulfur atoms, meanwhile the unit cell of hexagonal pyrrhotite contains 36 iron atoms and 40 sulfur atoms.

A.5. Pyrrhotite Electrode Purity

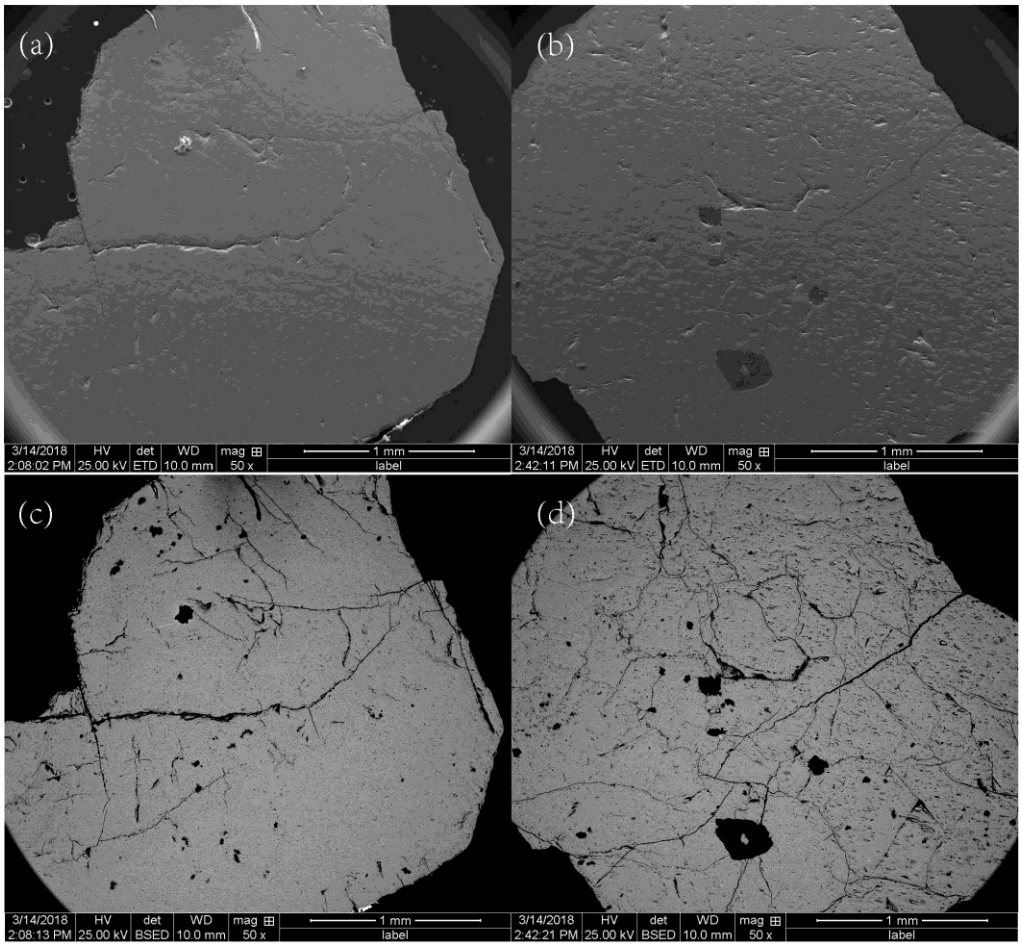

Figure A-5. SEM and BSE images of the monoclinic (a-SEM, c-BSE) and hexagonal (b-SEM, d-BSE) pyrrhotite

In the SEM-based mineral liberation analysis, different minerals can be distinguished solely based on the backscattered electron (BSE) image grey level contrast. In our experiment, both SEM images and BSE images (Figure A-5) are listed to demonstrate their purity. As shown in Figure A-5c and Figure A-5d, a slight amount of impurities do exist, but the main part of both pyrrhotites BSE images is of the same grey level, indicating that the overall purity of both pyrrhotites is good enough for our XPS and ToF-SIMS analysis. Note that most dark areas in Figure A-5c and Figure A-5d are a result of crevices. Their

main composition was analyzed with the Energy-dispersive X-ray Spectroscopy (EDX). The EDX results showed that the main part of hexagonal pyrrhotite is composed of 61.81% Fe and 38.19% S; meanwhile, the monoclinic pyrrhotite is composed of 61.34% Fe and 38.66% S.

Appendix B. Supporting Information: Unraveling H_2O_2-stimulated Surface Oxidation of Hexagonal Pyrrhotite and Pentlandite by Underlying Electronic Structures

B.1. Flotation

B.1.1. Single Mineral Preparation

The single hexagonal pyrrhotite mineral particles were prepared according to the procedure described in Chapter 6 Section 6.2.1 Materials and Chemicals. Single pentlandite mineral particles used in Chapter 5 were the nickel concentrate from Copper Cliff Mills (Vale Canada Limited, Copper Cliff, Ontario, Canada). Mineral particles of -74/+38 μm size range were obtained via sieving and slight grinding of the oversized particles. They were then washed with pH 2 sulfuric acid solution for 10 min at least twice to clean the surface, followed by exchanging the acid wash solution to Milli-Q water three times. The washed particles were then cleaned and stored following the same procedure used on the single hexagonal pyrrhotite particles.

The magnetic monoclinic pyrrhotite comes from Sudbury, Canada and Virginia, America. Single minerals of -74/+38 μm size range were purified via dry grinding, sieving, and magnetic separation. Note that for the magnetic separation, a hand-magnet is good enough for monoclinic pyrrhotite.

B.1.2. Single Mineral Characterization

Table B-1. Mineral assay (from XRF) and pyrrhotite type ratio (from Bruker D8 Advance XRD) of hexagonal pyrrhotite, monoclinic pyrrhotite and pentlandite single minerals.

Single Minerals	Mineral Assay (wt %)				Po Type Ratio	
	Cp	Pn	Po	NSG	Mag Po	Non-Mag Po
Pn	1.5	87.5	8.3	2.7	-	-
Hexagonal Po	2.1	0	96.3	1.6	0	100
Monoclinic Po	1.0	3.6	94.8	0.6	100	0

*Cp– chalcopyrite, Pn– pentlandite, Po- pyrrhotite, and NSG– non-sulfide gangue.

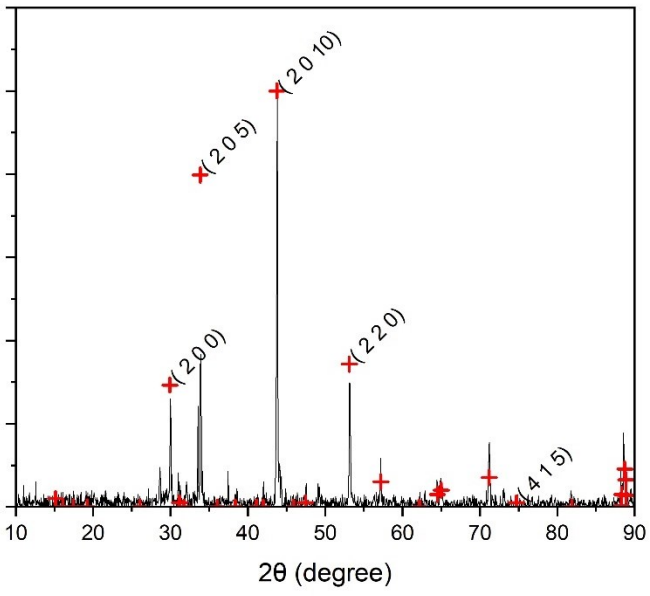

Figure B-1. The powder X-ray diffraction (XRD) results of the ground hexagonal pyrrhotite using CuKα radiation and the reference from the JCPDS database (PDF-29-0724).

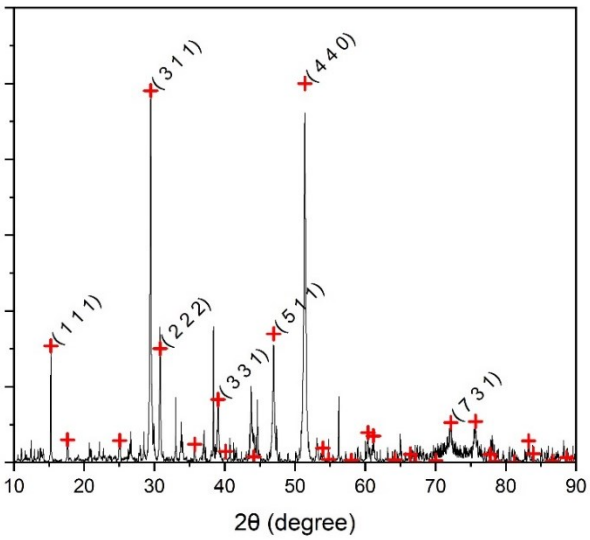

Figure B-2. The powder X-ray diffraction (XRD) results of the ground pentlandite using CuKα radiation and the reference from the JCPDS database (PDF-86-2279).

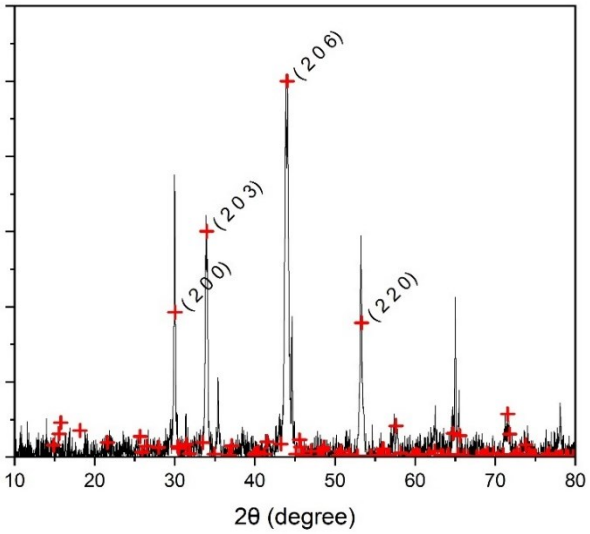

Figure B-3. The powder X-ray diffraction (XRD) results of the ground pentlandite using CuKα radiation and the reference from the JCPDS database (PDF-71-0647).

The elemental compositions of the single minerals were determined by an Orbis PC Micro-DEXRF Elemental Analyzer and their crystal structure further confirmed by X-ray Powder Diffraction (XRD, Rigaku Ultima IV) as shown in Figure B-1, Figure B-2, and Figure B-3. The proportion of monoclinic pyrrhotite and hexagonal pyrrhotite in the single minerals

was tested and analyzed by Expert Process Solutions via a D8 Advance XRD (Bruker, Massachusetts, USA). According to the peak-ratio method proposed by Graham [147] and refined by Multani and Waters [181], if the ratio of peak intensity at 51.40 degree over the peak intensity at 51.75 degree in the XRD tests using CoKα radiation ($I_{51.40}/I_{51.75}$) is over 9, the proportion of the hexagonal pyrrhotite in the pyrrhotite sample could be considered as 100%; while if $I_{51.40}/I_{51.75}$ is smaller than 0.6, the proportion of the monoclinic pyrrhotite in the pyrrhotite sample could be considered as 100%. Therefore, the hexagonal pyrrhotite could be considered that contains no monoclinic pyrrhotite since its $I_{51.40}/I_{51.75}$ is larger than 9. In contrast, the monoclinic pyrrhotite contains no hexagonal pyrrhotite since its $I_{51.40}/I_{51.75}$ is lower than 0.6. The analysis results are presented in Table B-1.

B.1.3. Micro-flotation Procedures

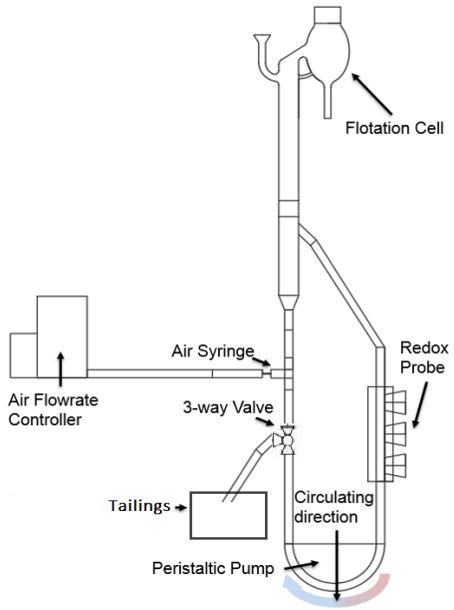

Figure B-4. The schematic diagram for the modified micro-flotation tube.

Micro-flotation tests were conducted with a home-designed micro-flotation tube (Figure B-4). Before the flotation, 2.1 g of mineral particles were agitated in 500 ml Milli-Q water

in the ultrasonic cleaning bath for 10 min, and the mineral particles were then transferred to N_2-purged (at least 30 min) buffer solutions (0.05 M $Na_2B_4O_7$). H_2O_2 was then added into the solution to the desired concentration. After 1 h of conditioning by H_2O_2, PIBX was added to 10.6 μM to condition particles for another 2 min. Flotation concentrates were collected at (1, 2, 5, 7, and 10) min for single mineral flotation tests and at (1, 2, 5, and 10) min for paired mineral flotation tests. The electrochemical potential was recorded during the whole experiment using a standard 3-electrode cell with the platinum working electrode, the platinum counter electrode, and a saturated calomel reference electrode.

The tube is composed of two major parts: the lower circulation loop and the upper Hallimond tube [194]. The pulp was circulated via a peristaltic pump in the lower circulation loop to reach a flow rate of 1.8 l/min. N_2 was injected via a combination of a syringe and a digital flowmeter, at a rate of 6 ml/min.

B.1.4. Flotation Results

Mineral flotation recoveries (Figure B-5a, Figure B-5c, Figure B-5e) of pentlandite and hexagonal pyrrhotite indicate that H_2O_2 can selectively depress hexagonal pyrrhotite. For single mineral flotation, when the H_2O_2 concentration increased from 0 mM to 5.29 mM, the recovery of hexagonal pyrrhotite at 10 min dropped from 85% to around 10%, while the recovery of pentlandite was about 85% under all these tested concentrations. For mixed mineral flotation, when the concentration of H_2O_2 increased from 0 mM to 5.29 mM, the recovery of hexagonal pyrrhotite at 10 min dropped from about 90% to about 40%, and that of pentlandite remained around 85% (Figure B-5e). It is suggested that a one-hour low-concentration H_2O_2 conditioning can selectively depress hexagonal pyrrhotite without affecting the flotation of pentlandite.

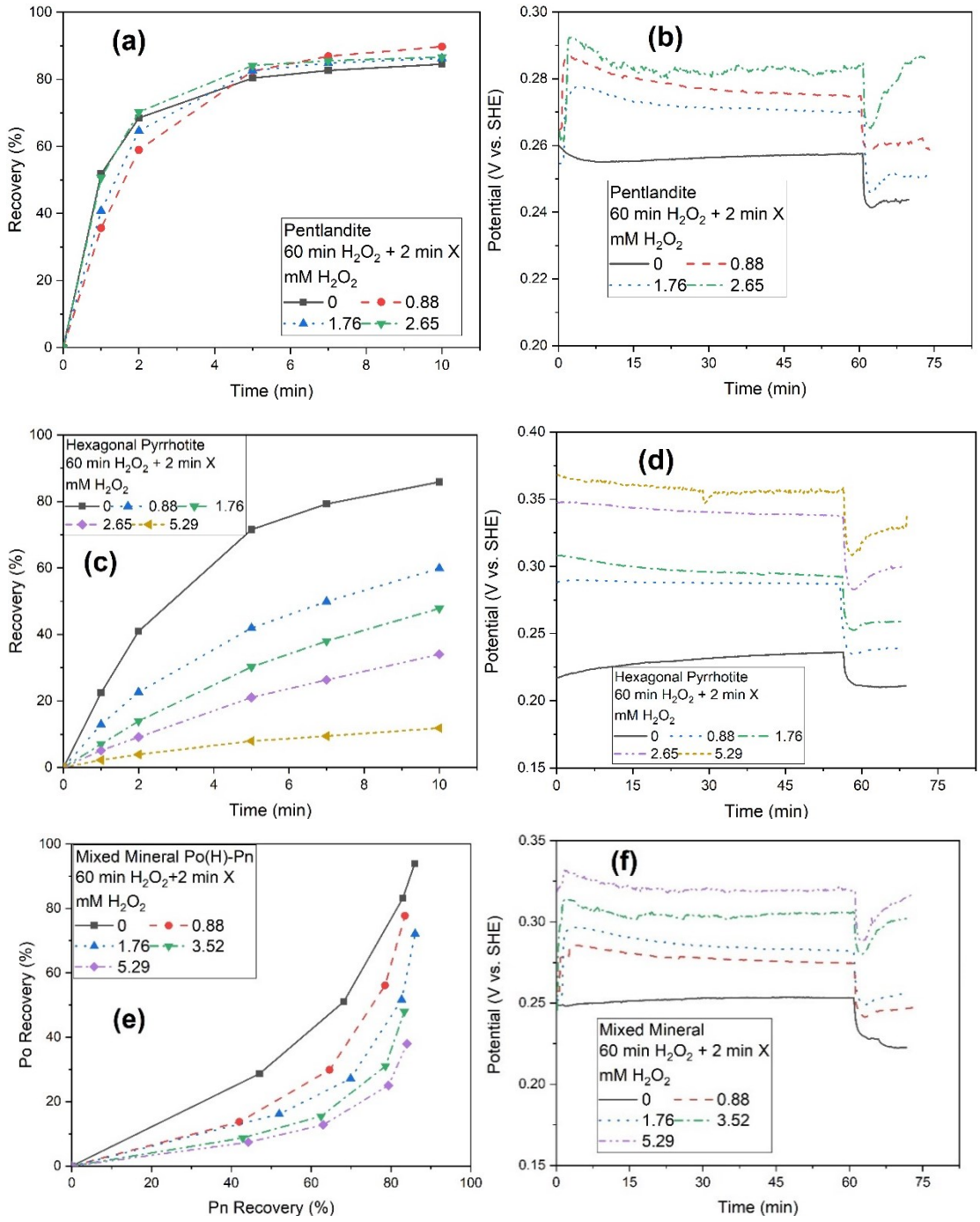

Figure B-5. Single mineral flotation recovery and potential variation, respectively, of pentlandite (a, b) and hexagonal pyrrhotite (c, d); flotation recovery (e) and potential variation (f) of mixed pentlandite and hexagonal pyrrhotite (1:1 mass ratio). Mineral particles were conditioned in different concentrations of H_2O_2 for 1 h and 10.6 μM PIBX for 2 min before starting flotation.

B.2. Dissolved Oxygen Tests Setup

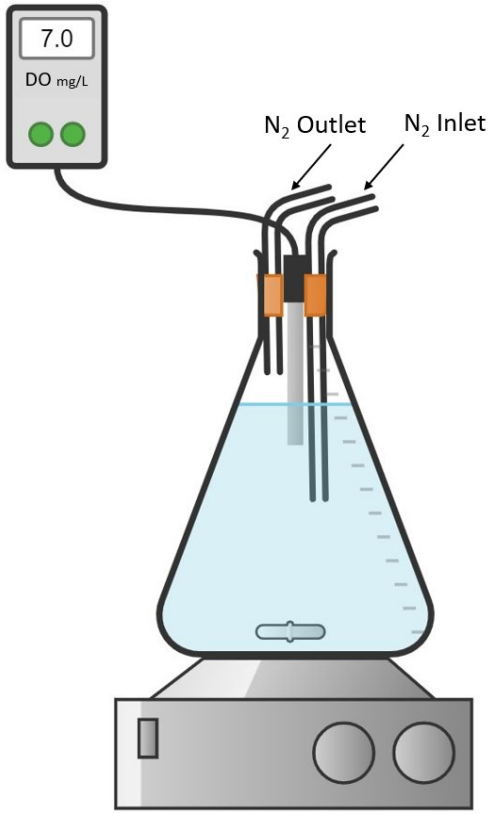

Figure B-6**.** The schematic diagram for the dissolved oxygen test setup.[15]

B.3. Electrochemical Tests

As shown in Figure B-7, the exchange current density (j_{ex}) of the pentlandite is several times higher than the j_{ex} of the hexagonal pyrrhotite. Meanwhile, the j_{ex} of pentlandite decreased much more sharply than that of the hexagonal pyrrhotite. For a detailed discussion, please refer to Section 5.3.7 Discussion.

[15] Note that the N_2 inlet is maintained under the solution surface when purging the solution and remained over the solution surface during the H_2O_2 conditioning.

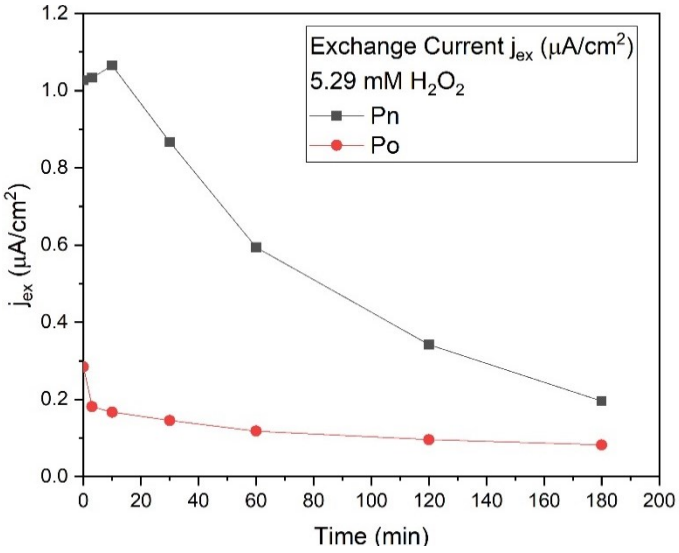

Figure B-7. Variation of the exchange current density j_{ex} of the hexagonal pyrrhotite and the pentlandite in the open circuit chronopotentiometry (CP) test intervened with the linear sweep voltammetry (LSV) as determined by Tafel plot analysis.

Table B-2. Tafel analysis results of the LSV tests in open-circuit chronopotentiometry (CP) intervened with the LPR.

Electrode	$[H_2O_2]$ (mM)	E_{oc} (V)	E_{corr} (V)	i_{corr} (μA/cm^2)	β_a (V/dec)	β_c (V/dec)	R_p (kΩ/cm^2)
Po(H)	0	0.148	0.096	1.458	0.324	0.159	2264.175
	1.76	0.249	0.216	1.712	0.160	0.173	1500.422
	5.29	0.275	0.257	2.211	0.131	0.191	1087.665
Pn	0	0.194	0.173	2.208	0.201	0.264	1783.631
	1.76	0.251	0.229	5.556	0.147	0.187	655.041
	5.29	0.261	0.248	12.613	0.183	0.212	567.827

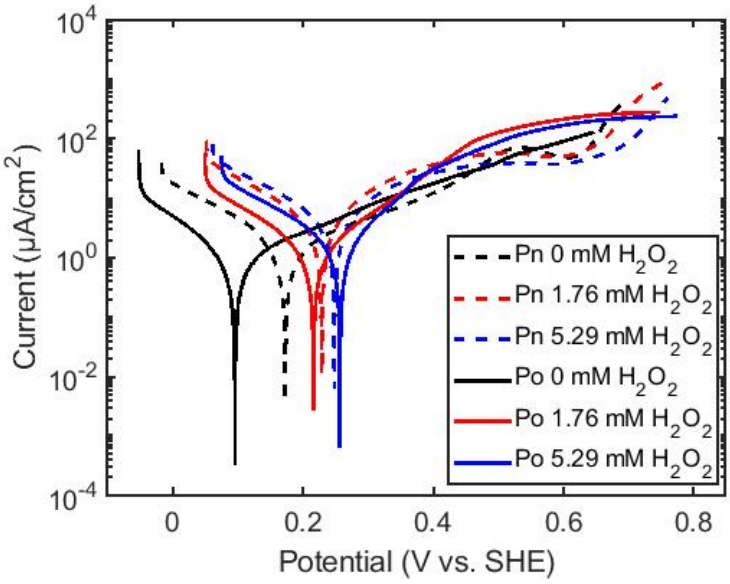

Figure B-8. Linear sweep voltammograms (LSVs) for the stationary pentlandite (dashed lines) and hexagonal pyrrhotite (solid lines) electrodes. LSVs listed were obtained immediately after the sixth linear polarization resistance (LPR) in the open circuit chronopotentiometry (CP) intervened with the LPR.

B.4. Sputtering Rates of ToF-SIMS and XPS

According to Baryshev and Thimsen [190], the following formula (B-1) can describe the relationship between the sputtering rate on sulfide minerals and that on silicon:

$$\left(\frac{SR_{Po}}{SR_{Si}}\right) = \frac{U_{o,Si}}{U_{o,Po}} \frac{n_{Si}}{n_{Po}} \frac{\alpha_{Po}}{\alpha_{Si}} \frac{\gamma_{Po}}{\gamma_{Si}} \quad \text{(B-1)}$$

Here, SR refers to the sputtering rate; U_o is the surface binding energy of the mineral of interest; n (atoms/volume) refers to the minerals' atomic density, calculated according to formula (B-2) [190]; α (formula (B-3)) and γ (formula (B-4)) are functions of M_t (number-average atomic mass, formula (B-5)) and M_p (the projectile atomic mass, Cs^+ for ToF-SIMS and Ar^+ for XPS) [190].

$$n = \frac{\rho}{M_t} \quad \text{(B-2)}$$

$$\alpha = 0.08 + 0.164\left(\frac{M_t}{M_p}\right)^{0.4} + 0.0145\left(\frac{M_t}{M_p}\right)^{1.29} \quad \text{(B-3)}$$

$$\gamma = \frac{4M_tM_p}{\left(M_t + M_p\right)^2} \quad \text{(B-4)}$$

$$M_t = \frac{\sum v_i M_i}{\sum v_i} \quad \text{(B-5)}$$

In formula (B-5), M_i refers to the element i's atomic mass, and v_i is the element i's atom number in the material. Based on formula (B-2) to formula (B-5), all parameters needed are calculated and listed in Table B-3.

For the ToF-SIMS depth profile, the Cs^+ was used as the sputtering source:

$$\left(\frac{SR_{Hex-Po,Cs}}{SR_{Si,Cs}}\right) = \frac{U_{o,Si}}{U_{o,Po}}\frac{n_{Si}}{n_{Po}}\frac{\alpha_{Po,Cs}}{\alpha_{Si,Cs}}\frac{\gamma_{Po,Cs}}{\gamma_{Si,Cs}} \approx 1.26 \quad \text{(B-6)}$$

$$\left(\frac{SR_{Pn,Cs}}{SR_{Si,Cs}}\right) = \frac{U_{o,Si}}{U_{o,Pn}}\frac{n_{Si}}{n_{Pn}}\frac{\alpha_{Pn,Cs}}{\alpha_{Si,Cs}}\frac{\gamma_{Pn,Cs}}{\gamma_{Si,Cs}} \approx 1.02 \quad \text{(B-7)}$$

For the XPS depth profile, the Ar^+ was used as the sputtering source:

$$\left(\frac{SR_{Hex-Po,Ar}}{SR_{SiO_2,Ar}}\right) = \frac{U_{o,SiO_2}}{U_{o,Po}}\frac{n_{SiO_2}}{n_{Po}}\frac{\alpha_{Po,Ar}}{\alpha_{SiO_2,Ar}}\frac{\gamma_{Po,Ar}}{\gamma_{SiO_2,Ar}} \approx 5.53 \quad \text{(B-8)}$$

$$\left(\frac{SR_{Pn,Ar}}{SR_{SiO_2,Ar}}\right) = \frac{U_{o,SiO_2}}{U_{o,Po}}\frac{n_{SiO_2}}{n_{Po}}\frac{\alpha_{Po,Ar}}{\alpha_{SiO_2,Ar}}\frac{\gamma_{Po,Ar}}{\gamma_{SiO_2,Ar}} \approx 4.37 \quad \text{(B-9)}$$

The ToF-SIMS sputtering rate on the hexagonal pyrrhotite and the pentlandite are 1.6 Å/s and 1.3 Å/s, respectively; the XPS sputtering rate on the hexagonal pyrrhotite and the pentlandite are 17.7 nm/min and 14.0 nm/min, respectively.

Table B-3. Summary of parameters and values used for estimating the sputtering rate of ToF-SIMS and XPS when applied on the hexagonal pyrrhotite and the pentlandite.[16]

Parameter	Value	Units
ρ_{Po}	4.6[192]	g/cm^3
ρ_{Pn}	4.8[195]	g/cm^3
ρ_{Si}	2.33[193]	g/cm^3
ρ_{SiO2}	2.65[195]	g/cm^3
$M_{t,hex\text{-}Po}$	43.33	a.m.u.
$M_{t,Pn}$	45.49	a.m.u.
$M_{t,Si}$	28.09	a.m.u.
$M_{t,SiO2}$	20.03	a.m.u.
$M_p(Ar)$	39.95	a.m.u.
$M_p(Cs)$	132.91	a.m.u.
$\gamma_{(Hex\text{-}Po,\ Cs)}$	0.74	-
$\gamma_{(Pn,\ Cs)}$	0.76	-
$\gamma_{(Si,\ Cs)}$	0.58	-
$\gamma_{(Hex\text{-}Po,\ Ar)}$	1.00	-
$\gamma_{(Pn,\ Ar)}$	1.00	-
$\gamma_{(SiO2,\ Ar)}$	0.89	-
$\alpha_{(Hex\text{-}Po,\ Cs)}$	0.19	-
$\alpha_{(Pn,\ Cs)}$	0.19	-
$\alpha_{(Si,\ Cs)}$	0.17	-
$\alpha_{(Hex\text{-}Po,\ Ar)}$	0.27	-
$\alpha_{(Pn,\ Ar)}$	0.27	-
$\alpha_{(SiO2,\ Ar)}$	0.21	-
$n_{(Hex,Po)}$	6.39×10^{22}	cm^{-3}
$n_{(Pn)}$	6.35×10^{22}	cm^{-3}
$n_{(Si)}$	5.00×10^{22}	cm^{-3}
$n_{(SiO2)}$	7.97×10^{22}	cm^{-3}
$U_{o,hex\text{-}Po}$	4.12[8]	eV atom^{-1}
$U_{o,Pn}$	5.33[196]	eV atom^{-1}
$U_{o,Si}$	4.67[197]	eV atom^{-1}
$U_{o,SiO2}$	12.94[198, 199]	eV atom^{-1}

[16] Note that surface binding energies listed in this table are absolute values.

B.5. Fenton Reactions of H_2O_2 [200, 201]

$$Fe^{3+} + H_2O_2 \rightarrow Fe^{2+} + H^+ + OOH^* \quad \text{(B-10)}$$

$$Fe^{3+} + OOH^* \rightarrow Fe^{2+} + H^+ + O_2 \quad \text{(B-11)}$$

$$OOH^* + H_2O_2 \xrightarrow{Fe^{2+}/Fe^{3+}} H_2O + OH^* + O_2 \quad \text{(B-12)}$$

$$Fe^{2+} + OOH^* \rightarrow Fe^{3+} + OH^* + OH^- \quad \text{(B-13)}$$

B.6. DFT Simulation Results

Table B-4. The optimized crystal structures of the pentlandite and the pyrrhotite from DFT+U calculation.[17]

		a (Å)	b (Å)	c (Å)	α (°)	β (°)	γ (°)	V (Å3)
Pentlandite	Calc.	10.11	10.11	10.11	90	90	90	0
	Exp.[158]	10.03	10.03	10.03	90	90	90	0
Pyrrhotite	Calc.*	6.85	6.85	12.90	114.06	114.06	59.98	3.16
	Exp.[156]	7.1	7.1	13.38	113.65	113.65	62.57	3.77

To further analyze the difference between the electronic structures of the pyrrhotite, and the pentlandite, we performed population analysis to calculate their partial atomic charges. Although the absolute magnitude of the atomic charges calculated through population analysis has little physical meaning, their relative values, when consistent computational parameters were used, can reveal useful information. DFT calculations performed in this study met this condition as we used the same computational parameters.

[17] This simulation work was carried out by Mohammad Khalkhali.

Table B-5. The calculated U values for the metal atoms in the pentlandite and the pyrrhotite.[18]

Mineral	Metal Species	a (Å)
Pentlandite	Octa. Fe	5.45
	Tetra. Fe	5.39
	Octa. Ni	6.60
	Tetra. Ni	5.95
Pyrrhotite	Fe1(F)	4.61
	Fe2(F)	5.10
	Fe3(V)	4.83
	Fe4(V)	4.53

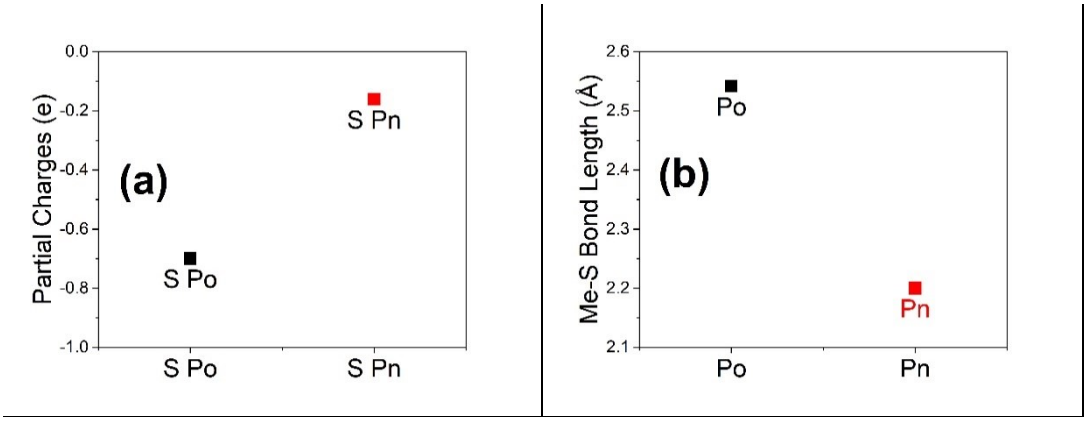

Figure B-9**.** Average partial charges (a) of sulfur atoms and average metal-sulfur bond length (b) in the pyrrhotite and the pentlandite.[19]

[18]Octa. Me – octahedrally coordinated metal atoms; Tetra. Me – tetrahedrally coordinated metal atoms; F – the layer without iron vacancy; V – the layer with iron vacancies. This simulation work was carried out by Mohammad Khalkhali.

[19] This simulation work was carried out by Mohammad Khalkhali.

As shown in Figure B-9a, the population analyses confirmed that sulfur atoms are more negatively charged in the pyrrhotite than those in the pentlandite. This means sulfur atoms in pyrrhotite have a more nucleophilic nature and, therefore, they are more prone to oxidation inherently. It is important to note that the conclusion is made based on the electronic properties of the bulk structures, and explicit simulation of the oxidation process on the surface is needed to drive more accurate conclusions. However, it is interesting that our simulation results confirm our experimental observation.